Microcircuitry in the Entorhinal Cortex

DISSERTATION

To obtain the academic degree
Doctor rerum naturalium (Dr. rer. nat.)

submitted to the
Department of Biology, Chemistry and Pharmacy
of Free University, Berlin

by
Prateep Sanker Beed
from Calcutta, India

January, 2010

This experimental work of this thesis was completed under the supervision of Prof. Dr. Dietmar Schmitz in the time period October 2006 – September 2009 at the Neuroscience Research Centre, Charité, Berlin, Germany.

1st Reviewer : Prof. Dr. Dietmar Schmitz

2nd Reviewer : Prof. Dr. Stephan Sigrist

Date of Defence : 28th April, 2010

CONTENTS

ABBREVIATIONS

ACSF	-	Artifical Cerebro-Spinal Fluid
AP	-	Action Potential
CA1-3	-	Cornu ammonis Area 1-3
DG	-	Dentate Gyrus
EC	-	Entorhinal Cortex
EEG	-	Electroencephalogram / graphy
EPSC	-	Excitatory Postsynaptic Current
mEC	-	Medial Entorhinal Cortex
P	-	Postnatal days
pA	-	picoAmpere
IUE	-	*in utero* Electroporation
KO	-	Knockout
L1 – 6	-	Layers I, II, III, IV, V and VI
L2S	-	Layer II Stellate cell
L2P	-	Layer II Pyramidal cell
L3P	-	Layer III Pyramidal cell
LPA	-	Lysophosphatidic Acid
LPP	-	Lipid phosphate phosphatase
PRG	-	Plasticity Related Gene
TLE	-	Temporal Lobe Epilepsy
UV	-	Ultraviolet
WT	-	Wildtype

ABSTRACT

Computation of neuronal information in local microcircuits underlies critical brain functions. Such microcircuits connect excitatory and inhibitory neurons to functional neuronal networks. By studying normal or misconnected neuronal microcircuits one can better understand the underlying functions in physiological or pathological conditions.

The microcircuitry of the entorhinal cortex has thus far always been investigated in relation to its role as an information hub between the cortex and the hippocampus. However, recent *in vivo* work has revealed the functional relevance of the entorhinal cortex as an independent computational unit serving a pivotal role in spatial navigation. In addition, disruption of the basal neuronal synchrony and excitability in the entorhinal cortex has been implicated in Alzheimer's disease, temporal lobe epilepsy (TLE), schizophrenia and many other neuropsychiatric disorders. To date, the functional microcircuitry of the entorhinal cortex, in particular the medial entorhinal cortex (mEC) that might underlie its independent role in physiology and involvement in pathophysiology has not been specifically addressed.

During my doctoral thesis, I aimed to systematically study the neuronal microcircuitry in the mEC underlying its role in spatial navigation and neuronal synchrony. Using a combination of electrophysiological and optical techniques, I looked at the microcircuitry of the two projection neurons in the L2 mEC – the Layer 2 stellate cell (L2S) and the Layer 2 pyramidal cell (L2P) and also the role of the Layer 3 pyramidal cell (L3P) in neuronal synchrony and excitability.

Taken together, the first direct functional evidence for a cell-type specific and modular organization of inputs upon the L2S and L2P is provided in this thesis, thereby furthering the

knowledge as to how information is transferred within the local microcircuitry of the mEC. Further, the characterization of the kainate receptors (KARs) on L3Ps is a step forward in our understanding of the KAR-mediated synaptic transmission and its contribution towards neuronal synchrony and network excitability in the mEC. As an outlook, the studies on a novel modulator of synaptic strength, PRG-1, exhibit a critical way in which neuronal networks are finely tuned. The balance between excitation and inhibition is needed to maintain the integrity of neuronal microcircuits.

In conclusion, these are the first steps towards understanding the functional microcircuitry of the mEC that might explain its emerging independent role in neuronal information processing, both under physiological and pathological conditions.

CHAPTER 1:

NEURONAL MICROCIRCUITS

The clustering of several neurons into functional modules in the brain has been reported since the earliest days independent of species, age, and cortical area (Cajal, 1911; Steriade, 2001). There exists a striking similarity in the organization of such functional modules, 'microcircuits', across species. This robustness of neuronal organization implies the importance of microcircuits in carrying out the principal functions of the brain. These include fundamental functions - spatial navigation, locomotion, memory, vision, olfaction, etc. - and higher order cognitive functions - decision making, evaluating reward and punishment, processing emotions and facial expressions, etc. (Grillner et al., 2005; Schubert et al., 2007; Silberberg et al., 2005; Thomson and Lamy, 2007).

1.1 Hierarchical organization

The brain is organized in a strict hierarchy. The different brain areas (Brodman's areas or the different lobes) are made up of networks containing functional microcircuits which in turn are composed of neurons that possess a branched architecture of dendrites bearing the simplest computational unit – the spine (Toledo-Rodriguez et al., 2005). This hierarchy provides the opportunity to study the neuronal organization of the brain at many levels; however, this itself is a challenge, as one finally needs to integrate the information from all disciplines of

neuroscience to have a holistic understanding of brain functions. Thus for any systematic study of brain functions, a specific question is needed, and more importantly, there is a need to investigate at the right level of organization. With the advent, implementation and combination of new techniques with improved temporal and spatial resolution it is now possible to simultaneously address questions at more than one level of neuronal organization (Arenkiel and Ehlers, 2009; Scanziani and Häusser, 2009).

1.2 Establishment of microcircuits over development

The development of the brain's circuitry requires the coordination of an extraordinarily complex set of neurodevelopmental events. The structure and function of neuronal microcircuits perpetually matures from the time of first contact between nerve cells. The interplay of inherent genetic programs with a wide range of environmental exposures and experiences determines the birth, death, and cellular characteristics of neurons, as well as the formation and reformation of their axons, dendrites, and synapses. Neuronal microcircuits consequently have diverse functional attributes within a finite set of genetically and environmentally constrained designs and functions.

In humans, the early postnatal period represents a time of dramatic change in brain structure and function. The brain grows to about 70% of its adult size by 1 year of age and to about 80% of adult size by age 2 years (Dekaban, 1978; Knickmeyer et al., 2008). Development of gray and white matter, myelination, synaptogenesis, pruning, and synaptic modification establish the fundamental anatomical organization for the initial functioning of neural circuits *in utero*. These progressive and regressive developmental processes continue in early postnatal life. Subsequently, local connections within cortical circuits are fine-tuned, and complex longer-range connections among circuits form an increasingly unified and functionally organized neuronal network. During early postnatal life, the newborn does not simply experience novel stimuli passively; the infant also elaborates behaviors that powerfully influence its environment (Kandel et al., 2000). Together with inborn genetic factors, novel experiences and behavioral responses act on a still immature brain to stimulate the further development of neuronal circuits. With time, experience has an increasingly prominent function in the shaping of neuronal circuitry.

In rodents, it has been observed that developing neuronal microcircuits are highly excitable and have an intrinsic tendency to oscillate (Ben-Ari, 2008). *In utero* they generate intrinsic voltage-dependent calcium currents that do not propagate, and then they form small cell

assemblies interconnected by gap junctions that generate non-synaptic calcium plateaus around delivery time. The first synapse-driven coherent patterns appear soon after (the so-called giant depolarizing potentials or GDPs) and connect large neuronal populations (Crepel et al., 2007). Similar coherent patterns are present in macaque neurons *in utero* and in premature infants. Neuronal properties are also rapidly modified enabling the sequential development of important functions. In summary, neurons have a developmental-stage-dependent expression of electrical signals that provides a read-out of their state and modulates the subsequent operation of the system (Ben-Ari, 2008). In adult rats and mice, neuronal microcircuits in the brainstem, hippocampus and neocortex give rise to cortical rhythms (central pattern generator, gamma and theta oscillations) and provide evidence for a coherent functioning of neuronal assemblies / microcircuits (Grillner et al., 2005; LeBeau et al., 2005; Thomson and Lamy, 2007).

The flexibility and diversity of developmental outcomes create a fine balance between adaptation and vulnerability during development from the level of individual circuits to the level of the maturing individual. The opportunities for adaptive change and the periods of critical vulnerability during the development of neuronal circuits are themselves dynamic, temporally specific, and sensitive to experience and environmental exposures (Ben-Ari, 2008). As cognition, emotions, and behaviors in health and illness are increasingly viewed in terms of the functioning of neuronal circuits, defining typical trajectories for the maturation of those circuits provides a crucial background against which genetic alterations and the effects of adverse experience on brain maturation can be compared and contrasted to identify the developmental origins of neuropsychiatric diseases (Ben-Ari, 2008).

1.3 Features of a microcircuit

1.3a Defining a microcircuit

The brain is modular in its architecture and it consists of various networks that serve different functions in different brain regions. Underlying these networks are functional modules known as microcircuits. ‘Microcircuit’ is used to denote a minimal number of neurons that can collectively produce a functional output (Grillner et al., 2005). From a networks perspective, neuronal microcircuits are the fundamental structural and functional units in the brain.

Microcircuits have a well-defined structure (intrinsic and extrinsic connectivity patterns consisting of excitatory and inhibitory neurons that are interconnected with dynamic synapses as elementary building blocks) (Grillner et al., 2005). Though there is a structural

homogeneity, microcircuits are organized to serve unique functions – they can be constructed to produce autonomous rhythmic behaviour (in the spinal cord), to relay and transform information to build maps of associations between parameters of the world (in the hippocampus), to predict events and deal with real-time updates (in the neocortex), or to compute error functions of the mismatch between the predicted and actual world (cerebellum) (Grillner et al., 2005; LeBeau et al., 2005; Silberberg et al., 2005; Thomson and Lamy, 2007). Thus even though there exists a canonical structure ('structural stereotypy'; Silberberg et al., 2002), microcircuits perform different functional roles ('functional heterogeneity'). These ideas are discussed in the following subsections.

1.3b Structural stereotypy

Stereotypy refers to a repeating pattern of structural and/or functional features. An important example is that of the neocortical microcircuitry. Stereotypical morphology, electrophysiology and molecular profiles have enabled characterization of many different types of neocortical neurons (DeFelipe 1993; Fairen et al., 1984; Kawaguchi et al., 1997; Toledo-Rodriguez et al., 2002; White, 1989). Distinct spatial arrangements and precise connectivity patterns between these neurons give rise to stereotypical microcircuits. Striking examples of spatial stereotypy are the layering of neurons in the neocortex and the specific distributions of different cell types across neocortical layers and areas (White, 1989).

Cortical cells are also organized vertically: such arrangements are especially apparent in primates, where groups of ~100–200 neurons are arranged around tight bundles of the apical dendrites of pyramidal cells. The dimensions of these 'minicolumns' (~30 μm in diameter) are surprisingly stereotypical across most cortical areas and regions, and even across many species (Mountcastle, 1998; Peters et al., 1993; Schmolke et al., 1997).

1.3c Functional heterogeneity

Even though a structural stereotypy is observed in cortical microcircuits, each is specialized to perform a different function. The functional heterogeneity mostly arises from the intrinsic properties of the neurons and the dynamic synapses that connect one neuron to the other (Silberberg et al., 2005). Each synapse has its characteristic release properties (number of active zones, release probability) and plasticity mechanisms. Depending on the synaptic input a single neuron receives in the microcircuit, it responds by firing action potentials. Thus in a functional microcircuit it is necessary to understand the dynamics of synaptic transmission in addition to its structural organization.

Of particular interest in my PhD work is the microcircuitry of the entorhinal cortex. This cortical region has been long considered as the input-output hub of information flow between the neocortex and the hippocampus (Amaral and Witter, 1989; Fernandez et al., 1999; Fell et al., 2001; Van Hoesen, 1982; Witter et al., 1989). Recent advances however, point to a more independent role of the entorhinal cortex as an integral computational unit for spatial navigation (Hafting et al., 2005). Even though many anatomical studies have shed light on the structural organization of the microcircuitry in the entorhinal cortex, to date little has been done to integrate such knowledge with functional roles due to a wide chronological gap in the structural and functional studies.

In the following section, I briefly introduce the entorhinal cortex and in the next chapter I will discuss the prevailing and emerging functional roles of the entorhinal cortex. Thereby I will emphasize the need to understand the microcircuitry of the entorhinal cortex and how it might shed light on the functions it performs.

1.4 The Entorhinal Cortex

The entorhinal cortex (Brodman area 28) is located in the temporal lobe and derives its name from the fact that it is partially enclosed by the rhinal (olfactory) sulcus (figure 1-01). Interest in the entorhinal cortex arose around the turn of the 20th century when Cajal, in his seminal studies on the anatomy of the nervous system, described a peculiar part of the posterior temporal cortex which is strongly connected to the hippocampus with fibers that merge in the angular bundle and perforate the subiculum (Canto et al., 2008). Cajal was so struck by this massive connection that he suggested that the physiological significance of the hippocampus had to be related to that of the entorhinal cortex.

The entorhinal cortex is surrounded by a number of cortical areas. Anterio-laterally, it meets with the piriform (olfactory) cortex, and anterior-medially it is surrounded by the periamygdaloid cortex and the posterior cortical nucleus of the amygdala. On its medial side, the entorhinal cortex merges with structures that belong either to the hippocampal formation or the parahippocampal region, such as the amygdalo-hippocampal transition, and the parasubiculum. The lateral and posterior borders are with the other two major constituents of the parahippocampal region, the perirhinal cortex laterally and the parahippocampal cortex (in non-primate species generally referred to as postrhinal cortex) posteriorly (figure 1-01; Amaral and Witter, 1989; Canto et al., 2008; Witter et al., 1989; Witter and Amaral, 2004).

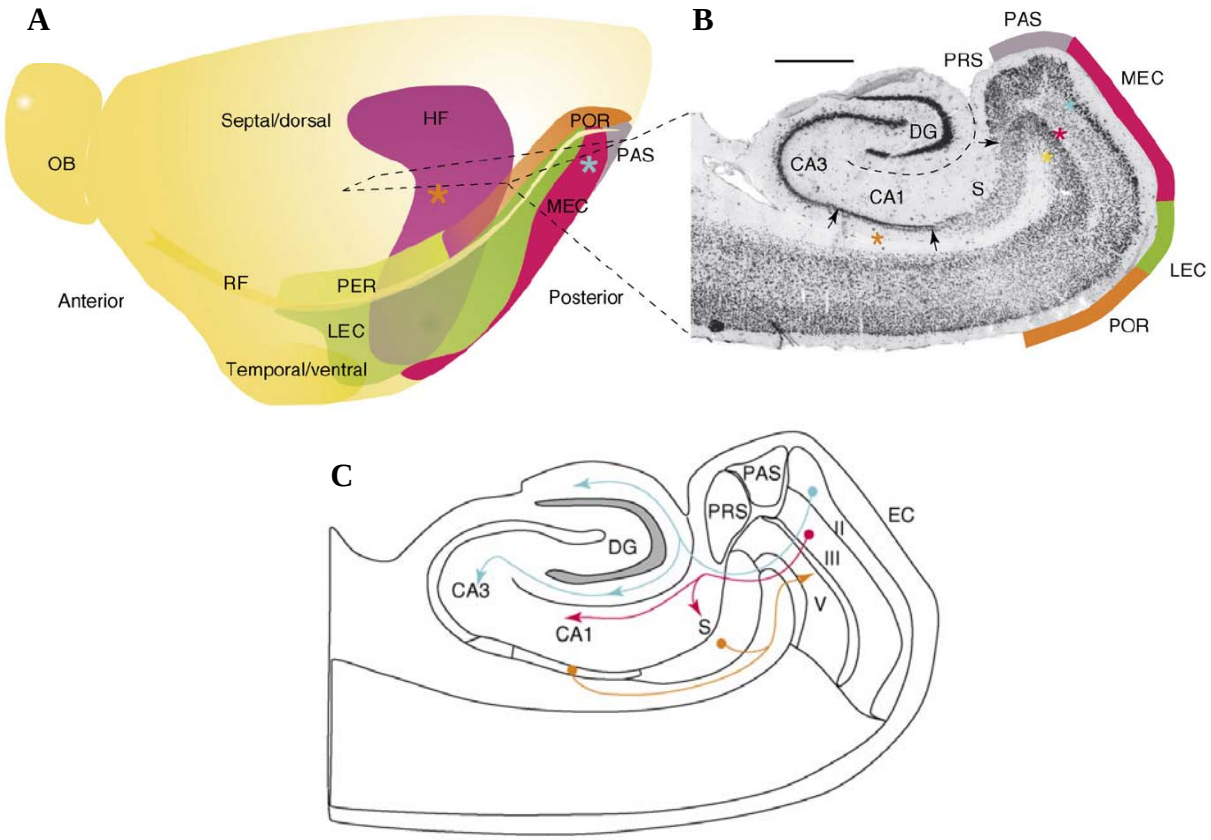

Figure 1-01: The entorhinal cortex (A) Posterolateral view of the left hemisphere of a rat brain, with the hippocampal formation (HF, purple) located deep to the cortical surface. The lateral and posterior cortical surface contains a small indentation, the rhinal fissure (RF), which coincides roughly with the border between entorhinal cortex and perirhinal (PER) and postrhinal (POR) cortices. The entorhinal cortex is subdivided into a lateral (LEC, green) and medial (MEC, red) area. The parasubiculum (PAS, grey–purple) is also indicated. The dashed square indicates the position and perspective of the section shown in (B). (B) Horizontal section illustrating the cytoarchitectonically defined subfields of the hippocampal formation [the dentate gyrus (DG), hippocampal fields CA3 and CA1 and the subiculum (S)] and of the parahippocampal region [the presubiculum (PRS), parasubiculum (PAS), medial and lateral entorhinal cortex (MEC and LEC) and the postrhinal cortex (POR)]. Scale bar: 100 µm. Arrows indicate borders between subfields of the hippocampal formation. **(C)** Main overall wiring of the entorhinal–hippocampal system, illustrated using the same horizontal section as in (B). Cells in layer II (L2) of the entorhinal cortex project to DG and CA3 (blue arrows). Cells in layer III (L3) of the entorhinal cortex distribute their axons to CA1 and the subiculum (red arrows). In turn, neurons in CA1 and the subiculum give rise to the major output projections of the hippocampal formation, targeting layer V (L5; orange arrows) and L3 (not indicated) of the entorhinal cortex (Adapted from Witter and Moser, 2006).

1.4a Medial and Lateral subdivisions

Based on a consensus between two fundamentally different approaches, connectivity versus architecture, the entorhinal cortex (EC) is divided in two parts: the medial entorhinal cortex (mEC) and the lateral entorhinal cortex (lEC) (Witter and Amaral, 2004). On the basis of the

terminal distribution of entorhinal projections in the rat and the mouse, it seems plausible to divide the entorhinal cortex into the two above-mentioned subdivisions. These areas roughly correspond to the description of Brodman's areas 28a and b. Such an anatomical subdivision of the entorhinal cortex supports the hypothesis that this cortical region harbours parallel input/output channels (Witter et al., 1989). In fact, recent electrophysiological recordings in mEC and lEC of the rat have elaborated on this point in showing that cells in the medial subdivision are spatially modulated, whereas in the lEC such modulation is largely absent (Hafting et al., 2005). Cells in the lateral subdivision cortex most likely convey olfactory and somatosensory information (Witter and Amaral, 2004).

1.4b Layered structure

The lamination of the entorhinal cortex is generally considered the prototype of the transition between the three-layered allocortex and the six-layered neocortex. The superficial plexiform or molecular layer (L1) is relatively free of neurons and, in general, contains a dense band of transversely oriented fibers. The outermost cell layer (L2) varies considerably in appearance among the rostro-to-caudal and lateral-to-medial extent, but mainly contains 'stellate' and 'pyramidal' cells. L3 is a wide layer of loosely arranged, large-to-medium sized cells that are predominantly of the pyramidal type (figure 1-02). The deep border of L3 is the cell-sparse fiber layer called the lamina dissecans (sometimes referred to as L4). The lamina dissecans is better developed in the medial entorhinal cortex although species differences are apparent.

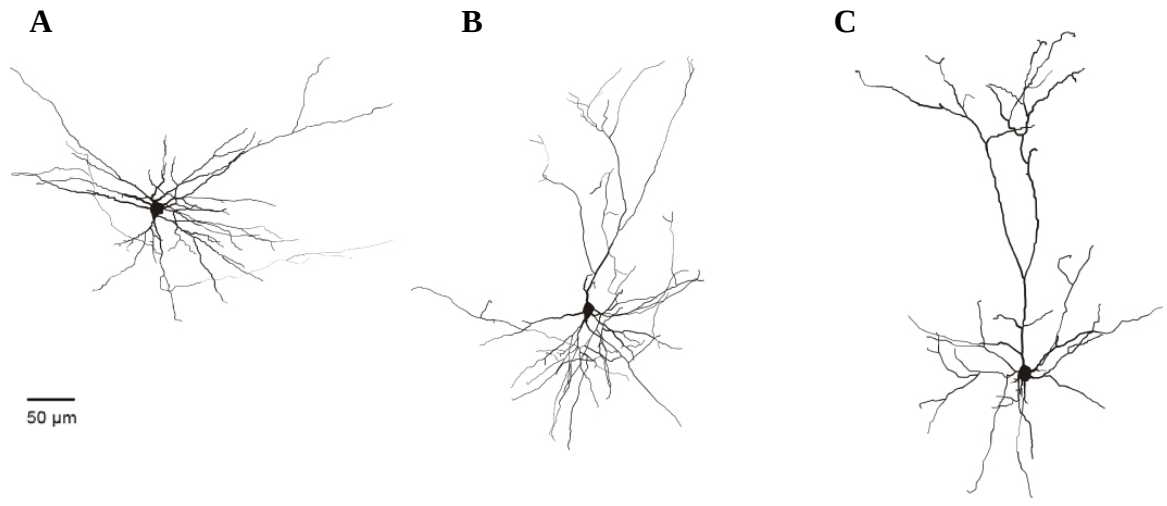

Figure 1-02: Different projection neurons in the medial entorhinal cortex **(A)** Layer 2 stellate cell (L2S) **(B)** Layer 2 pyramidal cell (L2P) **(C)** Layer 3 pyramidal cell (L3P).

The next cell layer (L5) is clearly stratified and sometimes subdivided into a superficial layer of large to medium-sized, darkly stained pyramidal cells, which is sometimes referred to as L5a. Subsequent deeper portions of L5 (L5b/5c) have an overall stratified appearance and mainly consist of rather small pyramidal cells with a moderately dense packing. In the deepest cell layer, L6, which is delineated by the white matter, multiple layers can be distinguished, more in particular in primates. However, since the appearance of L6 is highly variable at different lateromedial and rostrocaudal levels, generally no further differentiation between sublayers is made (Canto et al., 2008).

1.4c Extrinsic and intrinsic connectivity

The connectivity of any cortical region is described by both its extrinsic and intrinsic connections. Extrinsic connectivity of the entorhinal cortex includes entorhinal-hippocampal (figure 1-01C), entorhinal-cortical and entorhinal-subcortical connections. The intrinsic connectivity is the wiring of the neurons in the different layers of the entorhinal cortex between each other. The extrinsic connectivity of the entorhinal cortex to other brain areas have been extensively studied however, till date a gap of knowledge exists in defining the intrinsic connectivity or the local microcircuitry of the entorhinal cortex.

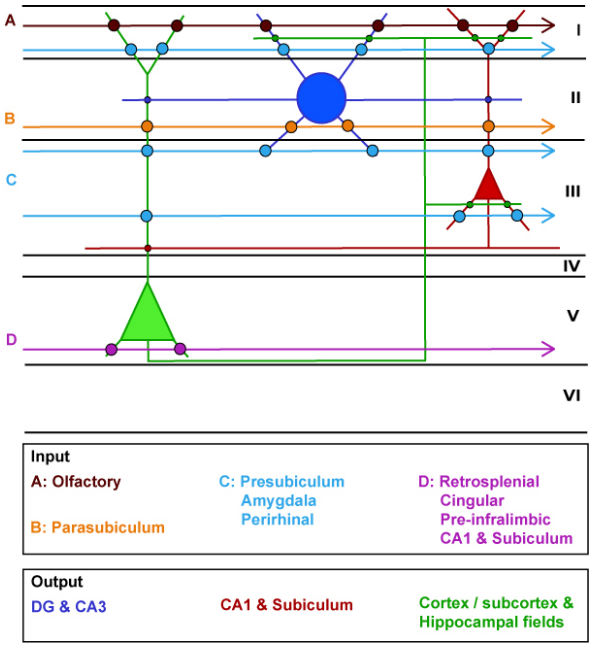

Figure 1-03: Schematic representation of laminar distribution and synaptic interactions between inputs and principle cells of the entorhinal cortex. Different inputs are represented by colour-coded arrows; position of the arrows indicates the main laminar distribution. Circles indicate putative synaptic contacts between inputs and principle cells. Main output connectivity of principle cells is indicated as well (modified from Canto et al., 2008).

Extrinsic connectivity: The superficial layers – L2 and 3 – of the mEC project to the dentate gyrus and hippocampus: L2 projects primarily to dentate gyrus and hippocampal region CA3; L3 projects primarily to hippocampal region CA1 and the subiculum. These layers receive input from other cortical areas, especially associational, perirhinal, and parahippocampal cortices, as well as prefrontal cortex. The entorhinal cortex as a whole, therefore, receives highly-processed input from every sensory modality, as well as input relating to ongoing cognitive processes (Amaral and Witter, 1989; Fernandez et al., 1999; Fell et al., 2001; Van Hoesen, 1982; Witter et al., 1989). The deep layers, especially L5, receive one of the three main outputs of the hippocampus and, in turn, reciprocate connections to other cortical areas that project to superficial EC layers (figure 1-03).

Intrinsic connectivity: The intrinsic connectivity in the entorhinal cortex implies the local connectivity that exists within and among layers of the entorhinal cortex. Neurons in different layers have very different interlaminar and intralaminar connection patterns that include axon collaterals confined to the parent cell layer and those spanning several layers. But not only the axonal distribution is of importance: the dendritic trees may also play an essential role in that they either span several layers or are more restricted to the parent cell layer. Since detailed information for quite a few neuronal types in the entorhinal cortex is still lacking, this second level of intrinsic organization has not yet been incorporated into a working concept about the entorhinal cortex. This is essential however in order to properly understand how inputs to the entorhinal cortex will be processed by the entorhinal network and to understand which information will potentially be conveyed to 1) the hippocampal formation and 2) to other cortical and subcortical areas. One important anatomical observation already reported by Cajal is that neurons in the deep layers are connected to superficial layers by way of axonal projections (figure 1-03; Dolorfo et al., 1998; Hamam et al., 2000; Hamam et al., 2002; Koehler, 1986; Koehler 1988; van Haeffen et al., 2003). These anatomical findings have been corroborated in a number of functional studies (Bartesaghi et al., 1989; Gloveli et al., 1997b; Iijima et al., 1996; Jones, 1994). The majority of the axons from deep to superficial layers are likely excitatory and target both interneurons and principal neurons in almost equal percentages (van Haeffen et al., 2003). This thus constitutes the substrate for powerful excitation as well as feedforward inhibition to neurons in the superficial layers. It should be mentioned here that there is also convincing anatomical and electrophysiological evidence supporting the existence of connections between cells in L2 and 3 (Germroth et al., 1989; Koehler, 1986; Koehler, 1988; Bartesaghi et al., 1988; Bartesaghi et al., 2005; Dhillon et al.,

2000; Tolner et al., 2005a; Tolner et al., 2005b), suggesting that they may function in concert as well.

However, to date, studies elucidating the functional intrinsic microcircuitry by incorporating the roles of the principal cell types of the medial entorhinal cortex are lacking. Focus, thus far, has been on investigating the extrinsic connectivity of the entorhinal cortex with other cortical regions and the hippocampus. But to understand the more independent role of the entorhinal cortex itself, the local intrinsic microcircuitry needs to be understood at different levels of neuronal organization.

CHAPTER 2:

FUNCTIONAL MICROCIRCUITRY OF THE MEDIAL ENTORHINAL CORTEX

Although the structural elements are comparable between cortical microcircuits, each element is incorporated in a specialized way to perform a particular function. For example, the visual and sensory cortices share the similar layered structure, the basic excitatory and inhibitory neurons and the intrinsic wiring pattern. However, each of these cortical areas perform a unique function which lends support to the theory that inspite of the structural stereotypy, there exist differences in functional microcircuitry and synaptic dynamics (Thomson and Lamy, 2007).

It is of further interest to study this functional wiring in the light of pathophysiological states. Several neuropsychiatric diseases (Schizophrenia, Rett's Syndrome, Autism, Fragile X Mental retardation and Alzheimer's disease amongst others; Van Hoesen et al., 1986; Van Hoesen et al., 1991) have been attributed to misconnected microcircuits of the involved cortical area due to developmental or environmental insults. Recent studies have pointed to the possibility of looking at early markers – formation of misconnected neuronal microcircuits leading to an imbalance of excitation and inhibition – for such diseases. It is proposed that by studying these alterations in neuronal microcircuits, it is possible to look at pathological states even before symptoms appear. By investigating the pre-symptomatic signatures of

neuropsychiatric diseases, there exists a possibility to predict and potentially cure the progression of such diseases (Ben-Ari., 2008).

The entorhinal cortex has been implicated in important functions such as spatial navigation, memory processing and in pathophysiology (e.g. TLE, Alzheimer's disease and Schizophrenia amongst others). Thus it is necessary to understand the integrative properties, intrinsic microcircuitry and synaptic transmission of the key projection neurons in the mEC.

2.1 Key functions of the medial entorhinal cortex

2.1a Spatial navigation

The mEC is the main input-output station of the hippocampus. This cortical region has long since been implicated in processes involved in memory acquisition and consolidation. In addition to its classical function as an information hub for the hippocampus, recent studies point to an emerging independent computational function of the mEC – its role in spatial navigation.

The discovery of place cells in the 1970s (O'Keefe and Dostrovsky, 1971) and head-direction cells in the 1980s (Taube et al., 1990) sheds light on how space is represented in the brain. Discharging whenever the rat is in a certain place in the environment, or whenever the rat's head points in a certain direction, these cells are likely to contribute to the brain's systems for local navigation. Soon after their discovery, place cells were suggested to be the elements of a neural representation of allocentric space and the animal's (including rodents, bats and even humans) own position within it, which the animal could use to find its way from one place to another (O'Keefe and Nadel, 1978; McNaughton et al., 1996). The representation was thought to form a map-like framework for storage of experience in memory, a framework referred to as the 'cognitive map' (O'Keefe & Nadel, 1978). However, the conception of the hippocampus as a single dynamic spatial map has been challenged by accumulating evidence suggesting that the very same place cells participate in a number of representations, even in the same spatial location (Bostock et al., 1991). Researchers have also showed that place-specific firing persisted in CA1 neurons even after removal of all intrahippocampal input from CA3 (Brun et al., 2002). Because only direct perforant-path inputs from the entorhinal cortex remained after lesioning the CA3, it was concluded that spatial signals were computed either in CA1 itself or, more likely, in a general metric navigational system upstream of the hippocampus (Brun et al., 2002), a possibility raised early on (O'Keefe, 1976). In response to these challenges, Fyhn and colleagues (2004) recorded directly from layers 2 and 3 of the mEC, in the area that

provided the strongest projections to place cells of the dorsal hippocampus (Witter et al., 1989; Dolorfo & Amaral, 1998). Principal neurons in this area had multiple sharply tuned firing fields that collectively signaled the rat's changing position with a precision similar to that of place cells in the hippocampus. When these cells were recorded in sufficiently large two-dimensional environments, it became clear that the many fields of each neuron formed a periodic triangular array, or 'grid', that tiled the entirety of the animal's environment (figure 2-01; Hafting et al., 2005).

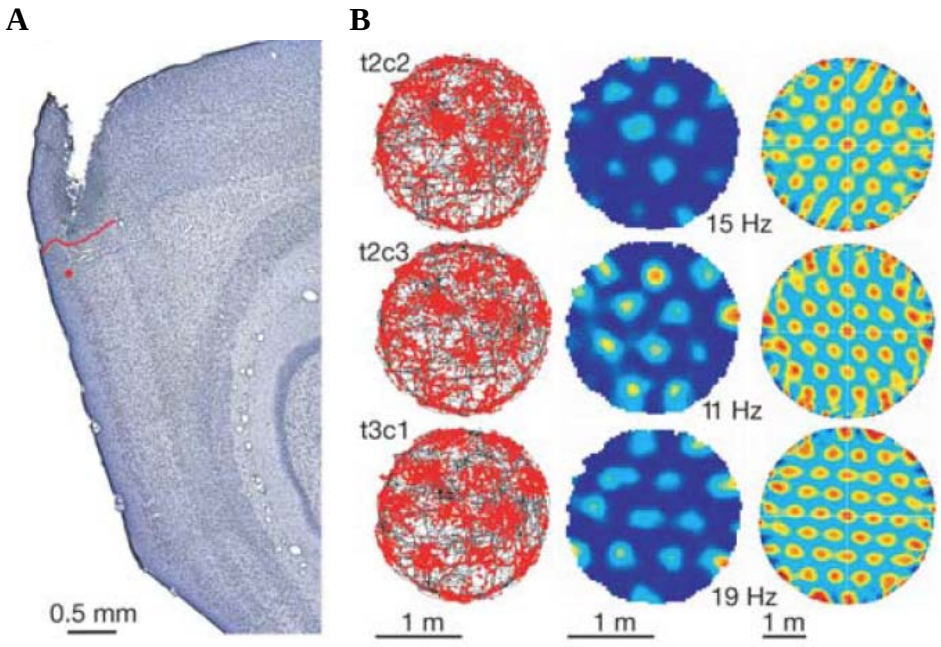

Figure 2-01: Firing fields of grid cells have a repetitive triangular structure **(A)** Sagittal Nissl-stained section indicating the recording location (red dot) in L2 mEC. Red line indicates border to postrhinal cortex. **(B)** Firing fields of three simultaneously recorded cells at the dot in **(A)** during 30 min of running in a large circular enclosure. Cell names refer to tetrode (t) and cell (c). Left: trajectory of the rat (black) with superimposed spike locations (red). Middle: colour-coded rate map with the peak rate indicated. Red is maximum, dark blue is zero. Right: spatial autocorrelation for each rate map. The colour scale is from blue (r = -1) through green (r = 0) to red (r = 1) (adapted from Hafting et al, 2005).

Grid cells may be the key elements of a modularly organized network for metric spatial representation. The neural map is thought to represent self-location based on integration of speed and direction signals during movement. However, this opens up many questions that are fundamental to the understanding of how the grid pattern is generated in single cells, and in neural networks of the entorhinal cortex and beyond. With the introduction of new tools for genetic activation and inactivation of particular circuit components, a deeper understanding of

the intrinsic microcircuitry of the principal cell types and using theoretical modeling it may be possible to decipher the underlying mechanisms.

2.1b Excitability and synchrony

The entorhinal cortex plays a pivotal role in transferring information to and from the neocortex and the limbic regions of the brain (Fernandez et al., 1999; Fell et al., 2001). It has been proposed to act as a major associational area, taking information from many neocortical areas (Van Hoesen, 1982; Amaral and Witter, 1989; Witter et al., 1989). Associating activity from spatially distant brain regions in a single, separate region may be seen as an extension of the binding hypothesis for associating activity in areas coding for separate features of a sensory object. The role of rhythmogenesis (particularly at gamma frequencies) may therefore be seen as a critical tool used by the entorhinal cortex to temporally organize multiple inputs of diffuse spatial origin. Accordingly, the occurrence of gamma oscillation has been shown in *in vivo*, whole brain preparation and *in vitro* brain slices (figure 2-02A; Cunningham et al., 2003; Cunningham et al., 2006; Dickson et al., 2000; Fisahn, 2005; Huxter et al., 2007). However, studies designed to deepen our understanding of the mechanisms used by the entorhinal cortex to generate gamma frequency oscillations have only recently been initiated.

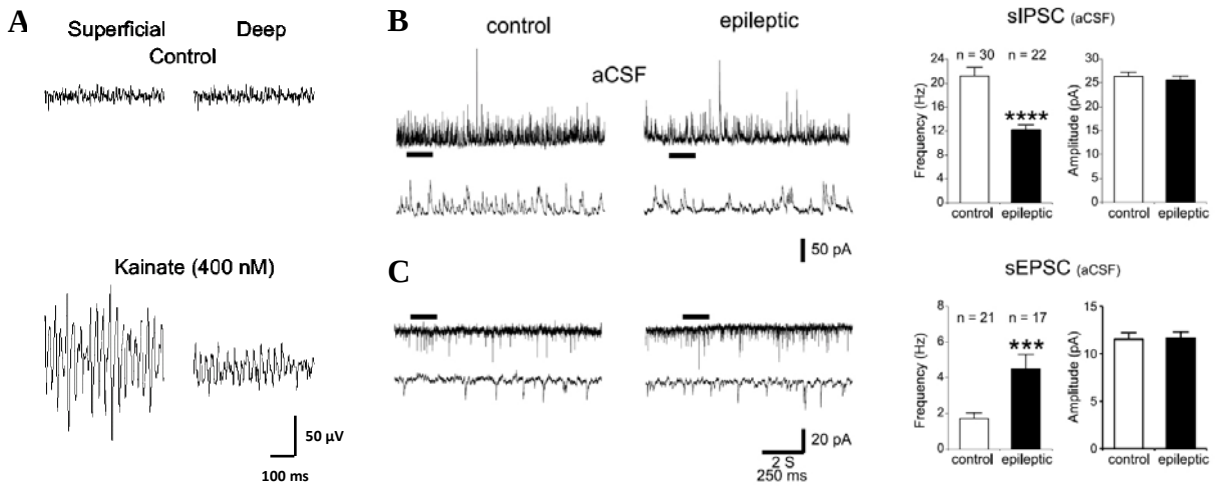

Figure 2-02: Synchrony and hyperexcitability in the superficial layers of the mEC. **(A)** Application of nanomolar concentrations of kainate receptor agonists induced persistent network oscillations in the mEC *in vitro*. Perfusion of kainate (400 nM) generated fast oscillations in the gamma range in the superficial and deep layers of the mEC. Field recordings demonstrate extracellular recordings from superficial and deep mEC during control and 60 min after the initial application of kainate (adapted from Cunningham et al., 2003). **(B, C)** Comparison of spontaneous PSCs of L2Ss between control and epileptic groups. **(B)** sIPSCs (outward events at 0 mV holding potential) of L2Ss in control and epileptic rats recorded in normal aCSF. Bottom traces show time-

expanded views of the regions indicated by bars in the top traces in these figures. Bar plots show the mean frequency and amplitude of the events in the indicated number of cells. Error bars indicate SEM. **(C)** Records and corresponding bar plots of sEPSCs (inward events at -60 mV holding potential) recorded in L2Ss. Error bars indicate SEM. ***p<0.001, ****p<0.0001, t test (adapted from Kumar and Buckmaster, 2006).

Further, if this intrinsic synchrony is off-balance, it results in hyperexcitability. Many studies have pointed to mEC as a focal point of epilepsy. In animal models of temporal lobe epilepsy, L2Ss and L3Ps are hyperexcitable 2-02B-C; Bear et al., 1996; Kumar and Buckmaster, 2006; Scharfman et al., 1998; Tolner et al., 2005a). In addition, diseases like Alzheimer's and schizophrenia could result from misconnected microcircuits in the mEC (Van Hoesen et al., 1986; Van Hoesen et al., 1991). In order to better understand imbalances in excitability arising due to malformed brain circuits, the L3 mEC pyramidal cell is an interesting focus; it assumes a central role given that there is a specific loss of this neuronal population in such pathophysiologies.

2.2 What can we learn from the microcircuitry of the medial entorhinal cortex?

Even though the mEC is implicated in key physiological processes such as spatial navigation and neuronal synchrony, to date little is known about the supporting neuronal microcircuitry and the molecular properties of synapses that are involved in this information processing. Thus, in my doctoral thesis, I was interested in the following:

a) Studying the functional microcircuitry of the projection neurons involved in spatial navigation, namely the layer 2 stellate cell (L2S) and the layer 2 pyramidal cell (L2P; Chapters 3 and 4)

b) Characterizing the role of layer 3 pyramidal cell (L3P) in neuronal synchrony and excitability (Chapter 5)

2.2a L2S and L2P in spatial navigation

The function of the mEC as a spatial navigation unit should be reflected by the intrinsic microcircuitry of the mEC. Two different patterns of associative connectivity can be distinguished in the mEC: 1) recurrent intralaminar connections for parallel processing and 2) 'non-parallel' interlaminar feedback. The ascending interlaminar feedback inputs from deeper layers to the superficial layers play an important role in updating the grid cell network through the integration of position, direction and speed signals. It is unclear if the integrative units,

defined by the microcircuitry, are organized in local circuits as comparable to columns in the neocortex or scattered across the mEC as in the organization of the neighbouring palaeocorical structures like the piriform cortex. Although the formation of modules has been postulated for grid cell function, there is no functional evidence for the columnar association of the mEC microcircuitry.

Projection neurons in L2 are a natural starting point for the analysis of the mEC microcircuitry in light of their proposed role as putative grid cells. In L2 mEC, two biophysically and morphologically distinct projection neurons have been identified, namely the stellate cell (L2S) and the pyramidal cell (L2P). We developed a scanning photostimulation system for studying neuronal microcircuitry and using this were able to investigate the local connectivity pattern of these two projection neurons of L2 mEC.

In Chapter 3, we introduce the available techniques for studying neuronal microcircuitry, the method we chose and the development of the software platform for performing scanning photostimulation experiments. By mapping the intralaminar synaptic connectivity of the mEC L2S as a model cell, the applicability, resolution and reproducibility of the software was validated.

In Chapter 4, we present the main findings of the functional microcircuitry of the two L2 mEC projection neurons. L2 mEC has been implicated in spatial navigation. However, the intrinsic (intralaminar and interlaminar) microcircuitry that is necessary for the flow of information to these cell types is not known. Hence by using the software developed for scanning photostimulation, we mapped the synaptic inputs that each of the cell types receive.

2.2b L3P in excitability and synchrony

Gamma oscillations can be evoked in the entorhinal cortex by applying kainate in nanomolar doses. Several labs have worked out the spatial and temporal organization of such neuronal synchrony in the entorhinal cortex. However, the molecular mechanisms and signaling cascades at the single cell level that could give rise to such oscillations at the network level are not known in detail.

On the other hand, kainate has been used as an epileptic agent in animal models of temporal lobe epilepsy: it causes specific and wide-spread cell loss in the L3 of the mEC. The L3Ps are recurrently connected and are susceptible to neuronal degeneration following systemic application of kainate. However, so far few studies have aimed to decipher the links between the use of kainate as an epileptic substance and the extensive but specific neuronal damage that it causes in the L3 mEC.

In Chapter 5, we look at the effect of kainate receptor-mediated excitability of L3Ps in an effort to understand how kainate is involved in both healthy neuronal synchrony and pathological hyperexcitability. Moreover, the characterization of kainate receptors on L3Ps potentially sheds light on their sensitivity and susceptibility in pathological states. Further, we report on the findings of a novel mediator of synaptic transmission, the deletion of which results in hippocampal network hyperexcitability by increasing synaptic strength. It is clearly of interest to investigate how insults that do occur to a normally functioning neuronal microcircuit resulting in pathological outcomes from the synapse to the circuit level.

CHAPTER 3:

MAPPING NEURONAL MICROCIRCUITRY BY PHOTOSTIMULATION

Neuronal microcircuits are similar in that they use excitatory and inhibitory neurons interconnected with dynamic synapses to embed inherited information on how to execute specific behaviours. Such neuronal microcircuits across various species and brain regions do share a similar repertoire of neurotransmitters, synaptic kinetics and synaptic plasticity. However, each is specialized and fundamentally different in terms of the precise recurrent design used to achieve a specific functionality. Thus much effort has been put in since the initial drawings of neuronal microcircuits by Cajal till date to understand the underlying structure and the corresponding function of brain circuitry.

3.1 Techniques to study neuronal microcircuitry

3.1a Anatomical studies

In addition to providing us with the structural and immunocytochemical details that allow different classes of neocortical neurons to be defined, these studies demonstrate the layer(s) in which each type of neuron receives its inputs and the layer(s), cortical regions and/or subcortical structures to which each type projects. In some ultrastructural studies, it has been

possible to identify both the presynaptic and the postsynaptic neurons involved in particular classes of connection. However, this requires markers, identifiable at the electron microscope (EM) level that unambiguously identify the presynaptic and the postsynaptic elements. This has been achieved in some cases by combining Golgi, or HRP staining of one cell and immunocytochemical labeling of a population of potential targets. Some studies have relied on recognition of postsynaptic subcellular elements such as somata, axon initial segments, and dendritic spines at the ultrastructural level. In others, retrograde labeling of a population of axons and thus their parent neurons has been combined with lesions to promote degeneration of axons and terminals in the recipient region studied. Both the filled neurons and the degenerating terminals can then be identified at the EM level.

Larger-scale information about projection patterns between layers and across columns has been obtained from populations of neurons labeled by uptake of dye from an extracellular injection in vivo, providing the basis for many predictions of connectivity patterns. However, only a few of these studies have identified the specific cellular and subcellular targets of these projections beyond, for example, the proportions that involve dendritic spines or shafts. In the future, techniques using a trans-synaptic tracer based on rabies virus that can label multiple presynaptic neurons from the transfection of a single postsynaptic neuron may further the understanding of neuronal microcircuitry.

3.1b Fluorescent mice – GFP constructs

An increasingly utilized approach is the use of genetically modified mice in which the expression of green fluorescent protein (GFP) is linked to the promoter for a selectively expressed protein such as GAD-67 (Yuste, 2005 for review). Following careful comparison of the expression of markers in the GFP-labeled neurons with markers in unlabeled cells, it has been possible to identify a number of mouse lines that express GFP only in certain subpopulations of neurons. The cells expressing GFP can be visualized in the slice and recordings targeted specifically to certain subpopulations of neurons. Apart from the need, common to most transgenic studies, to use mice rather than the previously better documented rat, the common criticism of this approach is the potential for damage to the neurons when the GFP is excited.

3.1c Focal flash photolysis of caged glutamate

This approach employs an intracellular/whole-cell recording from one neuron in an *in vitro* slice while many different regions of that slice are activated sequentially by uncaging

glutamate (e.g., Callaway and Katz, 1993; Schubert et al., 2001). Small volumes of the slice can be selectively activated by the glutamate released by a highly focused light beam (Yoshimura et al., 2005). The glutamate is then rapidly removed by diffusion and by uptake mechanisms. Cells in the activated area that are presynaptic to the recorded neuron and that reach firing threshold, generate postsynaptic potentials in that cell. Maps of the regions containing these presynaptic neurons can thus be generated, with relative input strengths. The structure (and therefore class) of the single postsynaptic recorded neuron is revealed by biocytin-labeling and subsequent histological processing. It is typically not possible to dissect postsynaptic responses to determine how many neurons contributed, to identify the presynaptic cell class(es) involved, or to biophysically characterize each contributory input. Kinetics of the synaptic response often cannot be characterized in the usually occurring compound signals since it is not clear whether later responses result from continued firing of the activated neuron(s), or different inputs. It does, however, provide valuable information about connections on the population level that have not been documented with other methods, particularly the density of inputs to specific cell types from other cortical layers. Source-cell specific comparisons of the strengths of inputs to a single neuron from many areas of the slice can be obtained more efficiently with dual recordings. A recent review compares this technique with others used to study cortical circuitry (Schubert et al., 2007).

3.1d Ca^{2+} indicator methods

Circuits of connected neurons can be studied by driving one recorded neuron to fire and using calcium imaging to identify the positions of other neurons activated by that cell (Peterlin et al., 2000). An indication of the numbers of 'follower' cells in a given area of the slice that are activated by one presynaptic cell can be obtained, but they cannot be identified further and the electrophysiological properties of the synaptic events are not accessible. The obverse can also be applied, i.e., recording from one neuron, identifying the spontaneous activity of other neurons with calcium imaging and using reverse correlation to identify the putative presynaptic neurons whose activity correlated with postsynaptic potentials in the recorded cell (Aaron and Yuste, 2006). Like the caged glutamate studies, these techniques can identify regions from which significant input to the recorded cell originate. With sparse presynaptic firing, they can reveal more about the properties of individual connections and to an extent also identify the class(es) of presynaptic neurons involved (Nikolenko et al., 2007).

Developments in imaging technology and methods such as the use of GFP labeling of specific interneuronal subclasses (Yuste, 2005 for review) have made significant contributions to this

field. Technical approaches that are being developed to improve the time and spatial resolution of scanning techniques are reviewed by Saggau (2006) and Yasuda (2006) and the ways in which techniques such as (fluorescence resonance energy transfer) (FRET) and fluorescence lifetime imaging microscopy (FLIM) may be applied to imaging molecular level events occurring in neuronal subcompartments (Okamoto et al., 2004; Yasuda et al., 2006). Although we are still dependent upon a range of traditional techniques for most of our current understanding of circuitry, these developments in confocal and two photon technology are likely to provide considerable insight in the future.

3.1e Activation of specific cell classes by a light-activated cation channel and inhibition with a light-activated chloride pump

Transgenic mice that express the light-activated cation channel Channelrhodopsin-2 (ChR2) in subsets of neurons may provide an important tool for the future. Illumination of ChR2-positive neurons in brain slices can drive them to fire and generate postsynaptic potentials in recorded target neurons (Zhang et al., 2006). In a recent report, Chr2-YFP fusion protein was placed under the control of the regulatory elements of the mouse Thy1.2 gene and was expressed at high levels in, for example, layer 5 pyramidal cells (Wang et al., 2007). In the future, genetic targeting of ChR2 expression to different neuronal classes will allow their selective activation and the accurate mapping of the inputs from one class of neuron to one, or several recorded neurons. This will provide an advantage over the caged glutamate studies in identifying the class of presynaptic neuron involved. This approach has also been applied to functional tracing of longer distance pathways in vitro (Petreanu et al., 2007) and in vivo (Arenkiel et al., 2007). A light-activated chloride pump, NpHR, which suppresses neuronal activity, can also be transfected into specific cell classes. It can be targeted together with ChR2 which is activated at a different wavelength. Integration of these tools with calcium imaging may even provide a totally optical method for investigating circuitry in vivo (Han and Boyden, 2007; Zhang et al., 2007).

3.1f Dual/multiple recordings of synaptically connected neurons

Paired or multiple recordings of synaptically connected neurons provide access to very detailed information of the unitary properties of the connection and their short-term plasticity (Feldmeyer et al., 1999). Since both, the pre-and the postsynaptic neuron can be stained, the number and location of the synapses responsible for the established functional properties can be determined as well. However, with paired recordings one is usually restricted to studying

neurons that are very closely located to each other, and only a few neurons (the highest published number being 4; (Gupta et al., 2000) can be examined in one experiment. These spatial and numerical limitations make it impossible to obtain an overview of the entire pattern of connectivity, especially of the transcolumnar, in a single column (which is estimated to consist of some 10,000 neurons) in a single preparation. For this reason it is desirable to also use a complementary method like computer-controlled mapping of functional connectivity with sublaminar resolution by uncaging glutamate.

3.2 Our approach: scanning photostimulation (optimized focal UV photolysis) to study neuronal microcircuits

Scanning UV-photostimulation, originally introduced by Katz and Dalva (1994), has become a well-established method in neurophysiology (Callaway and Yuste, 2002). Its application ranges from the analysis of neuronal connectivity of local brain circuits (Brivanlou et al., 2004; Jin et al., 2006; Lam et al., 2006; Schubert et al., 2001, 2003, 2006; Shepherd et al., 2003) and the functional characterization of synapses (Godwin et al., 1997; Kandler et al., 1998) to measurements of the distribution of specific receptors on the surface of neurons (Dodt et al., 1998; Frick et al., 2001) and the investigation of dendritic integration (Shoham et al., 2005). Despite this wide scope of applications, the common idea shared by all photostimulation experiments is the coordinated spatio-temporal conversion of an inactive 'caged' transmitter to an activated 'uncaged' transmitter by a transient and highly energetic mostly ultraviolet light beam, while simultaneously recording from one or more neurons. Since photolytic activation provides a fast way to produce perturbations in a chemical system without using an invasive mechanical instrumentation (Lester and Nerbonne, 1982), it is perfectly suited to analyze neuronal networks and their complex interactions.

For investigations of the qualitative assessment of connectivity patterns between brain regions (Dantzker and Callaway, 2000), a high resolution of photostimulation in the range below 10 µm is not critical. In contrast, for mapping experiments aiming to quantitatively estimate synaptic conductances, the diameter of the laser spot has to be decreased to permit for finer stimulation patterns (Dodt et al., 1998). Stimulation of neurons at the single-spine level, where the focal uncaging volume needs to be small enough to mimic glutamate release in the synaptic cleft, can only be achieved using a two-photon-laser based uncaging system (Losonczy and Magee, 2006; Matsuzaki et al., 2004).

However, larger focal uncaging volumes inherent to one-photon based uncaging systems are sufficient to investigate subcellular properties such as the distribution of receptors on the cell surface with a spatial resolution on the level of several µms (Frick et al., 2001). This spatial resolution of the optical stimulation can be achieved by conveying laser light via thin fiber glass cables in combination with focusing of the laser beam via the microscope optics. Since there is a physical limit to the minimal spot size when using low-magnification objectives, further increases of the resolution of stimulation require a high-magnification factor (60× or 40× objectives) with a high numerical aperture. The photostimulation system presented here was designed to provide maximal flexibility by combining high-magnification objectives with low magnification (2.5–5×) overviews for planning scans. The key concept was to plan the stimulation process graphically on the basis of a low-magnification planning image, while performing the stimulation with a high-magnification objective.

Depending on the quality of the slice preparation and the slicing angle, long-range axonal projections between adjacent brain regions (e.g., cortico-thalamical projections) can be preserved (Agmon et al., 1991), and scanning patterns for stimulation can be efficiently projected onto remote structures of interest (Bureau et al., 2006). The user-interface permits for an efficient temporal workflow of the experiment. The acquired data points are recorded and documented by the software.

With the software solution presented here, a standard electrophysiology setup can be converted to an uncaging system by using a versatile range of different commercially available hardware components. In comparison to equally performing galvanometric mirror-based scanning devices which direct a coherent light beam from a high-power laser to the back aperture of a low-magnification objective (Bureau et al., 2006; Shepherd et al., 2003), one only needs an electrical shifting table (which is a standard piece of equipment on most electrophysiology setups) and can use much weaker (and therefore less expensive) light sources. Moreover, when using galvanometric-mirror-based scanning devices the implementation of a fixed raster at low magnification will not permit for the control of the focal depth of the stimulation, which is compensated for by the use of a cylindrical light beam (Shepherd et al., 2003).

To exemplify possible applications of the system, the synaptic connectivity of layer II stellate cells (L2S) of the mEC was mapped. L2S axons form the main output of the mEC to the dentate gyrus via the perforant-path (Steward and Scoville, 1976). The mEC has been considered to be a possible central point in the neural circuitry for spatial representation. The key architectural features of the mEC are recurrent connections and a strong interlaminar

connectivity (Witter and Moser, 2006), two features predisposing this brain region for epileptogenesis (Kumar et al., 2007) and resulting in a high level of synaptic background activity. We also present a basic concept for automatized analysis of the data acquired by the presented software system.

3.3 Design of the control software

The control software Lucifer monitors and controls the connected devices, allows for planning of the experiment, coordinates the stimulation process and manages automatic data storage. The acquisition of data is conceptually separated from its subsequent analysis. Therefore all data and necessary program parameters are documented in a standardized manner and can be exported into a different analysis environment. Another important objective is the temporal efficiency of the experimental workflow, since the integrity of the neuronal tissue as well as the stability of a whole-cell patch decrease with time. For this purpose the software provides a graphical user-interface that allows online control of the experiment. This section describes the functionality of the control software. One key objective of the software design was to plan the stimulation process on the basis of a planning image providing an overview of a part of the tissue the size of which should only be limited by the intercellular circuitry preserved in the slice preparation. Moreover, sites of stimulation should be freely definable in this planning image to enable the experimenter to precisely select any given substructure of interest. The direct overlay of stimulation markers and the overview image greatly facilitates the a posteriori identification of the stimulation sites. This obviates the need for post-experimental definition of alignment sites by for example light-induced burning of the tissue (Brivanlou et al., 2004; Dantzker and Callaway, 2000).

The software offers two main functions: First, the high-precision three-dimensional control of the shifting table in real-time. Secondly it provides for the planning of the stimulation pattern, its execution and documentation. This conceptual dichotomy is represented by two screens, the navigation and stimulation screen.

3.3a Navigation screen

The navigation screen is intended to serve two purposes: (1) To monitor and manipulate the position of the laser beam in relation to the specimen. (2) To construct a planning image. To monitor online the position of the point of stimulation, the center of the navigation screen displays a digitized live image stream recorded by the camera (figure 3-01). By clicking into

the video screen a visually identified target structure is centered in a definable screen position that represents the focus of the stimulation spot. Left to this screen there is a control panel that allows the positioning of the shifting table at different motor speeds in three dimensions.

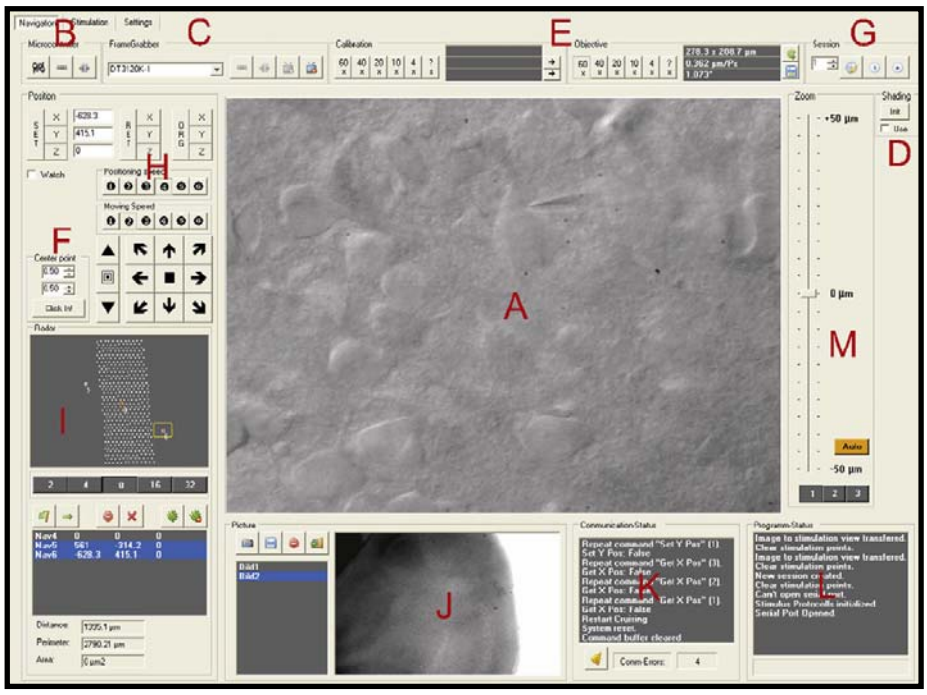

Figure 3-01: The navigation screen. The center video screen (A) displays the live image stream from the video camera. The buttons above the screen enable connecting to the shifting table (B), controlling frame-grabber internals (C), shading correction (D), adjustment of the software to the microscope magnification (E), redefining of the center of the stimulation spot (F) and managing the data acquisition (G). Steering of the shifting table is controlled by the panel H. Within the radar panel (I) navigation and stimulation points are displayed to aid orientation in the XY-plane. Additionally, panels for managing photos (J), displaying the communication with the shifting table (K) and documenting the program status (L) are provided. A vertical slider (M) controls the Z-axis of the table, i.e., the plane of focus of the laser beam.

Geometrical relations of the specimen are imported into the image data via the definition of navigation points that are defined by the three-dimensional coordinates of the shifting table and, hence, the microscope optics. By means of these navigation points the control software calculates distances, areas and perimeters of optical structures.

An overview of the spatial relations between navigation points on the specimen in the XY-plane is provided by an additional radar panel. To obtain a spatially extensive planning image with a high resolution, several overlapping high-resolution images from this region have to be stitched together. Navigation points thereby provide the necessary orientation by defining the

spatial extent of the region of interest. The compound images resulting from the stitching procedure can then be transferred to the stimulation screen.

3.3b Stimulation screen

The stimulation screen serves for planning of the stimulation procedure (figure 3-02). In contrast to the navigation screen, where the current microscope view is displayed as a continuously updated video stream, the planning image in the stimulation view is static.

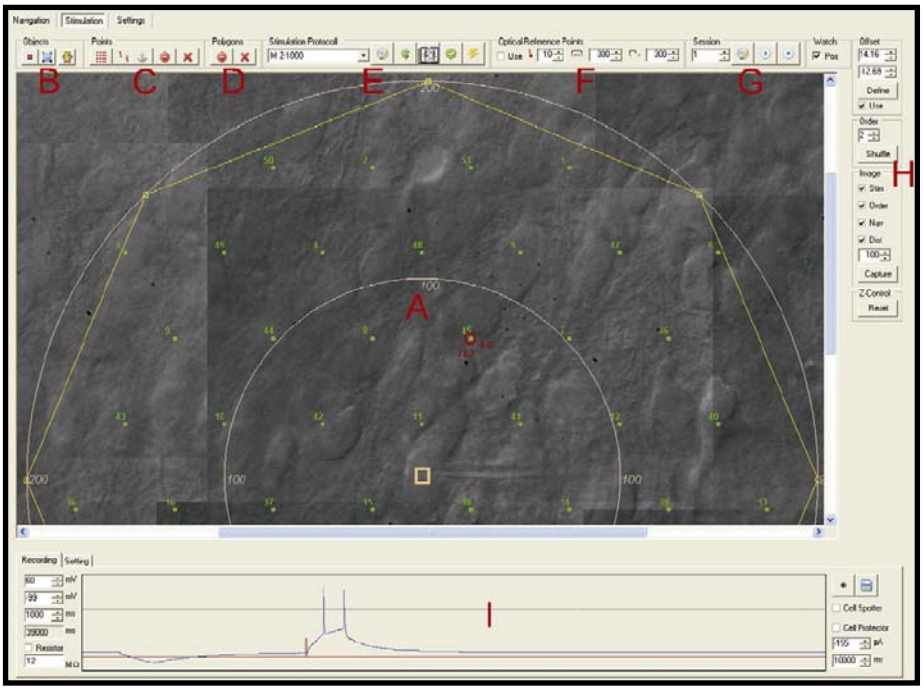

Figure 3-02: The stimulation screen. The stimulation process is planned graphically within the planning image (A). Several functions are available that enable the generation and management of graphical objects (points, polygons, stimulation protocols) (B–E), the definition of optical reference points (F, see below) and the initiation of the stimulation process (G). The recording panel (I) displays the latest recorded signal (blue) and its associated stimulus protocol (red).

Stimulation points are drawn directly into the planning image. Each stimulation point is assigned a number that indicates its rank during the stimulation process. This sequential order, however, can be changed arbitrarily. Each stimulation point is then associated with a particular stimulation protocol that defines the temporal pattern of the stimulation carried out at each point. For manual stimulation the position of the laser spot can be changed in the planning image.

3.4 Scanning process

During stimulation, coordinates of the stimulation points are transformed into the motor coordinates that determine the corresponding position of the microscope optics. In addition to triggering the predefined optical stimulus protocols at the predefined loci of stimulation, the control software also records, displays and stores the point-specific electrical signals of the patched neuron.

3.5 Optical reference points

Due to the inherent inaccuracy of a mechanical system and the non-stationarities in the tissue preparation, the mismatch between the positions on the camera image and the corresponding motor coordinates increases with time. To compensate for this increasing inaccuracy, the control software offers the possibility to define so-called optical reference points. There the idea is to retain the image region surrounding a stimulation point within the current video screen to serve as a template pattern for later comparisons.

Generally, a stimulation point is defined by its corresponding motor coordinate. If the stimulation point is defined as an optical reference point, then an additional correction step is performed after the coordinate is reached: The clipping from the planning image is matched with the live image by minimization of a mean-square error cost function. The corresponding deviation from the center point is compensated by a correction step of the shifting table. Since all points are referred to by relative motor coordinates with respect to their predecessor, all points benefit from these intermittent optical corrections.

3.6 Two-objective method

For experimental designs demanding the exact stimulation of substructures like brain nuclei, cortical layers or columns while recording from relatively remote structures, it is necessary to generate planning images using a low-magnification objective. This greatly facilitates the identification of the subregions necessary to conduct an efficient experiment. To permit the combination of a high-magnification objective for patch-clamping and stimulation on the one hand and a low-magnification image for online planning and navigation, the system offers the possibility to combine both advantages via the two-objective method.

The two-objective method requires the following steps:

1. Using the 60× objective the tip of a patch pipette is positioned in the optical plane and centered in the real-time image. The coordinates of the microscope stage are then set as the origin at the tip of the pipette.
2. Using a 4× objective, a sufficiently large planning image containing the tip of the pipette is created and transferred to the stimulation screen. Since there is a spatial offset between both objectives, the previously defined origin of the microscope stage and the optical position of the pipette tip are no longer identical under the 4× objective. By selecting the tip of the pipette with the mouse arrow within the planning image the spatial offset can be determined.
3. Finally, again using the 60× objective an appropriate target cell can be searched and patched, while planning can be done independently using the low-resolution planning image.
This method has the advantage that only one change of the objective is necessary for each slice. The planning image can be used for patching several cells sequentially, and no additional objective change is necessary after the patch is established. The disadvantage of this method is that no optical reference points can be defined, since both planning and real-time image have different magnification factors.

3.7 A posteriori visual identification of optically stimulated targets

In the two-objective method, no further high-resolution graphical information about the locus of optical stimulation is available. To solve this problem we have included a software tool taking an image from the live view at each stimulation point immediately before the optical stimulation is evoked. This additional graphical information can then be used to assess the quality of the recorded brain slice. Furthermore, the images from a first trial can be used as optical reference images in a second trial, therefore providing the possibility to repeat the stimulation at identical stimulation points and increasing the precision of repeated stimulation trials.

3.8 Effective resolution of the system: photo-induced spatial response profile

The major aim of mapping experiments is to identify the locations of presynaptic cells. Therefore it is necessary to know the spatial relation between stimulation site and location of the cell soma. With their dendritic and axonal arbors, neurons spread over large distances. In order to determine the resolution of our photostimulation, we characterized the photo-induced

spatial response activity of the two principal L2 projection neurons in mEC – stellate (L2S) and pyramidal cells (L2P; Alonso and Klink, 1993).

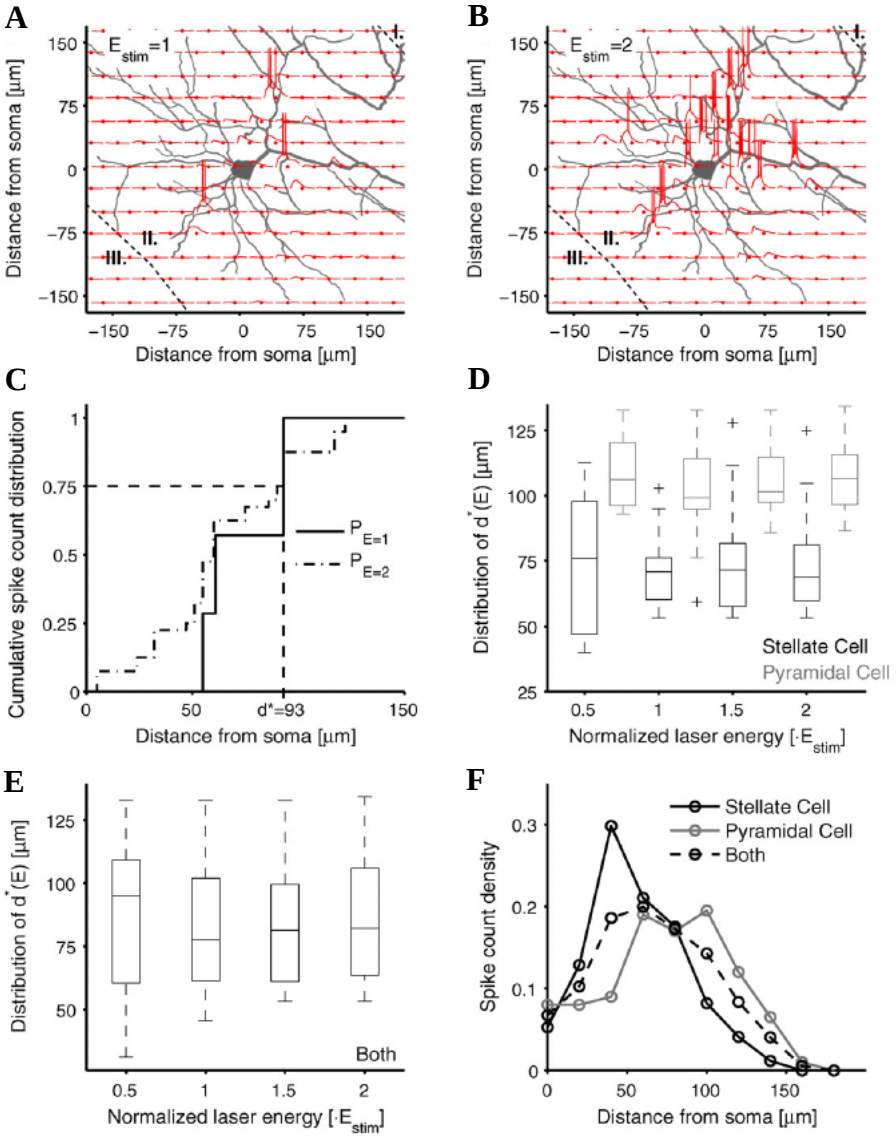

Figure 3-03: Photo-induced spatial response of a single neuron. **(A)** To characterize the photo-induced response activity (red voltage traces) of a current-clamped neuron (gray coloured biocytin reconstruction of a L2S) as a function of the laser spot position relative to its soma, a grid of points (distance 30µm) around the soma is consecutively photostimulated with laser energy Estim = 1. Suprathreshold activations are mainly evoked perisomatically. Cortical layers 1-3 are indicated by dashed lines. **(B)** Same as in A for stimulus intensity step Estim = 2. All hotspots identified in A show a higher activation level and some subthreshold activations become suprathreshold. The activation profile does not indicate a clear relationship between the hotspot position and the degree of dendritic thickness. **(C)** Cumulative spike count distributions as a function of the distance from soma. The critical value d* defines the distance from soma in which 75% of the spikes are evoked. **(D)** Boxplot of the distributions of d* as a function of the laser energy in arbitrary units for L2Ss (black, n= 27) and L2Ps (gray, n= 18). Boxes show median and the 25% and 75% quartiles. **(E)** Distribution of the critical distance d* after pooling over the two cell types. The energy Estim = 1 results in the smallest median d*. **(F)** Spike count density as a

function of the distance for both excitatory cell types separately and together obtained with a laser energy of Estim =1.

We therefore performed current-clamp recordings of L2S (n = 27) and L2P (n = 18). The hexagonal grid of stimulation points had a raster point distance of 30 µm and covered a region with a 150 µm radius around the soma. The point-specific recordings were quantified by the cumulative spike count distribution as a function of the distance from the soma (figure 3-03C).

For the distributions, a critical distance d* was defined below which we found 75% of the total amount of evoked spikes. A small d* results in a smaller activation diameter of a single cell (Shepherd et al., 2003). To illustrate the effect of the light energy onto the critical distance d*, the distribution of d* is plotted as a function of the stimulus intensity level in figure 3-03D. We stimulated at several laser intensities, starting at a low stimulus intensity level of Estim = 0.5 and increasing in steps of 0.5 to a maximum intensity of Estim = 3.

The median of d* across the two cell populations varies only slightly for different energy levels. The median d* ranged from 68.8 µm to 75.9 µm for L2Ss and from 99.2 µm to 106.5 µm for L2Ps. The response profile of L2Ss is characterized by a higher resolution of activation, e.g., for the light energy Estim = 1 the distribution of the critical value d* has a median of 70.8 µm (interquartile range: 16 µm) for L2Ss, and a median of 99.2 µm (interquartile range: 19.4 µm) for L2Ps. To identify the optimal stimulation energy, we also assessed the distribution of the critical distance d* for both excitatory cell types together. As illustrated in figure 3-03E, the stimulation energy Estim =1 induces the smallest critical distances of 77.5 µm (interquartile range: 40.7 µm) and is henceforth used for the mapping experiments.

We also quantified the average spatial response profile of the two excitatory cell types. The spatial activation region shows no statistically significant differences as a function of the orientation angle of the stimulus point relative to the cell soma. The radial spike-count distribution as a function of the distance between stimulation site and soma is shown in figure 3-03F: L2S have a sharp peak response at 40 µm, whereas the pyramidal cell profile is characterized by a flat peak between 60 µm and 100 µm. Both response profiles document that the soma is not the region with the highest glutamate sensitivity. This can be found at a perisomatic region that ranges from 28.5 µm to 66.5 µm for L2Ss, and from 56 µm to 107 µm for L2Ps. We also plotted the response profile averaged over the two excitatory cell types

(figure 3-03F). The region of highest response activity covers the perisomatic region from 37.5 µm to 80 µm.

In mapping experiments without optical control of the stimulated neurons, we cannot distinguish between the activated cell types. The spatial resolution is therefore set by the cell type with largest critical distance d*.

3.9 Mapping the functional connectivity of L2S

In this section we analyze the pattern of the intra-layer connectivity of L2Ss. The cells were held in voltage clamp at the resting potential of −60 mV (for setup details and methods please refer to Appendix A; figure 3-04A). In order to reveal both EPSCs and IPSCs, a low-chloride intracellular solution is used (Pouille and Scanziani, 2001). The stimulation regions extended over the whole L2 mEC and cover up a region of about 1.25 mm × 0.25 mm.

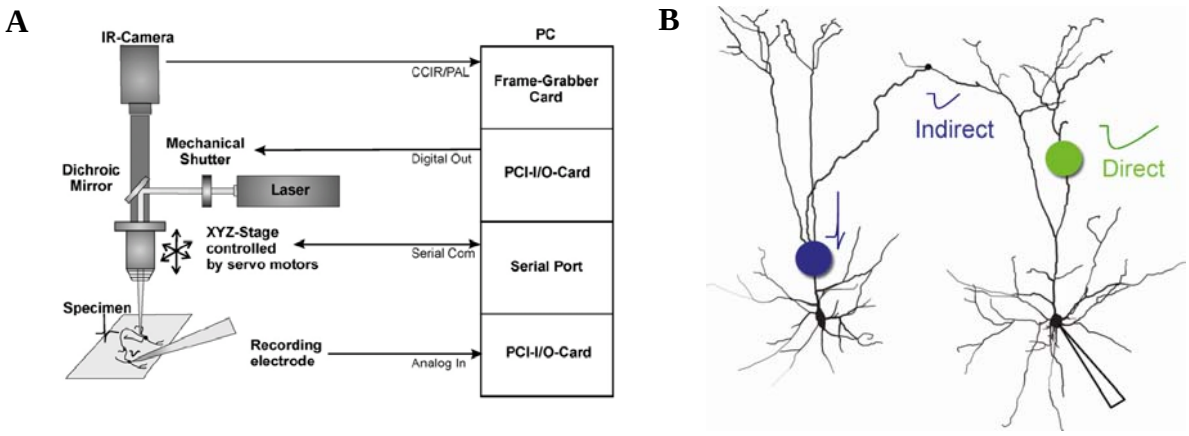

Figure 3-04: (A) The setup (left) is controlled by a personal computer (right). The laser spot is transferred to the specimen via the microscope optics. The light beam is guided through a flexible fiber optics from the laser to the microscope, where it is deflected via a dichroic mirror and then focused by the objective lens. The admission of light onto the tissue is regulated by an external mechanical shutter system controlled by a computer-internal PCI-I/O card. The microscope optics and, hence, the laser spot is positioned by amotorized XYZ-shifting table, whose axis are each equipped with a high-precision step motor, so that the specimen and the noise-sensitive recording electrode remainsfixed. The mutual communication between XYZ-stage and computer is realized using the serial communication port. The analog signal of the recording electrode is digitized by the PCI-I/O card. For the optical control of the experiment an IR-camera is mounted on the top of the microscope. The camera generates an analog video signal in the CCIR/PAL-format which is read out by a computer-internal frame-grabber card. **(B)** Intracellular recording during photo-induced uncaging of a glutamate compound consist of two types of signals: 1) Direct responses (in green) due to the activation of glutamate receptors at the recorded cell. 2) Indirect responses (in blue) due to a supra-threshold activation of a synaptically connected cell.

3.9a Stimulation protocol

At each stimulation point an intracellular current signal of 600ms duration is recorded with a sampling rate of 5 kHz. For the subsequent analysis the recorded signal is divided into four time intervals (0, Ia, Ib and II) as illustrated in figure 3-05A. In time-interval 0, which has duration of 150 ms, a test stimulus of 4 mV is delivered and used to calculate the access and input resistance. At the beginning of time-interval II, at time t = 300 ms, a 2 ms light stimulus is applied.

3.9b Classification of signals: direct, indirect photo-induced and spontaneous PSCs

PSCs detected in time-interval II are considered as photoinduced signals. Specifically, signals that appeared within the first 5 ms after light initiation are classified as direct signals, PSCs that occur later in time-interval II are classified as indirect photoinduced signals (figures 3-04B and 3-05). Direct signals / responses are evoked when glutamate is uncaged activating glutamate receptors on the soma or the dendrites of the cell that is being recorded from (figure 3-06A). Therefore the time to onset for a direct response is immediately after the light stimulus (yellow bar in figure 3-05). Indirect signals / responses are putative synaptic inputs as the uncaged glutamate evokes a spike in a presynaptic cell thereby producing a synaptic input upon the cell being recorded from (figure 3-07). To assess the spontaneous activity, PSCs are also detected and classified as spontaneous signals in the time-intervals Ia (150 ms duration) and Ib (214 ms duration) which surround time interval II (figure 3-05C-D).

3.9c Specifying time windows

When uncaging glutamate, it is necessary to distinguish between direct activation of receptors on the patched cell and indirect suprathreshold activation of a cell presynaptic to the patched cell based on the time window after the uncaging pulse (Schubert et al., 2001). The critical time window for separating between direct and indirect photo-induced signals was determined by a spatial criterion in which the separating point of time after light application was gradually decreased until a solitary region emerged for the first time representing the direct activation of the cell. Consecutively, the so defined time window was verified by TTX control experiments in which the synaptic transmission was blocked. As illustrated in figure 3-06B, the direct activation profile remains virtually identical while the excitatory synaptic input is blocked.

For specification of time-interval II in which incoming PSCs are classified as photo-induced PSCs, the averaged PSC rate during processing the stimulus protocol is computed as a

function of time (figure 3-05E). Only those cells were included into the analysis, in which the PSC rate exhibits a significant ($p < 0.05$) increase after light application (n = 17/20). As illustrated in (figure 3-05E), the time-interval Ia preceding light application is characterized by an almost constant rate of PSCs. The mean PSC rate of this time interval defines the spontaneous activity during the stimulation experiment (ν = 3.4 Hz; green solid line in figure 3-05E).

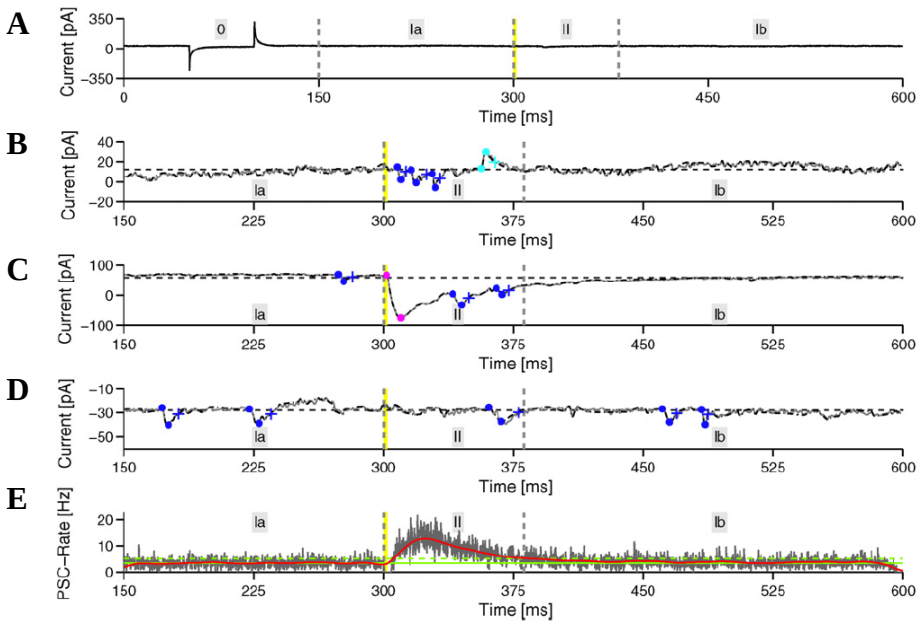

Figure 3-05: PSC-detection and classification. **(A)** At each stimulation point a point-specific signal of 600ms duration is recorded and divided into four time-intervals (0, Ia, Ib and II). Time-interval 0 displays the test pulse used to monitor the recording quality. At the beginning of time-interval II, at time t = 300 ms, the light stimulus (yellow bar) is applied (duration 2ms). PSCs detected in II are termed photo-induced signals, PSCs arriving in time-intervals Ia and Ib are classified as spontaneous signals. **(B–D)** PSCs are detected by an iterative algorithm described in Appendix A. In order to improve the detection, small fluctuations in the original trajectory (gray trace) are substituted by interpolating splines (black trace). The algorithm determines the baseline (dotted line), initiation and peak (points) of the PSC and the decay time constant (cross). Furthermore it distinguishes between direct PSCs (magenta), indirect EPSCs (blue) and indirect IPSCs (cyan). Unlike the sample in (B), the recorded signals in (C) and (D) exhibit spontaneous EPSCs. **(E)** To obtain a criterion for the duration of section II, the averaged point-specific PSC-rate is plotted as a function of time (gray trace, bin size = 0.2 ms, n = 17/20) and smoothed with a Gaussian filter (σ = 5 ms, red trace). The mean rate of time-interval II defines the spontaneous PSC-rate of 3.6 Hz (green solid line). Immediately after light application the PSC rate increases rapidly, reaches its maximum after 23 ms, declines slowly and goes back to the rate of spontaneous activity 167 ms after stimulus onset. The time window in which the PSC rate is one standard deviation (σ = 1.8 Hz) above the averaged spontaneous PSC rate (dashed green line) defines the duration of time-interval II (Δt = 86 ms).

Immediately after light application, at the beginning of time-interval II, the PSC rate increases rapidly, reaches its maximum of 13 Hz after 23 ms and declines slowly to the rate of spontaneous activity 168 ms after stimulus onset, which is maintained to the end of time-interval Ib. Half of the photo-induced PSCs appear within the first 32 ms, 75% of the photo-induced PSCs within the first 51.4 ms after stimulus onset. To obtain good signal-to-noise ratios of the photo-induced PSCs time-interval II is defined as the time window, in which the PSC rate is one standard deviation (σ_r = 1.7 Hz) above the averaged spontaneous PSC rate (dotted green line in figure 3-05E). The resulting duration of time-interval II is Δt = 86 ms.

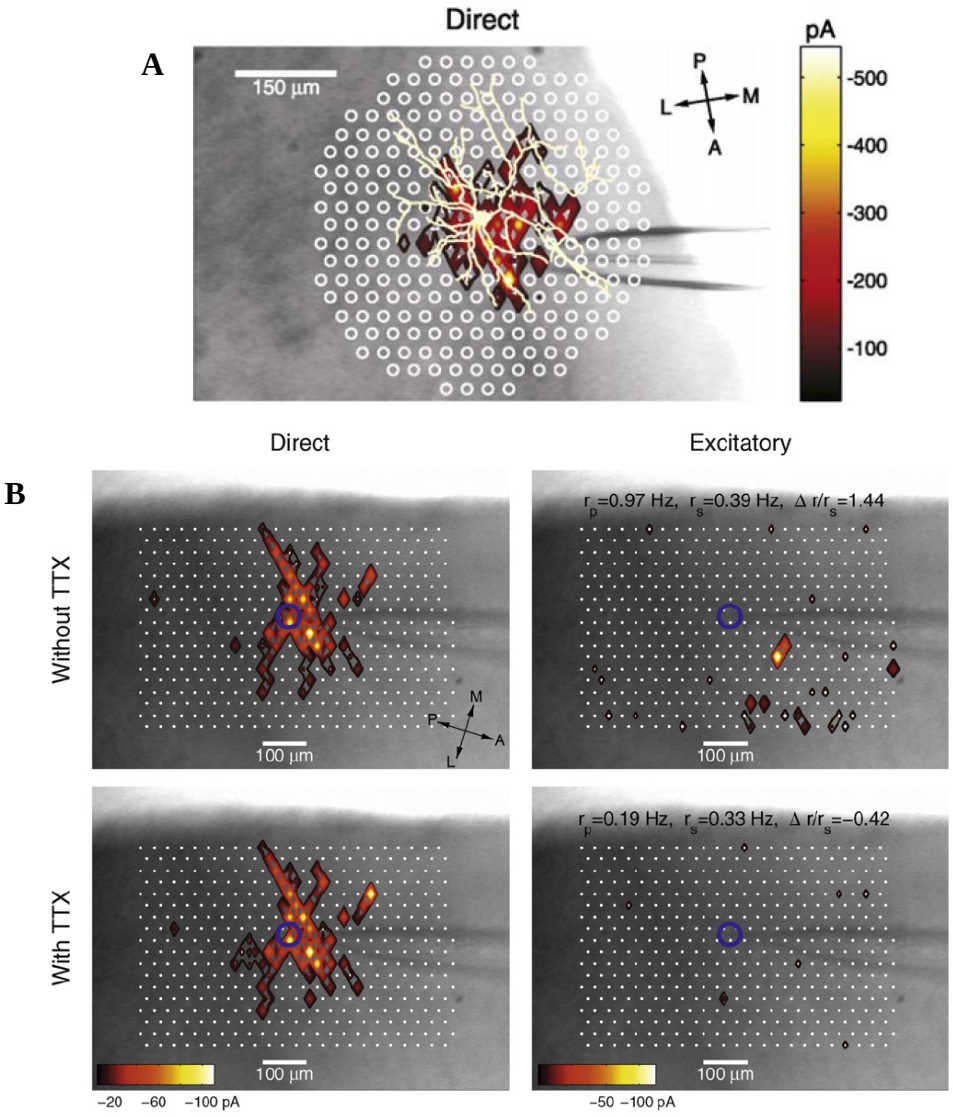

Figure 3-06: Direct responses. **(A)** Direct response profile for a biocytin reconstructed stellate cell (beige). Although regions of high activation are more likely in the perisomatic region, they can be also found in regions that are up to 150µm far from the soma. **(B)** The effect of TTX on the response profiles. Direct responses (left column) and indirect response map of excitatory inputs (right column) of a L2S (soma is indicated by a blue circle) as a function of the stimulation point (white points) without (top row) and with TTX (bottom row). The

point-specific amplitude of activation is coded by color (bright colors correspond to large amplitudes) and size (large size corresponds to large amplitudes). The direct response profile is virtually identical in spatial extent and amplitude for both trials, thus largely unaffected by TTX. Contrary, the indirect response map of excitatory inputs is altered significantly under TTX. Formerly clear excitatory inputs (e.g., from the bottom right quadrant) that are characterized by a non-random spatial arrangement and exhibit relatively large compound amplitudes between −50 pA and −120 pA vanish under TTX. Instead, random, spatially uncorrelated inputs remain with small compound amplitudes (<12 pA) presumably caused by miniature excitatory postsynaptic currents. Accordingly, the photo-induced PSC rate, r^P decreases from 0.97 Hz to 0.19 Hz, while the spontaneous PSC rate, r^S remains approximately constant under TTX (0.39 Hz vs. 0.33 Hz), reducing the quotient $(r^P - r^S)/r^S = \Delta r/r^S$ from 1.44 to −0.42.

3.9d Quantification of point-specific synaptic input

To quantify the point-specific synaptic input, a compound signal is computed by summing the peak amplitudes of the indirect PSCs. Since both photo-induced and spontaneous PSCs show similar biophysical characteristics (peak amplitude, rise and decay time), no clear separation of these unitary events is possible. To numerically correct for spontaneous activity the averaged compound signal of time-intervals Ia and Ib is subtracted from the photo-induced indirect compound signal of time-interval II. The point-specific background correction of the indirect input is justified by the findings that the time courses of the spontaneous activity can change significantly during the stimulation process, but evolves on a slower time scale than the photo-induced PSC rate. Even after 2 s, we observed a significant correlation of 0.11 between the spontaneous rates of subsequent signals ($p < 0.001$). In contrary, a correlation between spontaneous activity and photo-induced activity during a trial could not be observed.

3.9e Input maps

In a first step, the rate and the biophysical properties of the detected photo-induced and spontaneous PSCs was analyzed. The photo-induced PSC rate r^P is significantly higher ($p < 0.001$) for EPSCs ($r^P_{exc} = 6.6 \pm 5$ Hz) than for IPSCs ($r^P_{inh} = 1.9 \pm 1.4$ Hz). Similarly, the spontaneous EPSC rate ($r^S_{exc} = 3.3 \pm 2.5$ Hz) is significantly higher ($p < 0.001$) than the spontaneous IPSC rate ($r^S_{inh} = 0.4 \pm 0.3$ Hz). The average ratios R between photo-induced and spontaneous PSC rate are $R_{exc} = 2.2 \pm 0.8$ and $R_{inh} = 7.2 \pm 5.7$. The inhibitory response ratio is significantly ($p < 0.001$) higher than the excitatory response ratio. We found the following biophysical characteristics of the photoinduced PSCs (mean ± standard error of the mean): EPSCs exhibit a mean peak amplitude of −26.4 ± 0.7 pA (n = 3972), whereas IPSCs show a mean peak amplitude of 22.6 ± 0.5 pA (n = 1097). The mean decay time constant is 6.5 ± 0.08

ms for photo-induced EPSCs and 11.4 ± 0.25 ms for photo-induced IPSCs. Spontaneous PSCs possess subtle, but significant ($p < 0.001$) variations in their biophysical properties: In particular, the mean peak amplitudes are smaller for both spontaneous EPSCs (−19 ± 0.2 pA, n = 8963) and spontaneous IPSCs (13.7 ± 0.2 pA, n = 911). Additionally, the mean decay time constant is larger for spontaneous EPSCs (6.8 ± 0.05 ms) and spontaneous IPSCs (14.6 ± 0.3 ms). Since these characteristics change only slightly for photo-induced and spontaneous PSCs, these differences cannot be used to separate both signals. In a second step the strength of the synaptic input is quantified by the background-subtracted excitatory and inhibitory compound signal, which is computed for each stimulation point. Figure 3-07 shows a typical afferent map for both excitatory (figure 3-07A) and inhibitory (figure 3-07B) compound signals.

L2S receives synaptic input from both, excitatory and inhibitory cells. The excitatory inputs arise intralamninarly from L2 mEC. The excitatory compound signal is larger than the inhibitory compound signal. It ranges up to 220 pA per stimulation point. To quantify the spatial distribution of synaptic input over all trials (N_{exc} =17, N_{inh} = 17), the mean compound density (current per area) is calculated as a function of the distance r of the stimulation site from the soma of the target cell (figure 3-07C-D). Both excitatory and inhibitory mean compound densities decrease for increasing distances.

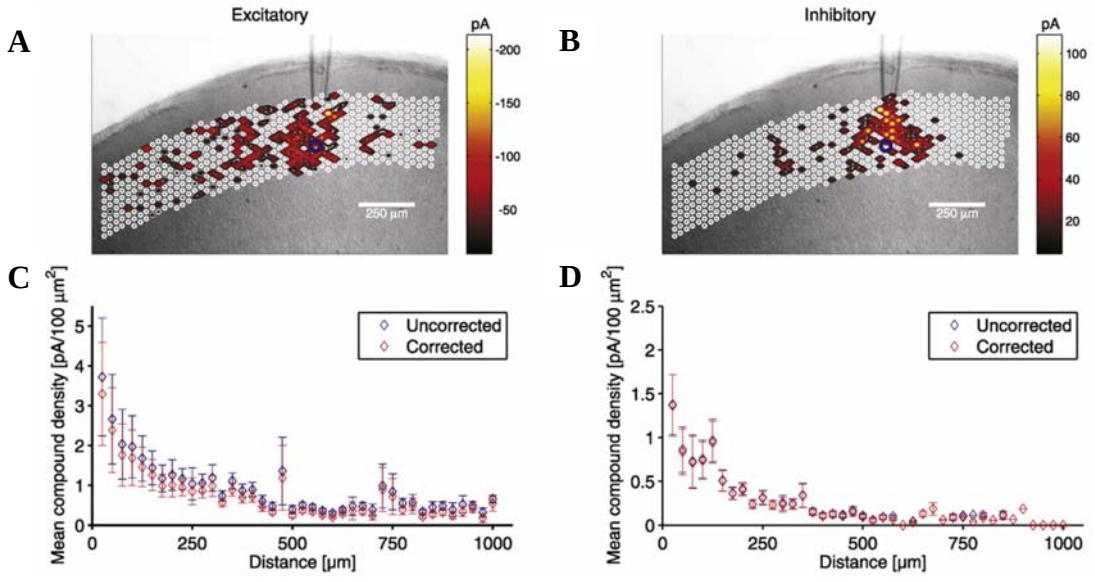

Figure 3-07: Input map of a L2S **(A, B)** Example of an afferent map of a L2S separated into excitatory and inhibitory compound signals, plotted as a function of the stimulation point. L2S receives synaptic input from both, excitatory and inhibitory cells. The excitatory inputs cover the whole extent of L2 mEC. The excitatory

compound signal ranges up to −180 pA, whereas the maximum inhibitory compound signal had a value of 120 pA. To quantify the mean (nexc =17, ninh = 17) spatial distribution of excitatory **(C)** and inhibitory **(D)** synaptic inputs, we plotted the mean compound density for both the uncorrected (blue diamonds) and the background-corrected (red diamonds) maps as function of the distance between stimulation site and the soma of the target cell. Excitatory inputs also arise from more distal locations than the inhibitory ones, which are more localized around the cell soma.

3.10 Inter-trial variability

In a last step, the reproducibility of the direct and synaptic activation profiles were analyzed by measuring their inter-trial variability across identical repeated stimulation patterns (n_{trials} = 4; figure 3-08). We found that the direct activation profile, i.e., its spatial extension and the point-specific peak amplitudes, is virtually identical for all trials (figure 3-08A).

The excitatory compound signal exhibits a higher inter-trial variability (figure 3-08B), which is caused by non-uniform spike transmission process and the high spontaneous background rate during the stimulation process. In particular, the trial-averaged ratio R between photo-induced and spontaneous EPSC rate is only R_{exc} =1.4 ± 0.18 (mean ± standard deviation). In order to quantify the level of similarity among the input maps, we computed both the trial-averaged mean and the coefficient of variation (CV) of the point-specific excitatory compound signal.

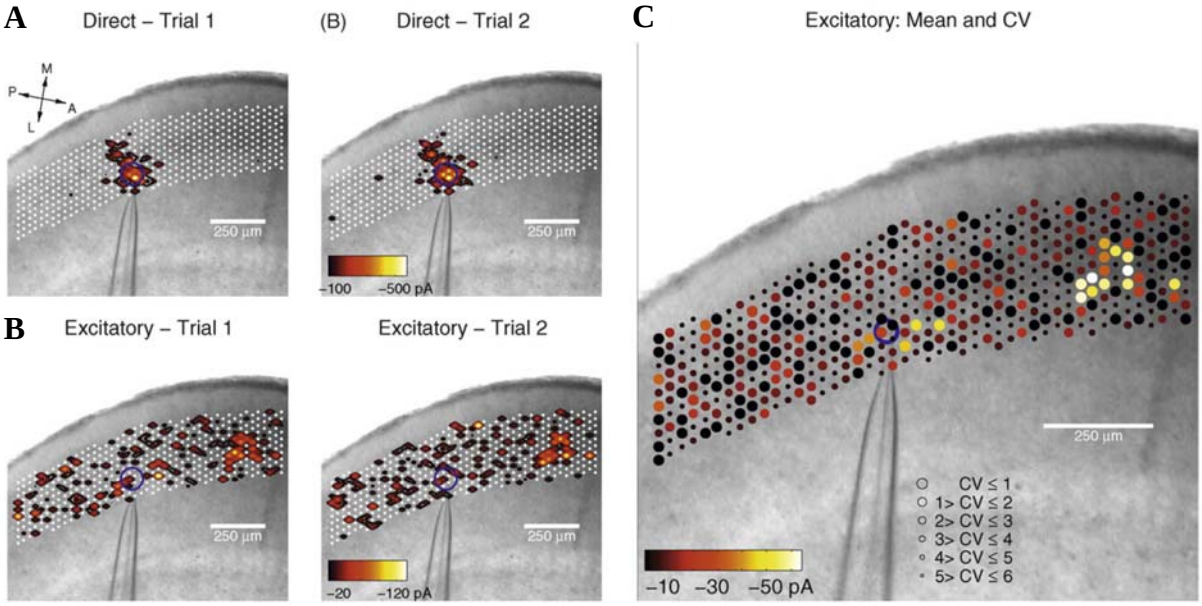

Figure 3-08: Reproducibility of activation. (A) Direct activation of a L2S (soma is indicated by a blue circle) as a function of the stimulation point depicted for two out of four trials of stimulating with identical patterns. The direct activation profile is virtually identical for both trials. (B) Same as in (A) for the excitatory compound

signal which exhibits a higher inter-trial variability. (C) Topographical illustration of both mean and coefficient of variation (CV) of the point-specific excitatory compound signal over all trials (n_{trials} = 4). The magnitude of mean and CV are represented by color and radius of the corresponding stimulation point. Signals that are characterized by a large inter-trial variability (small radius) possess mostly low amplitudes.

Both parameters are illustrated topographically in figure 3-08C, where the magnitude of mean and CV are represented by color and radius of the corresponding stimulation point respectively. Signals that are characterized by a large inter-trial variability possess mostly small compound amplitudes (Pearsons's r = 0.15, $p < 0.001$). Compound signals larger than −30 pA are prevalently of low variability (CV < 2). Thus, strong synaptic connections are reliably detected despite a considerable amount of spontaneous activity.

3.11 Discussion and Outlook

We presented a software solution that enables us to easily plan and conduct photostimulation experiments using large-scale images taken with low-magnification objectives before the onset of the experiment. For each slice, patching of cells and the subsequent photostimulation experiments can then be performed with a higher magnification objective without the need for further objective switches. This was achieved by calibrating the relation between the position of the laser spot in mechanical space and its position in images obtained with objectives of different magnification. The software enables the experimenter to determine the scanning patterns online according to macroscopic anatomical structures like for example brain nuclei, cortical columns or layers. Using this approach, the size of the scanned regions is only limited by the degree of preservation of long-range connections in the brain slice preparation and the stability of the patch recording. The presented software-based system can be used to easily upgrade electrophysiological setups. In comparison to already existing scanning UV-photostimulation setups, the system offers a larger degree of optophysical flexibility and an efficient intuitive workflow without the need for investing into extensive additional hardware equipment. To assess the functionality of the system, the spatial resolution in two-dimensional space was determined for L2Ss and L2Ps. In order to analyze the spatial distribution and the strength of presynaptic excitatory and inhibitory inputs, the functional connectivity of L2S was mapped. In the following subsections, a detailed comparison is drawn out between our technique to those already published and a summary is provided describing the pros and cons of using this method for mapping of neuronal microcircuits.

3.11a One-photon versus two-photon uncaging

Compared to recently developed two-photon based approaches with real single-cell resolution (Nikolenko et al., 2007) combining glutamate uncaging and staining of neuronal cell bodies, a single photon based approach without staining of cell bodies is limited. An inherent property of transmitted light microscopy is a large focal volume in which glutamate is uncaged. This results in a large spatial profile of single cell activation due to the activation of dendritic structures. It is therefore difficult to precisely allocate the source cell in space. Nevertheless, a one-photon based approach is well suited for large-scale mapping of neuronal circuits. At this scale, quantitative information about the connectivity patterns of a single cell with respect to cortical subregions, layers and adjacent regions can still be obtained without real single-cell resolution. In comparison to technically more sophisticated two-photon based solutions, the set-up needed to run the Lucifer software is cost effective, only a few additional standard pieces of equipment (a UV-light source, a shutter, a light guide, an adapter to couple the light guide to the epifluorescence lightpath of the microscope, a PC and a standard I/O-board) need to be bought to equip a standard infrared videomicroscopy DIC patch clamp setup for photostimulation. From this perspective, the Lucifer software offers some unique features when compared to other solutions used for one-photon photostimulation.

3.11b Comparison to other one-photon uncaging setups

There are two different basic concepts of moving a laser beam across a brain slice in one-photon uncaging setups. One is a stationary microscope where the laser beam is scanned across the objective's field of view by galvanometric driven mirrors (mirror-based) and the scanned laser spots are attributed to image coordinates (Shepherd et al., 2003). For large-scale mapping, this laser scanning approach offers sufficient resolution combined with the advantages of low-magnification objectives. The disadvantage of this approach is that once the scan is started, it is impossible to control the focal depth of stimulation precisely. Therefore, a cylindrical light beam is used (Shepherd et al., 2003).

A mirror-driven laser scanning setup requires two rather costly additional devices: A galvanometric-mirror-based scanning system is necessary to move the laser spot across the brain slice. Moreover, the physical properties of low-magnification low numerical aperture air objectives demand the use of a high-power pulsed UV-laser to convey enough laser energy to the brain slice (Kumar et al., 2007; Shepherd et al., 2003). Although the same laser was used in our experiments, we used it at a fraction of its maximal performance and the setup can also be employed with weaker light sources like a UV-Flashlamp.

The second, technically simpler approach to scanning photostimulation is mechanically moving the optical system with a UV-light spot determined by the focal point of the objective and the slice relative to each other using a motorized XYZ-shifting table (shifting table-based) (Schubert et al., 2001). There are two main drawbacks of a shifting table-based compared to a mirror-based system: First, the scanning speed is mechanically limited as a relatively large mass has to be moved on a fine scale while a cell is patched, which is no fundamental disadvantage when using the setup for functional mapping. Second, in previously existing shifting table-based setups, the shifting table moves in defined steps with respect to the patched cell without the possibility to fine-tune the scanning pattern according to cortical subregions on a larger scale. In these previously existing setups using the shifting table-based approach, certain subregions cannot be selectively targeted during planning the experiment but rather standardized point rasters have to be processed, usually resulting in larger scans and therefore longer experiments than needed.

The control software presented here relates the position of the laser spot in mechanical space to its position in planning images. We can combine a low-magnification DIC image for intuitive and fast online planning with high-magnification optics for stimulation. The magnification of the objective used for stimulation is therefore independent of the size of the analyzed brain region. Navigation and planning can be performed with high temporal efficiency on a large scale and while the cell is patched, so that any kind of scanning pattern relative to the cell and different subregions of the brain like layers, nuclei or adjacent brain regions can be easily implemented online.

Another related problem is the change of the distance between the focal depth of the microscope in the Z-axis and the slice surface due to non-uniformities of the surface of a large brain slice. With high NA lenses, the response amplitude is influenced both by the tissue depth and the focal plane (Kötter et al., 2005). The presented system offers the option to online determine adjacent subregions for scanning. Therefore, the depth of the focal plane in relation to the slice surface can be independently determined for different subregions. This increases the precision of uncaging in the Z-plane by keeping the stimulation depth at comparable values. In addition, the ability to capture high-resolution DIC images while scanning which can later be stitched together offer an offline high-resolution overview of the scanned brain region and can be used to identify the stimulated regions in greater detail and to determine the slice quality.

In summary, the presented system advances the concept of shifting table-based scanning photostimulation by adding one of the main advantages of a mirror-based system, the option

to online determine stimulation points on a low-magnification image during the course of the experiment obviating the need for post-hoc determination of the stimulation sites relative to the recorded cell.

3.11c Effective resolution of the system

The direct excitation profile of L2S and L2Ps, the two main excitatory cell types in the L2 mEC (Alonso and Klink, 1993), was calibrated for quantification of the effective resolution of the system. When comparing it to other calibration results in the barrel cortex (Schubert et al., 2001; Shepherd et al., 2003) or the hippocampus (Brivanlou et al., 2004), a d* value of 100 µm is within the published range and sufficient to differentiate inputs from different cortical layers. L2Ps possess a slightly larger spatial activation region than L2Ss. L2Ps which have a pronounced apical dendrite, a significant relationship between the orientation angle of the stimulation site relative to the cell soma and the number of hotspots was not found. Such an orientation selectivity would be required if hotspots on apical dendrites were the reason for the larger activation region of L2Ps.

3.11d Mapping of indirect responses

Direct stimulation can readily be distinguished from indirect stimulation when comparing the onset latencies of excitatory currents. The time window determined for direct activation was experimentally confirmed by comparing the direct activation profile with and without TTX. The time window for detecting indirect responses is based on the averaged photoinduced increase of the rate of PSCs one standard deviation above the averaged spontaneous PSC rate. Indirect responses were considered monosynaptic. During the calibration in current clamp we never observed AP-firing following an indirect response, which would hint at polysynaptic activation.

Using a low-chloride intracellular solution holding the cell voltage-clamped at −60 mV, it is possible to record both EPSCs and IPSCs at the same time (Pouille and Scanziani, 2001). The analysis software detects the PSCs and automatically determines the onset latency, peak amplitude, area under the curve, rise time and decay time constant of the detected signals. The performed mapping experiments exemplify the concept of stimulating a specific cortical subregion (L2 mEC) on a large scale, minimizing the number of stimulation points needed, therefore decreasing the duration of the scan and increasing the data yield per experimental day.

Due to the disruptive nature of reducing a three-dimensional brain to slices (Steriade, 2001), the observed decrease of presynaptic densities with distance from the cell may be an effect of axonal disruption. Carefully selected slice preparations can preserve long range axonal connections (Agmon and Connors, 1991; Alle and Geiger, 2006). In special preparations, it is therefore possible to use functional mapping on a large scale to compare the connectivity of different cell populations quantitatively and in relation to anatomically defined structures (Bureau et al., 2006). However, the main use of functional mapping is the characterization of the synaptic microcircuit on the scale of a few hundred µms. Examples are single cortical columns and/or layers in the barrel cortex (Schubert et al., 2001; Shepherd et al., 2003), the visual cortex of rats (Dantzker and Callaway, 2000) and macaques (Briggs and Callaway, 2005) and neighboring CA3 and CA1 cells in the hippocampus (Brivanlou et al., 2004). Another important aspect is the change of maps after functional modifications (Shepherd et al., 2003) or in disease models (Bureau et al., 2008). When plotting the compound EPSC and IPSC size against the distance from the cell body, both the presented system and the galvanometric-mirror driven scanning system used by Kumar et al. yielded comparable results (Kumar et al., 2007). The smaller compound EPSC and IPSC size routinely observed in our experiments most likely stem from differences in the holding potential (−60 mV in our experiments vs. −70 mV for EPSCs and −60 mv vs. 0 mV for IPSCs) and different ionic compositions of the extracellular and intracellular solutions used for recording.

In addition to the presented functional mapping of synaptic inputs on a large scale with a high resolution using caged glutamate, the presented uncaging system can also be easily adapted for different applications. Due to mechanical limitations of the moveable microscope stage, speed is a definite constraint of this setup. It is not suitable for fast uncaging at multiple sites (Shoham et al., 2005). For this approach, a fast galvanometric-mirror driven spot illumination system is needed. However, such a system could be combined with a Lucifer-based mechanical microscope stage to combine high-speed and the ability to scan large areas. By changing the diameter of the optical fiber, laser spot sizes as small as 2 µm can be used in combination with the definition of optical reference points for fine scale mapping of dendritic inputs visualized by staining the neuron with a fluorescent dye in the intracellular solution. In addition, the setup can be used to identify presynaptic partners of a postsynaptic patched cell to facilitate paired recordings.

CHAPTER 4:

CELL-TYPE SPECIFIC AND MODULAR ORGANIZATION OF MICROCIRCUITRY IN THE MEDIAL ENTORHINAL CORTEX

The medial entorhinal cortex (mEC) is considered as an interface for bidirectional processing of parallel streams of information, thereby functioning as a nodal input-output device (Canto et al., 2008). Recent evidence points to a more independent computational role of the mEC: place-specific firing fields are organized in hexagonal grids. Therefore, the mEC provides a two-dimensional metric representation of external space that is necessary for spatial navigation and independent of external cues (Fyhn et al., 2004; Hafting et al., 2005; Moser and Moser, 2008). Grid cells are present in all layers of the mEC. Cells in the deeper layers additionally exhibit head-direction–specific responses. In contrast, layer II (L2) mEC cells predominantly show pure grid-field responses (Sargolini et al., 2006). In spite of the functional homogeneity described, L2 mEC contains two biophysically and morphologically distinct projection neurons: the stellate (L2S) and the pyramidal (L2P) cells (Alonso and Klink, 1993).

Further, anatomical studies have distinguished two different patterns of associative connectivity in the mEC: intralaminar recurrent connections (Koehler, 1986) and ascending

interlaminar feedback connections (Iijima et al., 1996; Koehler, 1986). The ascending interlaminar feedback connections from deep layers to superficial layers play an important role in updating the grid cell network through the integration of position, direction and speed signals (Sargolini et al., 2006). It is however, unclear how these integrative units defined by the microcircuitry are organized. One option would be local circuit modules, comparable to columns in the neocortex (Mountcastle, 1997). Alternatively, circuit connections could be scattered across the mEC, comparable to the organization of neighboring paleocortical structures such as the piriform cortex (Johnson et al., 2000). Although the formation of modules has been postulated to reflect different grid spacing along a dorsal to ventral axis (Hafting et al., 2005), to date there is no direct functional evidence for modular connectivity (Witter and Moser, 2006).

Thus the hypothesis is that the integrative function of mEC as a spatial navigation unit should therefore be reflected in the intrinsic microcircuitry. Using a scanning photostimulation method with caged glutamate (Bendels*, Beed* et al., 2008), we investigated the microcircuitry of the L2Ps and L2Ss in the L2 mEC. In this study, we provide the first direct functional evidence that projection neurons in the L2 mEC have a cell-type–specific and modular organization suggestive of columns.

4.1 Calibration of spatial profiles of excitatory cells

Focal photolysis of caged glutamate induces two types of activity in the recorded neuron, direct and indirect synaptic responses. The direct responses were evoked when glutamate was uncaged directly on the cell soma or the dendrites of the recorded cell. Indirect synaptic responses reflect suprathreshold activation that results in action potential (AP) firing of a presynaptic cell projecting onto the recorded cell (figures 4-01 and 4-02).

The first step was to determine the laser intensity that permits maximal spatial resolution when mapping indirect synaptic inputs. A measure of spatial resolution for scanning photostimulation is the critical distance d*, which is defined as the distance from the cell soma where 75% of all cumulated action potentials (APs) could be evoked as direct responses. The d* value depends on cell type and laser intensity. It enables extrapolation of the distance between presynaptic cell soma and the hotspot, *i.e.*, the location of the photostimulated synapses that induce an AP in the presynaptic cell (Bendels*, Beed* et al., 2008). In figure 4-01A, the mEC is displayed in the DIC image. The white circle (radius of 150 μm) indicates the area for mapping AP profiles. Spatial profiles of AP firing of the main

excitatory cells in all layers of the mEC were generated in the current clamp mode. The direct responses elicited at each stimulus site were plotted in figure 4-01B-E. The stimulation pattern consisted of points with 30 µm spacing. For each cell type, d* was calculated at different laser intensities.

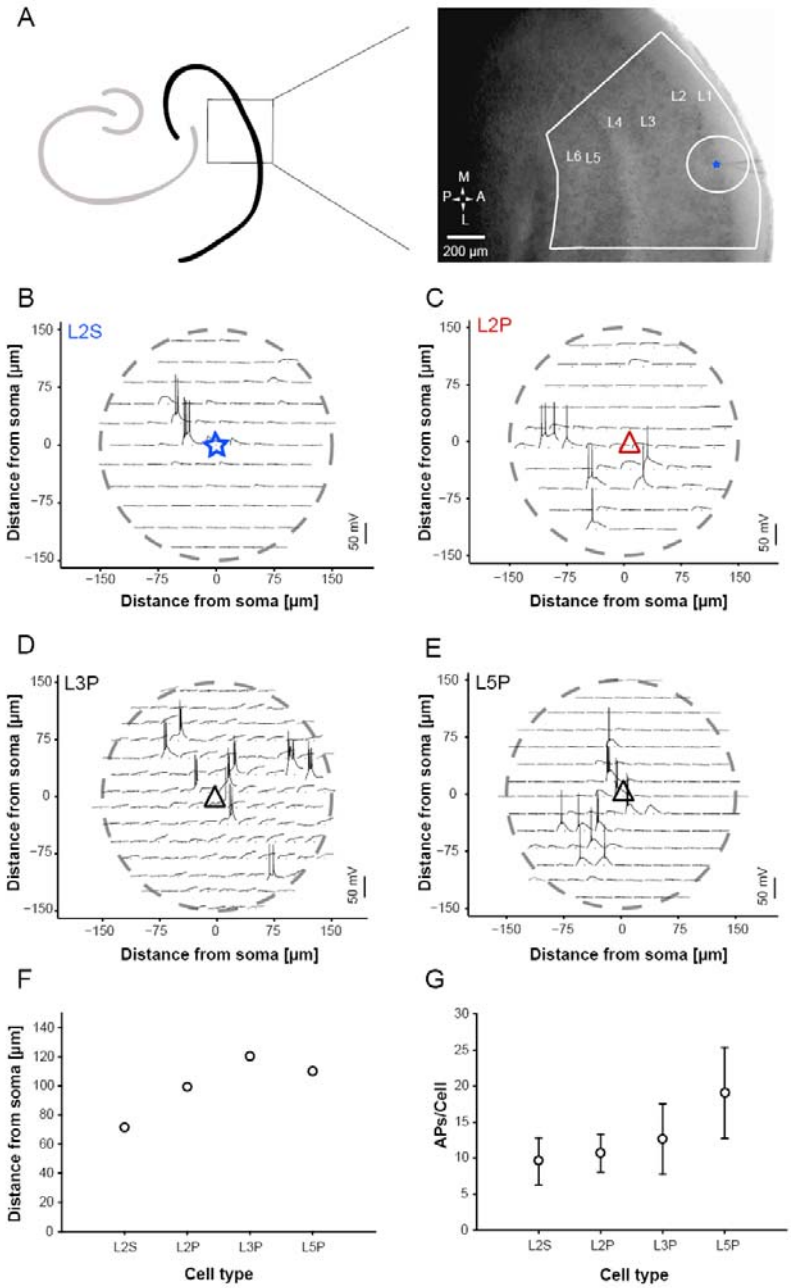

Figure 4-01: Resolution of photoactivation by glutamate uncaging **(A)** Horizontal acute brain slices containing the hippocampal formation were used for the mapping experiments. The medial entorhinal cortex (mEC) is highlighted in the DIC image. The white circle (radius of 150 µm) indicates the area for mapping action potential (AP) profiles and the white polygon indicates the area for mapping synaptic connections. **(B-E)** Spatial profiles of excitability of the main excitatory neurons were performed. The voltage changes elicited at each stimulus site were plotted. The stimulation pattern consisted of points with 30 µm spacing, and the area mapped is indicated

by the white circle in A. **(B)** Layer 2 stellate cell (L2S), **(C)** layer 2 pyramidal cell (L2P), **(D)** layer 3 pyramidal cell (L3P), **(E)** layer 5/6 pyramidal cell (L5P). Cell somas are depicted by symbols: L2S – blue star, L2P – red triangle, L3P and L5P – black triangle. **(F)** Analysis of excitation profiles: spatial resolution of photostimulation as indicated by critical distance (d*) from the soma that defines the radius within which 75% of the cumulated APs were elicited, indicated for each of the four cell types (L2S, n=17; L2P, n=12, L3P n= 18; L5P, n=25). **(G)** Analysis of excitation profiles: excitability in response to photostimulation as indicated by the average number of APs, shown for each cell type.

The following cell-type–specific d* values were recorded at the laser intensity used for our experiments: L2 stellate cell (L2S, n = 17), 71.5 µm; L2 pyramidal cell (L2P, n = 12) 99.2 µm; L3 pyramidal cell (L3P, n = 18), 120.3 µm; and L5/6 pyramidal cell (L5P, n = 25) 110.0 µm (figure 4-01F). The average number of APs per cell was calculated for each cell type as a measure of photostimulation-induced excitability. In figure 4-01G, the average number of APs/cell is plotted as a function of the cell type (L2S: 9.5 ± 3.2, L2P: 10.7 ± 2.6, L3P: 12.6 ± 4.9 and L5P: 19.0 ± 6.3).

4.2 Mapping excitatory L2 projection neurons

To determine the functional microcircuitry, mapping of synaptic inputs was performed for the two main projection neurons in L2 mEC, the L2S (stellate) and the L2P (pyramidal) cells (Alonso and Klink, 1993). For the mapping experiments, a hexagonal grid was projected across the different layers in the entorhinal cortex. Figure 4-02A depicts the mapping area. The scanning region (L1 – L6) was grouped into the following cortical layers: L1-2 (green), L3-4 (black), and L5-6 (purple; figure 4-02A). Layers 1 to 3 constitute the superficial layers, layers 5 and 6 the deep layers.

The two neuronal types were identified using their characteristic morphological and electrophysiological properties. The mapped cells could be unambiguously categorized based on their well-established biophysical markers (larger hyperpolarizing and depolarizing sag current and early firing upon depolarization for L2Ss, small hyperpolarizing and depolarizing sag current and slow ramp current with long-latency AP firing upon depolarization for L2Ps. (figure 4-02B and C left and middle; Alonso and Klink, 1993).

Uncaging of glutamate evoked both direct and indirect synaptic responses. These were clearly separated by their different delay-to-onset times. Direct responses were elicited almost immediately (in a time window of 10 ms), whereas synaptic inputs were collected up to 95 ms following UV photolysis (figure 4-02B and C, right; see Bendels*, Beed* et al., 2008 for

details). In order to discriminate between specific synaptic inputs and background activity, we used a spatial-correlation–based algorithm described elsewhere (Bendels et al. 2009, in revision). In brief, specific photoactivation-induced inputs were distinguished from randomly occurring background noise based on correlations in spatially oversampled recordings. This procedure is validated by the observation that photostimulation results in the spatial clustering of hotspots in presynaptic cells (figure 4-01B-E).

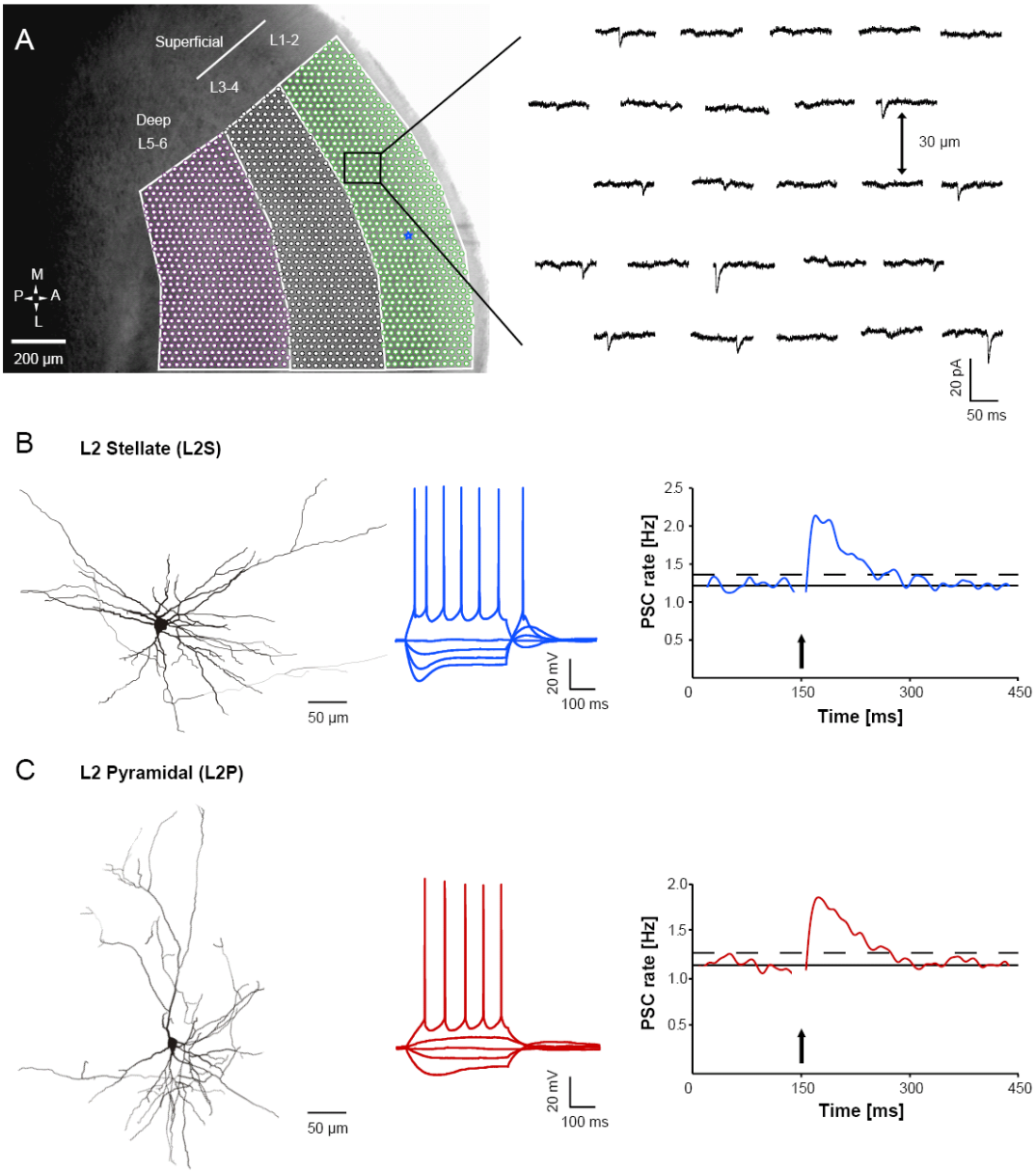

Figure 4-02: Mapping excitatory L2 projection neurons (A) Scanning raster (left) superimposed on the DIC image of the entorhinal cortex. The cortical region was grouped into the following layers: L1-2 (green), L3-4 (black) and L5-6 (purple). The raster consisted of stimulation points separated by 30 µm, and the trials were randomized to avoid any bias arising from scanning these cortical layers in a fixed order. Traces from the 5x5

raster highlighted in A are displayed on the right. The first 100 ms after the UV-flash are plotted at each stimulation point. (B-C) Biocytin reconstructions (left panels) of representative L2S and L2P, and corresponding electrophysiological properties (middle panels) of these two main projection neurons in the L2 mEC are shown. Average postsynaptic current (psc) incidence rates are indicated (right panels). Arrows indicate the time-points of the UV-flash.

4.3 Synaptic inputs onto stellate and pyramidal cells

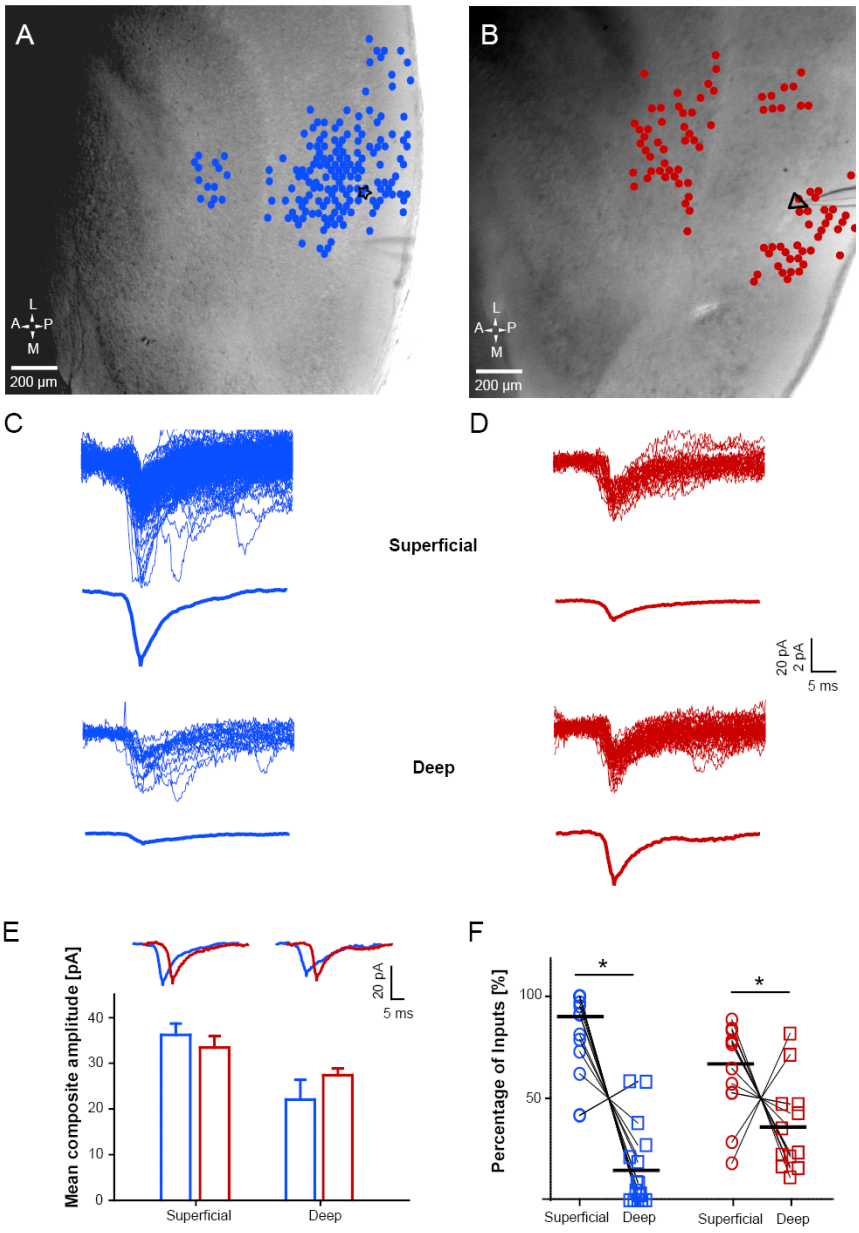

Figure 4-03: Cell-type–specific microcircuitry for L2 mEC projection neurons **(A)** Blue dots highlight the uncaging spots which were detected as synaptic points projecting to the L2S (black star) from a single representative map. Most of the inputs of this L2S arise from intralaminar recurrent connections. **(B)** Red dots

highlight all uncaging spots which were detected as synaptic points projecting to the L2P (black triangle) from a single representative map. The L2P receives less superficial intralaminar recurrent connections, but receives stronger ascending interlaminar feedback connections from the deep layers of the mEC. **(C, D)** Indirect synaptic responses underlying the synaptic points in the L2S in A **(C)** and L2P in B **(D)** were aligned to the minimum. The overlays correspond to superficial (top) and deep (bottom) layers. The corresponding average traces are scaled to the total number of scanned points (including all uncaging points which were no synaptic points) in each layer to document differences in input strength. **(E)** Mean composite synaptic amplitude as the sum of synaptic current amplitudes divided by the number of points from which a synaptic response was detected, calculated for each cell in the different layers. L2S: blue columns; L2P: red columns. Within layers, the differences are not statistically significant ($p > 0.05$). Traces in the inset are unscaled averages of the synaptic inputs depicted in the overlays in C and D. **(F)** Quantification of input source location for both L2S and L2P. The percentage of synaptic points in the different layers as a fraction of the total number of synaptic points is calculated for each cell. Circles indicate the percentage of inputs coming from the superficial layers for each cell analyzed; squares indicate that from the deep layers. L2S – blue, L2P - red. For both cell types, the percentage of superficial layer input was significantly higher than deep layer inputs ($p < 0.05$). When comparing across cell types, L2Ss receive a significantly higher proportion of inputs from the superficial layers ($p < 0.05$), whereas L2Ps receive a significantly higher proportion of inputs from the deep layers ($p < 0.05$).

L2Ss (n = 15) receive a larger proportion of inputs from the superficial layers, whereas L2Ps (n = 12) receive the majority of inputs from the deep layers (figure 4-03). Representative maps of only presynaptic input locations (synaptic points) that have significant spatial correlations (Bendels et al., 2009 in revision) are shown in figures 4-03A and B for the two cell types.

First, we calculated the mean composite synaptic amplitude, the sum of photoinduced synaptic current amplitudes divided by the number of points from which a synaptic response was detected, for each cell in the different layers. Comparing the mean composite synaptic amplitude of L2Ps and L2Ss within the superficial and deep layers, we could not detect a significant difference (figure 4-03E: superficial: 36.18 ± 2.5 pA for L2Ss vs. 33.46 ± 2.5 pA for L2Ps, $p > 0.05$; deep: 22.06 ± 4.35 pA for L2Ss vs. 27.38 ± 1.47 pA for L2Ps, $p > 0.05$).

As shown in figures 4-03A-D, the number of synaptic points from superficial and deep layers differs between the L2S and the L2P. The next step was to quantify the numbers of positive synaptic points. We calculated the percentage of synaptic points in the different layers as a fraction of the total number of synaptic points for each cell. Amongst the L2S population, 83.55 ± 5.30% of all inputs arise from the superficial layers while only 16.45 ± 5.30% arise from the deep layers. In comparison, L2Ps receive a higher proportion of inputs from the deep layers constituting 36.42 ± 6.51% of all inputs; the rest of the inputs, 63.58 ± 6.51%, were

from the superficial layers. Comparing deep and superficial inputs within cell types, both L2Ss and L2Ps receive significantly more input from the superficial lamina than from the deep lamina (stellate superficial vs deep: $p < 0.05$; pyramidal superficial vs deep: $p < 0.05$; figure 4-03F). However, 7 out of 15 (46.67%) received less than 5% of their total synaptic input from the deep layers, whereas every (all 12) L2P received more than 10% of their inputs from the deep layers.

4.4 Modular organization of deep layer inputs

Analysis of the spatial pattern of the deep layer inputs revealed a coherently clustered organization around the vertical axis (perpendicular to the pial surface) through the soma of the recorded cell (figures 4-04A-B). This clustering of the deep layer inputs suggests a modular organization of the ascending interlaminar feedback connections in the mEC, with a half maximal width of 106.64 µm for L2Ss and 188.71 µm for L2Ps (figures 4-04A-B).

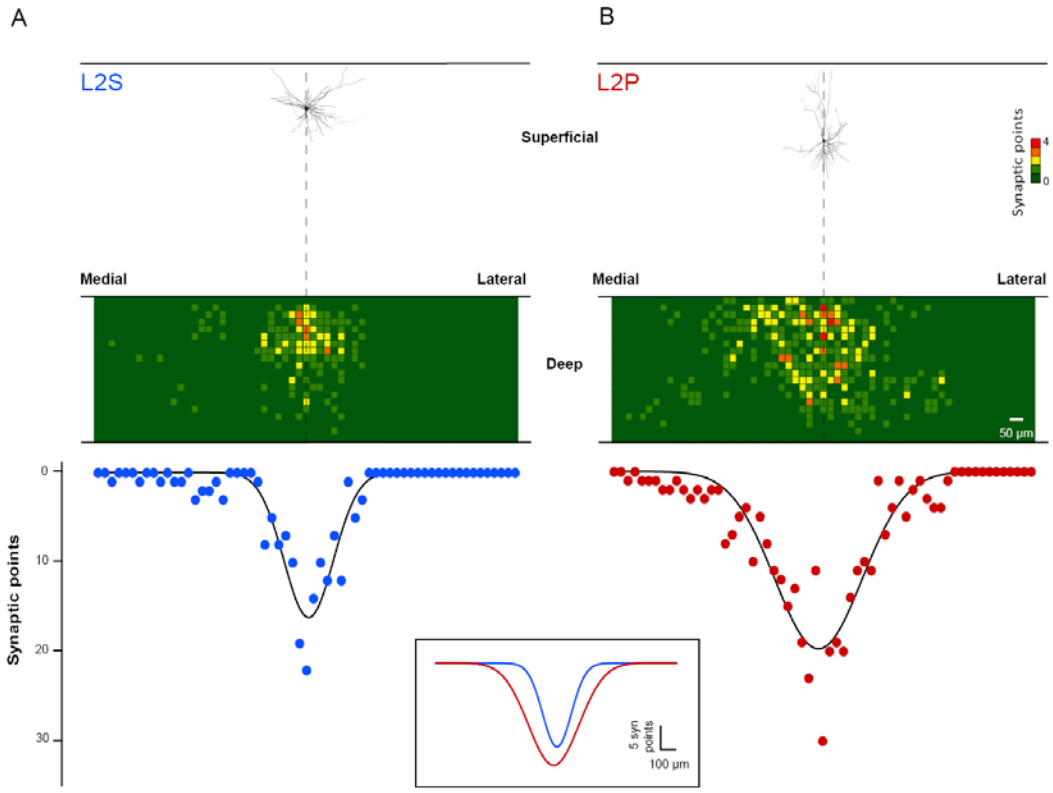

Figure 4-04: Modular organization of deep layer inputs (A-B) Overlay of synaptic input points from the deep layers to L2 projection neurons (L2S in A; L2P in B). A coherently clustered modular organization of inputs is revealed around the vertical axis (perpendicular to the pial surface) through the soma of the cells. Bottom: half maximal width of the distribution of synaptic inputs was for L2Ss: 106.64 µm and for L2Ps: 188.71 µm.

This clustering was observed for both projection neurons. However, the lateral extent of the deep layer inputs was different for the two cell types: L2Ss received 80% of their deep layer inputs within a lateral distance of 350 µm whereas the L2Ps received the same fraction of inputs from a significantly wider lateral distance of 598 µm (figure 4-05A; $p < 0.05$ by Kolmogorov-Smirnov test).

Thus, the deep layer inputs onto the L2Ss are spatially restricted in comparison to those onto the L2Ps. In addition, the difference between the average number of inputs (data pooled from all experiments and cumulated over distance) between the two cell types increased on moving farther away from the vertical axis (figure 4-05B) confirming that L2Ps have a wider lateral extent of the interlaminar feedback connections as compared to L2Ss.

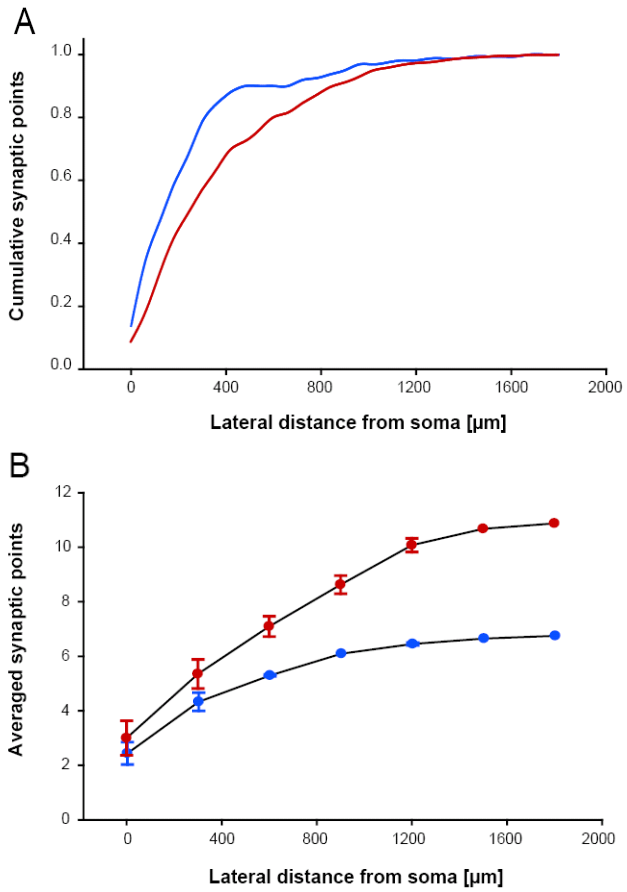

Figure 4-05: The lateral extent of the deep layer inputs is wider for L2Ps as compare to L2S **(A)** Cumulative plot of the deep layer synaptic inputs for the L2S and L2P shows that the lateral extent of the ascending interlaminar inputs is wider for L2P in comparison to L2S. 80% of the synaptic inputs for L2S and L2P are reached at 350 µm and 598 µm respectively ($p < 0.05$, Kolmogorov – Smirnov test). **(B)** The average number of synaptic inputs from all maps for each cell type is cumulated over distance. L2Ps receive significantly higher number of synaptic inputs wider away from the vertical axis through the cell soma even at distances where the L2Ss receive no further inputs.

4.5 Discussion and Outlook

Layer II of the medial entorhinal cortex (L2 mEC) has recently received considerable attention due to its unique grid-like firing fields, which provide a metric representation of external space. Functional work at the systems and behavioral level has been connected with cellular electrophysiology (Giocomo et al., 2007) and wiring diagrams based on classical

anatomical tracer studies (Witter and Moser, 2006). We present new insights into mEC microcircuitry based on an approach that is fundamentally different from anatomical studies in which connectivity is assessed based on the overlap of dendrites and axons. Scanning photostimulation permits for functional characterization of microcircuits based on the number of target-cell–specific functional contacts (Callaway and Katz, 1993; Dalva and Katz, 1994). Although scanning photostimulation with caged glutamate has its limitations for long-range connections, it can be used effectively for investigating short-range connections like columns in the barrel cortex (Schubert et al., 2003; Shepherd et al., 2003). Local circuitry is sufficiently preserved in acute brain slices (Steriade, 2001); we were therefore able to use this method to distinguish the circuitry of individual postsynaptic cell types in a cortical layer.

Based on anatomical studies, associative connectivity in L2 mEC can be divided into two different pathways, the intralaminar recurrent connections and ascending interlaminar feedback connections (Kohler, 1986). Using extracellular recordings and current source density analysis *in vivo*, ascending interlaminar feedback connections have been demonstrated primarily for deep layers to the superficial L3 (Kloosterman et al., 2003). Intralaminar recurrent connections have been demonstrated using paired recordings in L3 and L5 (Dhillon and Jones, 2000). In the same study, connected pairs of L2 cells could not be found, and interlaminar connectivity between the deep and superficial layers was not assessed. When using scanning photostimulation in another study, intralaminar recurrent connections could be demonstrated in L2 (Kumar et al., 2007). L2 projection neurons, the L2Ss and L2Ps, are clearly distinct from neurons in L3 mEC: they have different biophysical properties and project to CA3 and the dentate gyrus, whereas L3 cells project to CA1 and the subiculum (Alonso and Klink, 1993; Dickson et al., 1997; Gloveli et al., 1997; Klink and Alonso, 1997; Witter and Amaral, 2004). Consequently, our target population of L2 cells constitutes a defined and isolated functional unit. We discern between superficial (L1 – L3) and deep (L5 and L6) layers to assess the differences between intralaminar recurrent and interlaminar feedback connections. This division is supported by the different patterns of hippocampal and neocortical connectivity: the superficial layers relay cortical inputs to the hippocampus, whereas the deep layers receive hippocampal inputs and project back to the cortex (Canto et al., 2008).

We show that the two morphologically and biophysically different excitatory cell types in L2 mEC, L2Ss and L2Ps, (Alonso and Klink, 1993), are differentially embedded in the associative microcircuitry. L2Ss are mainly incorporated in intralaminar recurrent connections in superficial layers. Pyramidal cells receive proportionally less intralaminar recurrent input.

Instead, they receive more ascending interlaminar feedback connections from the deep layers of the mEC with a wider lateral extent as compared to L2Ss (figure 4-06 shows a cartoon summarizing the key findings of the L2S and L2P microcircuitry). Anatomical observations hint at a modular organization of the mEC in columns, with a columnar diameter of around 500 μm. Interestingly, the lateral diameter we observed for the functional spatial modules in mEC adds support to that reported in literature thus far (Witter and Moser, 2006).

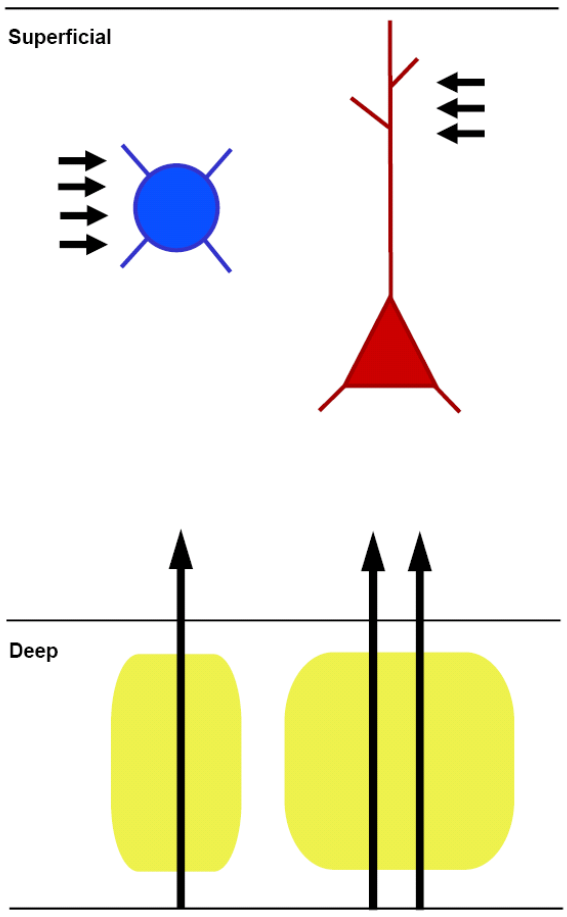

Figure 4-06: Summary cartoon illustrating the cell-type–specific and modular organization of inputs for the two types of projection neurons in the L2 mEC investigated.

The modular organization has been proposed to be important for mEC function. The path integration mechanisms underlying the metric representation of external space by grid cells require the mEC to function as an integrative unit (Sargolini et al., 2006). Theoretical models postulate intralaminar recurrent connectivity, interlaminar connectivity and modular organization of interlaminar connectivity (McNaughton et al., 2006; Witter and Moser, 2006).

In this study, all of these structural assumptions could be functionally confirmed for L2 projection neurons.

To assess the functional impact of the cell-type–specific differences in mEC wiring, it is important to note that grid cells have only been measured with extracellular unit recordings and have not been characterized morphologically. Considering the relative contributions of stellate (70%) and pyramidal (30%) cells (Alonso and Klink, 1993), and the fact that the majority of L2 projection neurons recorded this way display properties of grid cells (Sargolini et al., 2006), it is likely that both cell types constitute the grid cells.

Based on the different organization of inputs received by L2Ss and L2Ps in the mEC microcircuit, we propose that the two main projection neurons in L2 of the mEC have distinct integrative functions. This challenges the canonical view of a uniform grid function of L2 projection neurons in the mEC. The distinct distribution of intralaminar recurrent and ascending interlaminar feedback connections between the two cell types could represent parallel channels of information processing. A microcircuit has been defined as the ‘minimal number of interacting neurons that can collectively produce a functional output’ (Grillner et al., 2005; Silberberg et al., 2005). We postulate that the integration of position, direction, and speed in grid cells mediated by ascending interlaminar feedback projections is organized in spatially distinct modules suggestive of columns. Differences in lateral spread of the synaptic inputs are likely to result in differences in grid cell function between the two cell types. This establishes an important missing link between existing top-down knowledge (systems and behavioral level) and bottom-up knowledge (cellular physiology). In the future, these differences in wiring may be defined more precisely through in vivo study of the functional differences between the two cell types during behavior.

CHAPTER 5:

NEURONAL SYNCHRONY AND EXCITABILITY MICROCIRCUITS TO RECEPTORS

There exist different levels of neuronal organization in the brain, starting from single neurons through small microcircuits and eventually forming functional networks. Neuronal networks are important for processing various convergent inputs to produce a physiologically meaningful output. Neuronal excitability, connectivity and the resulting synchrony is therefore critical in the overall functioning of the different cortical regions.

Neuronal networks are finely balanced in the amount of excitation and inhibition each neuron receives. When such a balance is disturbed due to developmental or environmental insults, the whole network falls out of synchrony resulting in a pathological outcome. One such case is hyperexcitability of neuronal networks, which could, over a longer time scale, develop into epileptic seizures. Many cortical regions have been reported to be potential targets of epileptic insults including the hippocampus, entorhinal cortex and the piriform cortex amongst others.

Several local microcircuits build up the functional neuronal network in the entorhinal cortex. Of these, particularly interesting in regulating the synchrony and excitability in the entorhinal cortex is that formed by L3 pyramidal cells (L3P) in the medial entorhinal cortex (mEC). It is characterized by an extensive recurrent connectivity which is responsible for locally

processing the various cortical inputs and thereon projecting to the area CA1 in the hippocampus and the subiculum. Further, since kainate in different concentrations can either synchronize neuronal microcircuits to generate gamma oscillations (nanomolar; Cunningham et al., 2003) or induce epilepsy (millimolar; Tolner et al., 2005; for review see Vincent and Mulle 2009), it is of interest to investigate the role of kainate receptors (KARs, to which kainate is the ligand) on L3Ps in mediating neuronal synchrony and excitability in the mEC. In the following, we report first about the contribution of KARs in mediating neuronal synchrony at the network level in the mEC and subsequently characterize its role in neuronal excitability at the single cell level. This approach helps in understanding the underlying synaptic transmission mediating neuronal synchrony and excitability at two different levels of neuronal organization.

5.1 Role of KARs in neuronal synchrony and excitability

The neurotransmitter (S)-glutamate (L-glutamate) activates three subtypes of ligand-gated ion channel: the N-methyl-D-aspartate (NMDA), (S)-2-amino-3-(3-hydroxy-5-methyl-4-isoxazolyl)propionic acid (AMPA) and kainate receptors (Lodge, 2009; Watkins and Evans, 1981; Watkins and Jane, 2006). Molecular cloning has identified 5 subtypes: GluK1, GluK2, GluK3, GluK4 and GluK5 which co-assemble in various combinations to form functional receptors (figure 5-01A; according to the new IUPHAR nomenclature; Collingridge et al., 2009; Jane et al., 2009). These new subunit names mirror the corresponding gene names: GRIK1, GRIK2, GRIK3, GRIK4 and GRIK5. The existence of splice variants and editing sites on the KAR subunits increases the likelihood of pharmacological heterogeneity in the KAR family (Hollmann and Heinemann, 1994; Pinheiro and Mulle, 2006).

Kainate receptors (KARs) have a wide functional spectrum, ranging from the presynaptic regulation of transmitter release to the postsynaptic generation of excitatory inward currents (Borlotto et al., 2005; Lerma, 2006; Pinheiro et al., 2006). Furthermore, there is evidence indicating that they are also involved in brain rhythmogenesis (Cunningham et al., 2003; Cunningham et al., 2006; Dickson et al., 2000; Fisahn, 2005; Huxter et al., 2007). In contrast to AMPARs, which have been studied extensively, the roles and physiological importance of KARs are less well understood, although they were originally cloned and described over a decade ago (Lomeli et al., 1992; Tolle et al., 1993; Werner et al., 1991; Wisden et al., 1993) and for reviews see (Huettner, 2003; Lerma, 2006; Pinheiro et al., 2006). One reason for this lack in our understanding of KAR function is the limited availability of pharmacological

agents that enable KARs and AMPARs to be functionally distinguished. The generation of different KAR specific knock-out (KO) mice partially helped to overcome this drawback (Mulle et al., 1998; Mulle et al., 2000) and their characterization yielded insights into KAR physiology. The recent development of the AMPAR selective antagonists GYKI 52466 and GYKI 53655 has also considerably advanced research in the KAR field.

5.2 *KARs in the entorhinal cortex*

There is a mosaic like distribution of KARs in the mEC both in terms of the subunit composition and layer-wise localization (figure 5-01B - GluK2 subunit; Adapted from the Allen Atlas, Allen Institute of Brain Science). Recent works have focused on functional relevance of KARs depending on the neuronal localization. Since L3Ps are involved in kainate induced oscialltions and vulnerable to kainate model of temporal lobe epilepsy, it is of interest to study the KAR mediated synaptic transmission of L3Ps.

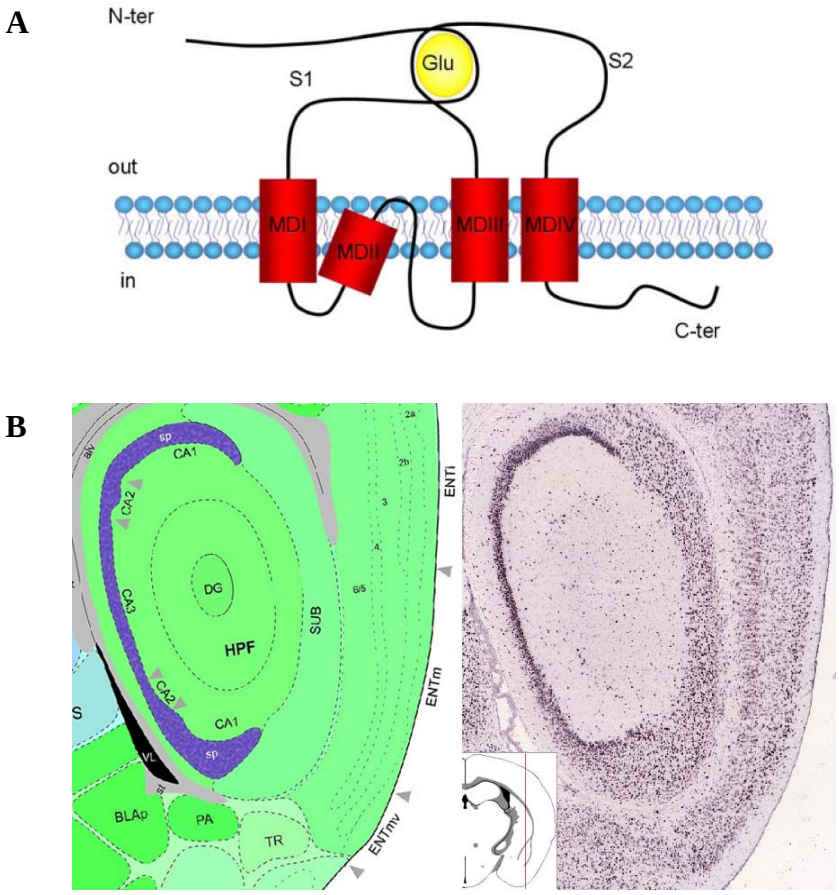

Figure 5-01: Kainate receptors (KARs) **(A)** The subunit topology of KARs is conserved with AMPA and NMDA receptor subunits (ter - terminal; Adapted from Pinheiro and Mulle, 2006). **(B)** *In situ* hybridization of GluK2 subunit of kainate receptor in the mEC (Adapted from the Allen Atlas, Allen Institute of Brain Science).

5.3 *GluK2 containing KARs in neuronal synchrony*

Oscillations in the gamma frequency are recordable from the entorhinal cortex in humans and rodents. It was recently shown that the medial entorhinal cortex (mEC) in isolation in vitro generates gamma frequency oscillations in response to kainate receptor agonists (Cunningham et al., 2003). Importantly, these kainate-induced oscillations in vitro had the same horizontal and laminar spatiotemporal distribution as seen *in vivo*.

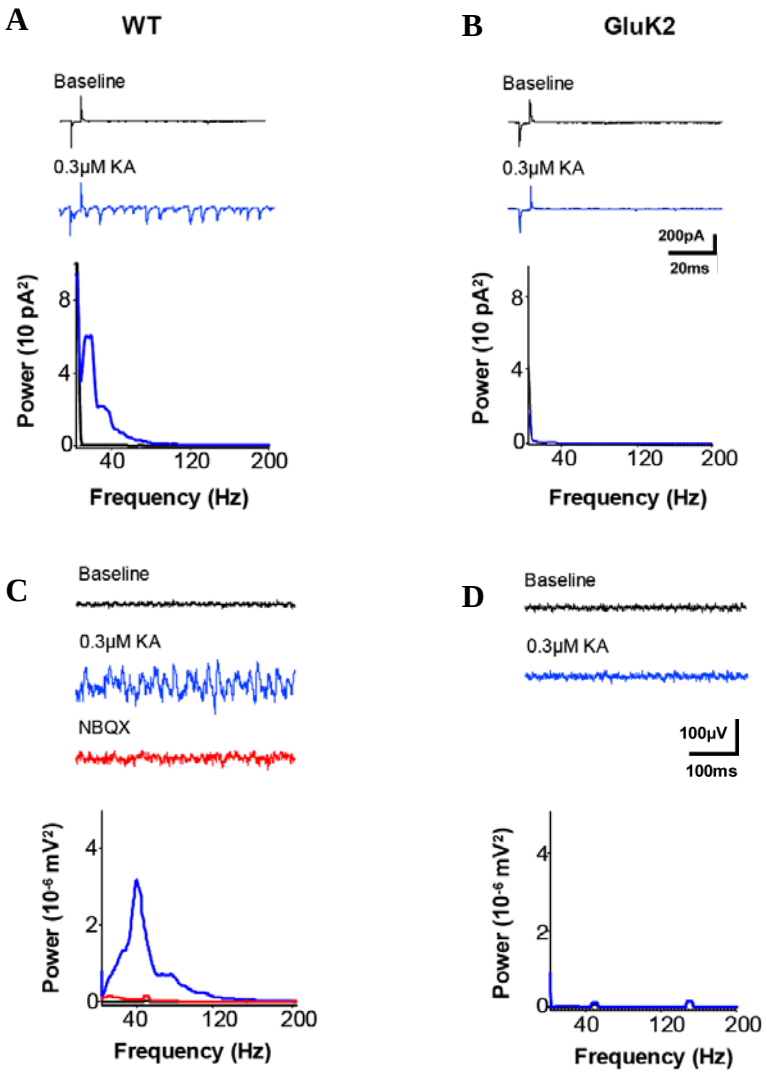

Figure 5-02: Role of GluK2 in network synchrony. **(A)** Rhythmic postsynaptic currents were recorded from WT mice (n = 7) following the application of 300 nM KA which had a frequency content of about 10-12 Hz. **(B)** In comparison such a synchronised increase in spontaneous postsynaptic currents was absent in the GluK2 KO mice (n = 7). **(C)** Local field potential recordings within the superficial layers of the entorhinal cortex were done in an interphase chamber to record KA-induced gamma oscillations. Low concentrations of KA (300 nM) induced robust oscillations (n = 8 slices). Power spectra analysis revealed a major peak frequency of 40 Hz. The KA-induced gamma oscillations were blocked by the KAR/AMPAR-antagonist NBQX. **(D)** Gamma oscillations were completely abolished in the GluK2 KO mice (n = 7 slices).

We observed during whole-cell patch-clamp recordings from L3Ps, rhythmic postsynaptic currents following the application of low doses of KA. Figure 5-02A shows an example in which under baseline conditions little spontaneous activity was recorded. However, following the application of 300 nM KA a massive increase in spontaneous postsynaptic currents was observed, which had a frequency content of about 10-12 Hz (figure 5-02A, n = 7). In comparison such a synchronised increase in spontaneous postsynaptic currents was absent in the GluK2 KO mice upon bath applying KA (figure 5-02B, n = 7).

Local field potential recordings within the superficial layers of the entorhinal cortex were done in an interphase chamber, a condition which improves the reliability and enhances the power of network oscillations. Low concentrations of KA (300 nM), indeed, induced robust oscillations. Power spectra analysis revealed a major peak frequency of 40 Hz (figure 5-02C, n = 8 slices). The kainate-induced oscillations in the entorhinal cortex were blocked by the KAR/AMPAR-antagonist NBQX. Further, we again made use of the GluK2 KO mice. Figure 5-02D (n = 7 slices) shows that the kainate-induced oscillations were completely abolished in the genetic deletion model.

Such neuronal synchrony in the gamma frequency range is implicated in integrating multimodal inputs in the entorhinal cortex. This synchrony is thus regulated by a tight balance of excitation and inhibition at the single cell level. Developmental or environmental insults result in misconnected neuronal circuits causing an imbalance in the normal synchrony. Often such hyperexcitability is observed in pathological conditions such as epilepsy. On the one hand, low doses of kainate induce neuronal synchrony in acute brain slices but on the other hand, systemic injection of kainate has been used to develop an animal model of temporal lobe epilepsy. Since kainate binds to KARs, a further detailed understanding can be obtained only by characterizing the distribution and role of these receptors at the single cell level.

5.4 Kainate model of epilepsy

One particular interesting aspect of KAR mediated action is the ability of the KAR agonist kainate (KA), which exhibits binding preference for KARs, to evoke epileptic seizures following in vivo administration in mice (figure 5-03; Ben-Ari et al., 2000; Vincent and Mulle, 2009). The interpretation that KAR activation, rather than unspecific side effects due to activation of other glutamate receptors, is responsible for this phenomenon is supported by the fact that GluK2 KO mice have a much higher threshold for the induction of epileptic seizures (Mulle et al., 1998) as compared to wild-type mice.

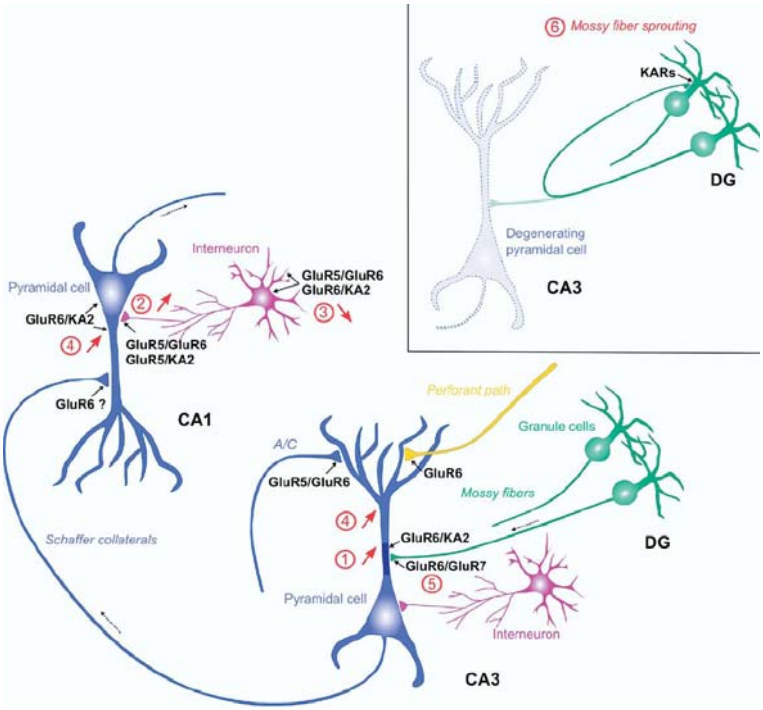

Figure 5-03: Involvement of KARs in the epileptogenic action of KA in the hippocampus. KA can either favor (ascending arrow) or prevent (descending arrow) epileptogenesis depending on KAR subtypes (containing GluK1 or GluK2, formerly GluR5 or GluR6 respectively), neuronal populations (pyramidal or interneurons) and the subcellular localization (somato-dendritic or presynaptic/axonal; Adapted from Vincent and Mulle, 2009).

Epileptic seizures can also be evoked by electrical kindling of the entorhinal cortex or the perforant path (which leads to antidromic excitation of the entorhinal cortex, EC). For this reason, the EC (in particular the mEC) is a prime candidate region for the development of temporal lobe epilepsy (TLE). The extensive interlaminar and intralaminar connectivity of the EC provide an ideal anatomical network for the generation of seizures (Dhillon et al., 2000). Additionally, in the later stages of the development of epilepsy, the EC is one of the first brain regions to suffer from severe cell death. This holds especially true for L3 mEC, making this region of special interest for investigation into the related pathological conditions. Despite this, there has been relatively little research into the basal KAR-mediated synaptic transmission in this region.

5.5 Neuronal loss following seizures in the Entorhinal Cortex

Severe but selective neuronal loss has been in reported in the L3 of the entorhinal cortex following TLE both in humans and rodents (Jarrard et al., 1993; MacGregor et al., 1997; Tolner et al., 2005a; Tolner et al., 2007). Particularly, by using kainate as an epileptic agent,

rats showed extensive loss of neuronal density (upto 60%) while no significant neuronal loss was reported in L2 or L5/6 of the mEC. However, the reason behind this selective neuronal degeneration is not clearly understood and the underlying molecular mechanisms are far from being elucidated. Since KARs do contribute to the hyperexcitability in neuronal networks and that KA acts as a ligand to these receptors, a step forward is to characterize the KAR mediated synaptic transmission of L3 pyramidal cells in the mEC following KA application.

5.6 The L3 pyramidal cell (L3P) in the mEC

In the six-layered cortical structure (Layers I – V/VI (L1-6); figure 5-04A) of the mEC, the L3Ps are easily distinguishable from all other entorhinal neurons based on anatomical location, morphology and characteristic electrophysiological properties (Dickson et al., 1997; Gloveli et al., 1997a; figure 5-04B). For this study we performed whole cell recordings from these neurons (figure 5-04A – experimental design). L3Ps show a typical pyramidal cell like structure with one main apical dendrite extending all the way upto and bifurcating as it nears the pial surface. There are five to ten basal dendrites that extend out from the cell soma as seen in the biocytin filled L3P in figure 5-04B left panel. The corresponding electrophysiological characterization of L3Ps is shown in figure 5-04B right panel. The lack of sag current clearly distinguishes L3Ps from the L2Ss.

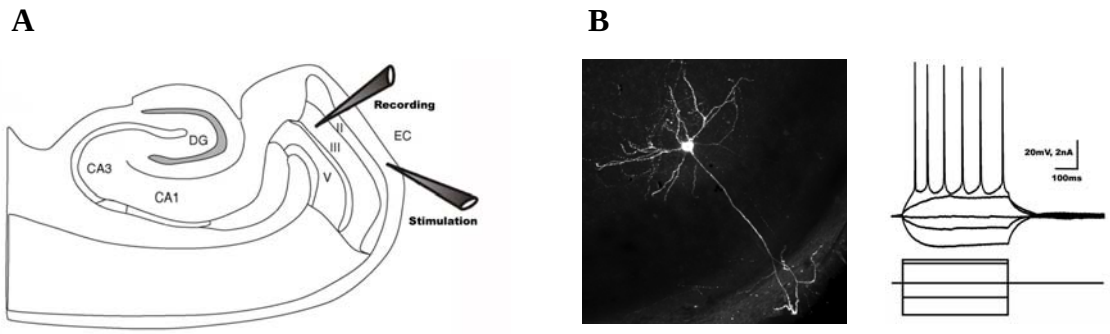

Figure 5-04: (A) Schematic representation of the entorhinal-hippocampal combined slice used in this study with the recording electrode (Recording) in L3 mEC while stimulating (Stimulation) the input from the lateral entorhinal cortex. **(B)** Electrophysiological and morphological properties of a typical L3P.

5.7 Kainate concentration dependent changes in holding current

KA activates non-NMDARs (AMPARs and KARs) with different affinities. Low concentrations of KA (300 nM) activate only KARs while at higher concentrations (1 μM) it acts as an agonist for both AMPARs and KARs [Mulle et al., 1998].

Concentration dependent successive activation of non-NMDARs leads to conductance changes of the cell, reflected in corresponding changes in its holding current. After attaining whole-cell configuration (at -60 mV) a baseline of holding current was obtained, following which increasing concentrations (100 nM, 300 nM, 1 µM and 3 µM) of KA were bath applied for five minutes each. Further increase of KA leads to severely depolarized cells and unstable recordings and was therefore omitted.

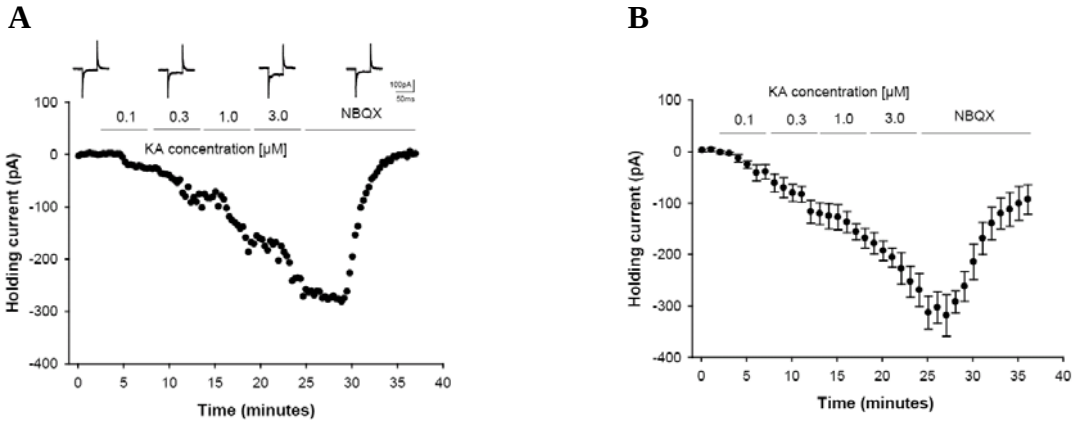

Figure 5-05: Kainate (KA) induced changes in whole-cell holding current on L3Ps. **(A, B)** Time course data for KA (100nM, 300nM, 1µM and 3µM) induced concentration dependent changes in the whole-cell holding current which is antagonized by NBQX (25µM). **(A)** Single experiment with voltage-clamp transients corresponding to baseline, 300nM, 3µM and NBQX. **(B)** Group data (n=6).

The changes in holding current (figure 5-05A - single cell with voltage-clamp transients corresponding to baseline, 300 nM, 3 µM and NBQX; 5-05B - group data, n = 6) at the end of the five minute KA bath application were 53.54 ± 13.95 pA at 100 nM, 131.79 ± 18.98 pA at 300 nM, 201.64 ± 20.55 pA at 1 µM and 303.58 ± 33.25 pA at 3 µM. The KA-induced holding current change was reduced after washing in 25 µM NBQX, indicating that non-NMDARs were involved.

5.8 KAR mediated currents

To study KAR mediated currents in L3Ps it is necessary to isolate this current from the combined current mediated by AMPARs and KARs. Since KA activates both AMPARs and KARs at different concentrations, it was necessary for us to determine the particular KA concentration at which only KARs are activated. Inititially, two different KA concentrations (300 nM and 1 µM) were applied subsequently followed by GYKI (20µM) while monitoring holding current changes (figure 5-06).

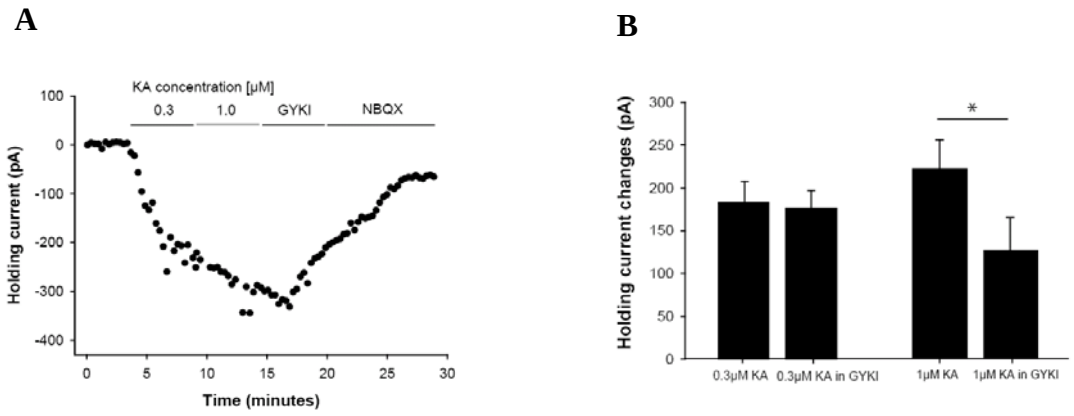

Figure 5-06: Activation threshold of kainate receptors (KARs) on L3Ps. **(A)** Time course data from a single experiment for two different KA concentrations (300nM and 1µM) with subsequent application of GYKI (20µM) and NBQX (25µM). **(B)** While there is no effect of GYKI (20µM) on holding current at 300nM KA ($p=0.344$; $n=4$) there is a significant effect at 1µM KA ($p<0.05$; $n=4$) indicating that at the lower concentration of 300nM only KARs are activated and at higher concentrations, there is a substantial portion of AMPARs that are in addition activated.

Since GYKI showed an effect on the holding current following the 1 µM KA wash-in, it suggested that at this concentration AMPARs are activated along with KARs (figure 5-06). Therefore, to isolate a pure KAR-mediated change in holding current, only the lower concentration of 300 nM KA was bath applied in separate experiments. The holding current changed by 181.58 ± 23.83 pA, following washout of KA, 20 µM GYKI was applied for 5 minutes and then 300 nM KA was reapplied (figure 5-07). On applying 300 nM KA for the second time, the holding current changed by 174 ± 20.7 pA.

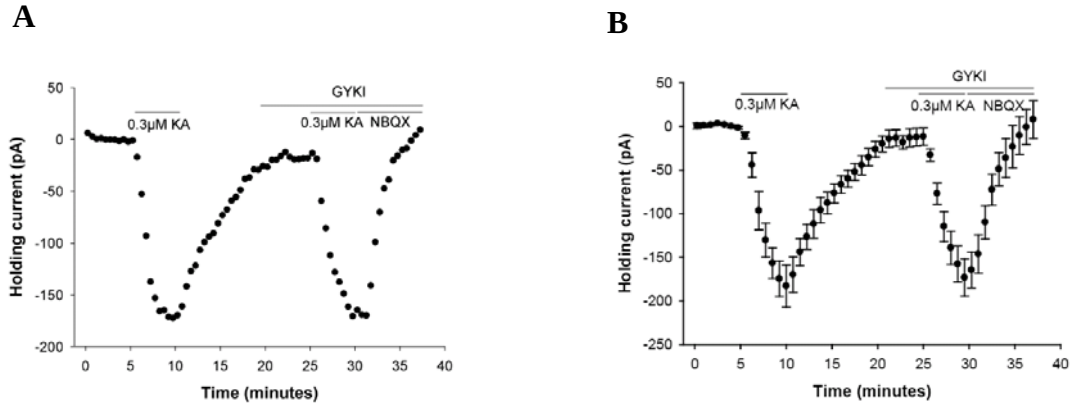

Figure 5-07: Activation threshold of kainate receptors (KARs) on L3Ps. **(A, B)** Time course data for determining the activation threshold of kainate receptors on L3Ps. The change in the whole-cell holding current

by bath application of 300 nM of KA was reversible and following treatment with GYKI (20 µM), 300nM KA was applied for a second time. Holding current decreased to the same amplitude indicating that at a concentration of 300 nM KA, no AMPA receptors are activated. **(A)** Single experiment. **(B)** Group data (n = 4).

Since the changes in holding current in the absence and presence of AMPA receptor blocker, GYKI, was not significantly different, these changes are therefore mediated predominantly by KARs. At 1 µM KA, substantial amount of AMPARs were activated as there was a significant difference in holding current before (229.3 ± 34.5 pA) and after (130.9 ± 38.8 pA) washing in GYKI (figure 5-06B, n = 4). Since at 1 µM KA, AMPA receptors were also activated along with KARs, 300 nM KA was chosen as the working concentration which activated only KARs and no AMPA receptors for L3Ps.

KAR-mediated currents were also analyzed in L2Ss in mEC. We found smaller holding current changes following application of 300 nM KA, in the presence of GYKI, in L2S (108.8 ± 15.4 pA, n = 7) in comparison to L3P (174 ±.20.7 pA, n = 4; figure 5-08A). However, this could be due to differences in membrane capacitance. Indeed, L2Ss have a smaller capacitance in comparison to L3Ps (Gloveli et al., 1997b). In a small number of neurons, the current density between the two neuronal populations was analyzed. No siginificant difference was observed (L2S: 0.63 ± 0.17 pA/pF; L3P: 0.75 ± 0.08 pA/pF; p=0.57; n = 3 for each cell type; figure 5-08B).

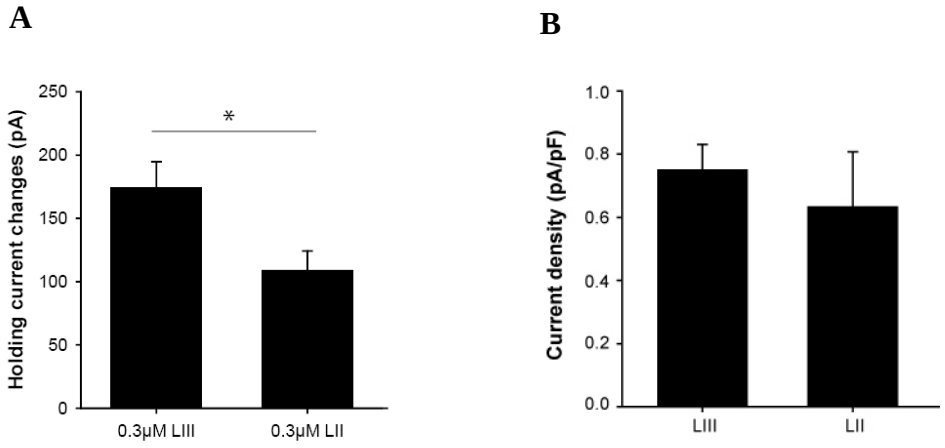

Figure 5-08: Comparison of whole-cell holding current changes between LIII pyramidal neurons (L3P) and LII stellate neurons (L2S). **(A)** L2Ss (108.8 ± 15.4 pA, n = 7) showed smaller following application of 300 nM KA, in the presence of GYKI, in comparison to L3Ps (174 ±.20.7 pA, n = 4). **(B)** Analysis of the current densities in a subset of L2Ss and L3Ps revealed no significant differences (L2S: 0.63 ± 0.17 pA/pF; L3P: 0.75 ± 0.08 pA/pF; p=0.57; n = 3 for each cell type) indicating that the difference in holding current changes is due to the capacitive properties of the two cell types.

5.9 GluK2 is the major subunit mediating the KAR current

KARs have different expression patterns at different synapses and also the composition of subunits vary. Since in the GluK2 KO mice, no gamma frequency could be evoked by washing in kainate, it points to a significant contribution of GluK2 containing KARs in the neuronal excitability in the superficial layers of the mEC. Thus, it was of interest to assess the role of GluK1 and GluK2 subunit in the KAR mediated current at the single cell level in the L3Ps. By bath applying 300nM KA, the holding current in the GluK1 KO changed by 118.13 ± 19.73 pA which was not significantly altered (p = 0.181) when compared to the changes observed in wild-type mice (86.82 ± 7.4 pA, n = 4 each for GluK1 KO and WT). However, in the GluK2 KO there was no change in holding current over the whole duration of bath application of 300 nM KA (figure 5-09A – single cell data; 5-09B – group data, n = 9 for GluK2 KO). This suggests that GluK2 is the major subunit mediating the KAR currents in the L3Ps.

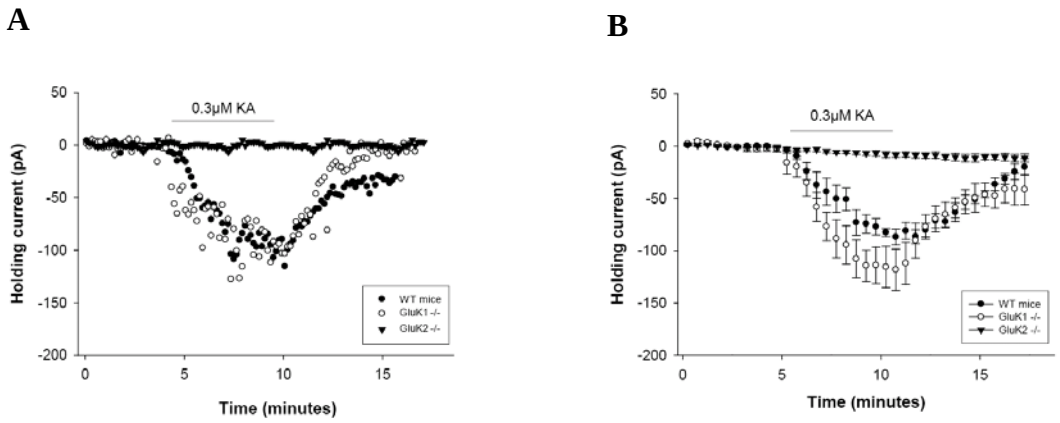

Figure 5-09: Genetic deletion studies to determine the role of GluK1 and GluK2 subunits in the KAR mediated current on the L3Ps. **(A, B)** By bath applying 300 nM KA, the holding current in the GluK1 KO did not change significantly when compared to the wild-type mice (p = 0.181; n = 4). However, no change in holding current was observed for GluK2 KO (n = 9) upon bath applying 300 nM KA indicating that the GluK2 is the predominant KAR subunit responsible for mediating the observed KAR current in these neurons. **(A)** Single experiment. **(B)** Group data (n = 4 each for WT and GluK1 KO and n = 9 for GluK2 KO).

5.10 Characterization of the KARs

RNA editing (Q/R editing) of KARs influences channel properties. The unedited form of the receptor with glutamine (Q) at the Q/R site renders the channel permeable to Ca^{2+} whereas the edited form of the receptor with the positively charged arginine (R) makes it Ca^{2+}

impermeable (Seeburg et al., 1998; Seeburg et al., 2003; Sprengel et al., 1998). To determine whether the KARs present on L3Ps were of the edited or non-edited form, an IV curve was computed by uncaging 200 µM MNI-Glutamate over the cell soma in the presence of 100 µM APV, 2 µM Gabazine and 20 µM GYKI (figure 5-10A-D). Initially the cell was held at -60mV and a baseline of stable responses (20 to 25 sweeps, pulse of 5 ms duration with a inter- stimulus interval of 30 seconds) was obtained in the presence of ACSF containing APV and Gabazine only. After washing in GYKI, the isolated KAR current was 34.32% (± 2.05%) of the baseline value (figure 5-10C, n = 5). This remaining current in GYKI was mediated by KARs because they were blocked completely by NBQX (25 µM).

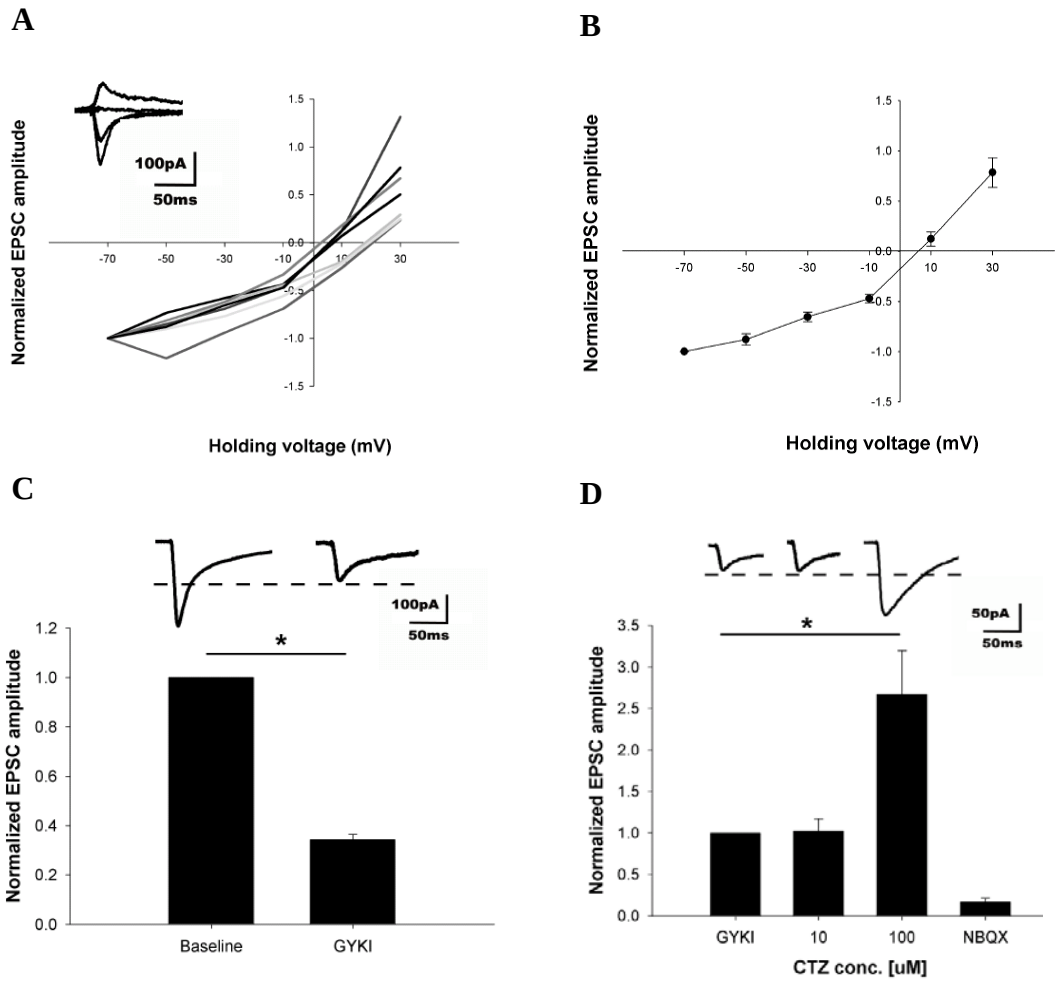

Figure 5-10: IV curve and characterization of kainate receptors on L3Ps using photolytic uncaging of glutamate. **(A)** The peak current for each individual cell (n = 7) is plotted against the membrane potential along with the corresponding superimposed current traces (inset). **(B)** Group data (n = 7). A linear relationship between voltage and current, both at negative and positive potentials suggested the KARs on L3Ps to be mostly of the Ca^{2+} impermeable edited form. **(C)** Photolytic uncaging of glutamate at the cell soma elicited inward currents, which were reduced to 34.32% (± 2.05%; $p<0.01$; n=5) of the baseline value in the presence of GYKI (20 µM). **(D)** At 20 µM of GYKI no residual AMPA current is seen as there is no potentiation of the resultant EPSC upon

application of AMPAR desensitization blocker CTZ (10 μM; p = 0.956; n = 4). However, at a higher concentration of CTZ (100 μM), the effect of GYKI is antagonized ($p < 0.01$; n = 6). In the presence of GYKI, APV and Gabazine, the holding membrane potential was changed in steps of 20mV from -60mV to 40mV and at each step, 5 responses (5 laser flashes with inter-stimulus interval of 30 seconds) were recorded by uncaging glutamate over the cell soma.

For the IV curve of the KARs, the holding membrane potential was changed in steps of 20mV from -60mV to 40mV and at each step, five responses were recorded. Posthoc analysis was performed by averaging these five responses. Calculated junction potential of 10mV was subtracted from the holding membrane potential. A linear relationship between voltage and current, both at negative and positive potentials (figure 5-10A-B, n = 7) suggested the KARs on L3Ps consist mostly of the Ca^{2+} impermeable edited form.

To prove that the IV curve was for purely KAR mediated responses, at the end of each experiment, cells were brought back to a holding membrane potential of -60mV and either 10 or 100 μM Cyclothiazide (CTZ) was added. There was no potentiation of the response on washing in 10 μM CTZ proving that there was no contribution of AMPARs. However, at a higher CTZ concentration (100 μM), the drug antagonizes GYKI (Eder et al., 2003) and therefore a large potentiation of AMPARs was seen in this case (figure 5-10D, n = 4 and 6 for 10 μM and 100 μM CTZ respectively). In separate experiments, 10 μM CTZ was added to mixed AMPAR and KAR responses and this concentration was sufficient to potentiate any existing AMPAR component in the response (data not shown).

5.11 Synaptic activation of KARs

To investigate the contribution of synaptic KARs to the observed currents, recorded L3Ps in the whole-cell mode were stimulated by placing a stimulation electrode in L1 mEC. In this region, the distal apical dendrites of the L3P synapse onto the input pathways from the lateral EC. Baseline $EPSC_{AMPA+KA}$ was recorded in the presence of ACSF containing 50 μM APV, 2 μM Gabazine and 20 μM SCH 50911. After a stable baseline response, 20 μM GYKI was washed in to isolate $EPSC_{KA}$ (figure 5-11A, n = 8). The EPSC was blocked in GYKI. Since there was no $EPSC_{KA}$ in the recorded neurons, the apparent conclusion was that there was no synaptic KARs activated upon stimulation of this pathway.

To verify this finding high frequency stimulations (5 pulses at 200 Hz, 10 pulses at 200 Hz, 5 pulses at 25 Hz and 10 pulses at 25 Hz; Castillo et al., 1997) were performed in the presence

of GYKI. There was no detectable $EPSC_{KA}$ under these stimulation conditions indicating the absence of synaptic KARs in the distal dendritic region (figure 5-11B).

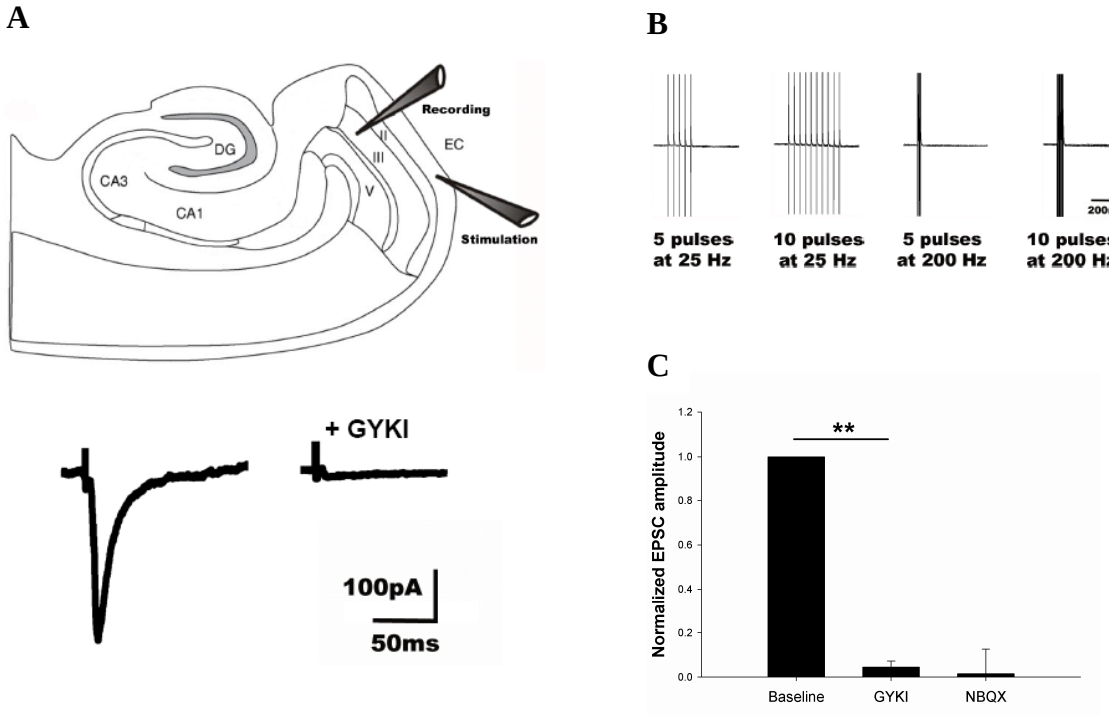

Figure 5-11: Synaptic activation of KARs in L3Ps **(A, B)** Recorded L3Ps were held in the whole-cell mode while stimulating the afferent pathway L1 mEC. **(A, lower panel)** In the presence of GYKI (20 µM), no synaptically evoked $EPSC_{KA}$ is detected (n = 8) as seen in an example trace from a single experiment. **(B)** High frequency stimulations (5 pulses at 25 Hz, 10 pulses at 25 Hz, 5 pulses at 200 Hz and 10 pulses at 200 Hz) were performed in the presence of GYKI. There was no detectable $EPSC_{KA}$ under these stimulation conditions as well indicating the absence of synaptic KARs upon stimulation of this pathway. **(C)** The baseline EPSC was completely blocked in GYKI (20 µM) in all L3Ps ($p < 0.01$, n = 8) recorded.

In a further experiment, synaptic stimulation in L1 mEC was combined with glutamate uncaging, thereby recording first a synaptic current and thereafter a somatic current from the same cell while all other conditions remained constant. After washing in GYKI, the somatic current was reduced to 30.96% ± 4.45% of the baseline value while the synaptic current was blocked (figure 5-12).

Our data suggests that there is negligible contribution of synaptic KARs upon stimulating L1 mEC. However, a KAR current was evoked by uncaging glutamate over the cell soma indicating that the functional KARs could be limited to the somatodendritic region of L3Ps. It has been shown that the distribution of KARs can be pathway specific (Castillo et al., 1997; Vignes et al., 1997).

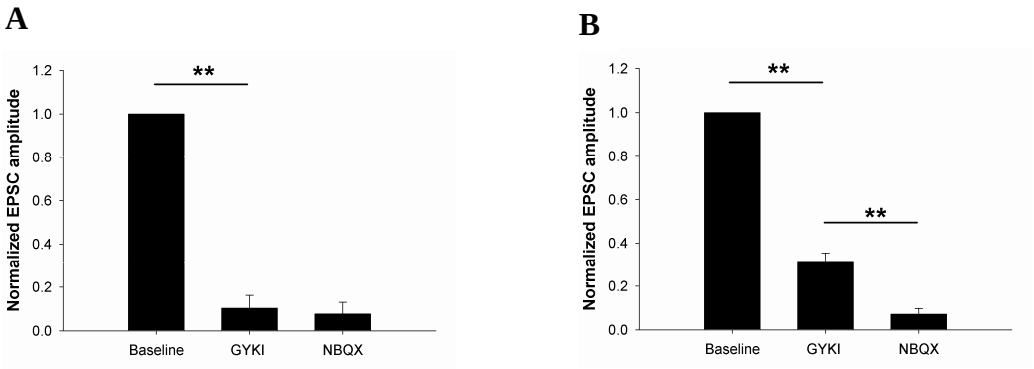

Figure 5-12: Synaptic versus somatodendritic activation of KARs in L3Ps. In a subset of recorded cells, KAR mediated currents were evoked by stimulating the L1 mEC and glutamate uncaging on the cell soma sequentially and under the same recording conditions. L1 mEC stimulation evoked synaptic currents while the following glutamate uncaging evoked somatic currents. **(A)** Negligible contribution of synaptic KARs was observed upon stimulating L1 mEC. **(B)** KAR mediated current was evoked by glutamate uncaging indicating that the functional KARs could be limited to the somatodendritic region of L3Ps.

To determine, whether any other input pathway would yield a significantly higher proportion of synaptic KAR mediated current, we stimulated at the border of L2-3 mEC. When kainate currents were isolated in the presence of GYKI, a GYKI resistant component was seen (10.24% ± 1.1% of baseline), which was blocked by NBQX (figure 5-13, n = 5). Thus by stimulating a different pathway, a $EPSC_{KA}$ could be evoked in L3Ps.

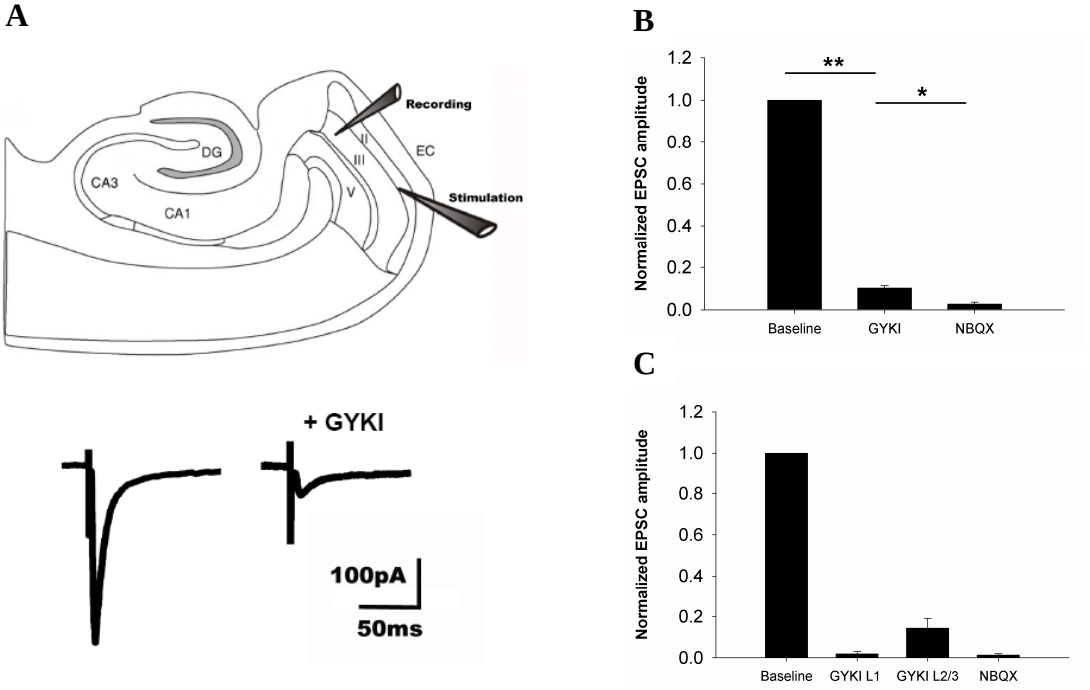

Figure 5-13: Pathway specific activation of synaptic KARs in L3Ps **(A, B)** To determine, whether any other input pathway would yield a significantly higher proportion of synaptic KAR mediated current, the border of L2-

3 mEC was stimulated. In the presence of GYKI, an $EPSC_{KA}$ was observed (10.24% ± 1.1% of baseline; n = 5) as seen in an example trace from a single experiment **(A, lower panel)**. **(B)** In the presence of GYKI (20 μM), $EPSC_{KA}$ could be isolated upon stimulation of this second pathway. This $EPSC_{KA}$ could be blocked further by NBQX (20 μM). **(C)** In a subset of recorded cells, stimulation electrode was first placed in L1 mEC, thereby evoking no $EPSC_{KA}$. However, relocating the electrode within the same experiment to a second position at the border of L2-3 mEC and without increasing the stimulation intensity, an $EPSC_{KA}$ was evoked in the same cell (14.31% ± 4.7% of baseline). Thus by stimulating a different pathway, a $EPSC_{KA}$ could be evoked on L3Ps, suggesting the existence of synaptic KARs in a pathway specific manner.

In an additional experiment, the stimulation electrode was first placed in L1 mEC, thereby evoking no $EPSC_{KA}$. However, relocating the electrode within the same experiment to a second position at the border of L2-3 mEC without increasing the stimulation intensity, $EPSC_{KA}$ was evoked in the same cell (14.31% ± 4.7% of baseline; data not shown).
Taken together, the data suggests the presence of KARs limited to the somatodendritic region of L3Ps (somatic uncaging and L2-3 stimulation) and a clear lack of KARs in the distal dendrites.

5.12 Discussion and Outlook

This study focuses on L3 of the mEC, which provides input to the hippocampal CA1 region and subiculum via the perforant path. Since this particular layer suffers from extensive neuronal cell death after epileptic seizures (Jarrard et al., 1993; MacGregor et al., 1997; Tolner et al., 2005a; Tolner et al., 2007), characterization of its synaptic connectivity and modes of synaptic transmission are of critical interest. This study shows that KAR mediated currents could be evoked in L3Ps. Such currents possess properties of Ca^{2+} impermeable KARs and were mediated by GluK2 containing receptors.
KARs can be localized both post- and pre-synaptically. Postsynaptically they facilitate synaptic currents and influence signal integration (Frerking et al., 2002). Presynaptically they regulate transmission, e.g. by decreasing the probability of transmitter release. Bath application of KA evoked a reversible increase in the holding current, which could also be observed in the presence of the specific AMPAR blocker GYKI 53655, indicating a KAR mediated effect. Further, at a concentration of 300 nM KA, KARs are selectively activated. Although the subunit composition of individual KARs is not completely clear, ionotropic KARs often include either GluK1 or GluK2 subunits (Lerma, 2006; Pinheiro et al., 2006; Huettner 2003; Chittajallu et al., 1999). Using genetically modified mice lacking either GluK1 or GluK2, we have shown unambiguously that GluK2 and not GluK1 subunit

contribute to the recorded KAR currents. Since there is considerable presence of transcripts of other kainate receptor subunits (GluK3, GluK4 and GluK5; Bahn et al., 1994; Wisden et al., 1993), one cannot exclude the contribution of heteromeric GluK2 KARs towards the observed kainate current.

Laser mediated glutamate uncaging in the somatic region of L3Ps reliably produced KAR mediated currents in the presence of GYKI and were blocked by the application of NBQX. Additional evidence that these current was mediated exclusively by KAR was provided by the fact that the remaining current was unaltered during application of the AMPAR desensitization blocker CTZ.

The AMPAR subunit GluA2 as well as the KAR subunits GluK1 and GluK2 can undergo Q/R editing, a process determining the calcium permeability, rectification and conductance of the ion channels (Seeburg et al., 1998; Seeburg et al., 2003; Sprengel et al., 1998). Whereas GluA2 editing seems to be almost complete in the adult animal, and disruption of the editing process is lethal (Bruse et al., 1995; Higuchi et al., 2000), KAR editing increases only to a degree of 60-80% during development (Seeburg et al., 1998; Seeburg et al., 2003; Sprengel et al., 1998) and interfering with GluK1 editing showed only a mild phenotype (Sailer et al., 1999). On the other hand, analysis of mutant mice which do not undergo GluK2 editing show NMDAR independent LTP at the EC-DG synapse as well as an increased vulnerability to seizures (Vissel et al., 2001), arguing for a developmental need to down regulate the unedited Ca^{2+} permeable GluK2 receptors and replace them by edited ones.

These considerations, together with the potential role of the EC in epilepsy led us to investigate whether the dominating electrophysiological phenotype of L3Ps is of the unedited, rectifying and Ca^{2+} permeable form or not.

It turned out that the majority of these channels consist of non-rectifying channels, suggesting that the critical receptor subunit is of the edited form. As a functional consequence, a large proportion of these receptors are Ca^{2+} impermeable. Although not very much is known about the physiological role especially of KAR Q/R editing (Sprengel et al., 1998), they might play a role in certain pathologic conditions. For example, abnormalities in the ratio of the unedited/edited forms have been reported as a consequence of ischemia (Paschen et al., 1996). Furthermore, analysis of AMPAR and KAR editing ratio in epileptic patients revealed differences in various brain regions, suggesting a possible involvement of the editing process in this disease (Grigorenko et al., 1998; Kortenbruck et al., 2001; Musshoff et al., 2002). It would be of interest to investigate a potential role of GluK2 editing in the developmental course of epilepsy in the EC.

We tried to evoke synaptic KAR mediated responses by stimulating the inputs from the lateral EC by placing a stimulation electrode in L1 mEC. Although we could reliably evoke AMPAR mediated synaptic transmission, which confirmed intact connectivity in our working stimulation conditions, no detectable synaptic current was found after blocking AMPAR mediated currents with GYKI. This argues against synaptically localized KARs, at least in the distal apical dendrite of L3Ps. A similar phenomenon was observed by (Castillo et al., 1997), showing little synaptic transmission after blockade of AMPAR mediated transmission at mossy fibre synapses in the CA3 region of the hippocampus. However, short high frequency stimulation during AMPAR blockade (in the presence of GYKI) in this study lead to a potentiation of the KAR mediated currents. One possible interpretation of these results would be the existence of extrasynaptic KARs that could only be activated by glutamate spillover resulting from synchronous activation of excitatory fibres. To test whether this scenario also holds true for the L1 input to the L3Ps, several similar high frequency protocols were applied. There was no detectable KAR mediated current observed in any case. The most straightforward interpretation of these results is that the distal apical dendrites of L3Ps are devoid of KARs. Also recently, astrocytic glutamate release has been implicated in extrasynaptic activation of neuronal KAR (Liu et al., 2004), offering a potential explanation and functional role for these receptors, in addition to activation via spillover of synaptically released glutamate after intense stimulation.

However, moving the stimulation electrode to the L2-3 border reliably yielded synaptic responses in the presence of GYKI. Based on these results, we conclude that L3Ps have functional KARs that contain GluK2 subunit and are restricted to the somatodendritic region in this layer.

Recent studies (West et al., 2005; West et al., 2007) show that L3Ps show small but significant residual synaptic currents after blocking AMPAR mediated currents via the application of 100 µM GYKI 52466 by stimulating at the border of L2-3. These responses could be potentiated by brief high frequency stimulation. The present study confirms one of the results obtained there, namely the existence of KAR mediated synaptic currents evoked by L2-3 stimulation. Furthermore we extend their findings by identifying the responsible KAR subunit involved, no synaptic KAR current upon L1 stimulation and that a KAR current is evoked upon stimulating at the border of L2-3 mEC.

We have shown that GluK2 containing KAR-mediated synaptic currents are exclusively restricted to the somatodendritic region of L3Ps, where they are most likely boosting excitatory synaptic transmission, as reported for other synapses (Frerking et al., 2002).

Furthermore, there is connectivity between superficial and deeper layers and within L3 itself (Dhillon et al., 2000). Also L3Ps project via the perforant path to the CA1 and subiculum region. Boosting and prolonging the influx of positive charges during stimulation might be an important mechanism influencing the time window required to form long term association between different inputs arriving in this region. The observed localization of KAR mediated currents might also be an explanation for the almost complete loss of L3Ps, often observed in experimental models of epilepsy.

Changes in the power of gamma oscillations have been reported to occur in animal models of psychiatric diseases (Cunningham et al., 2006). Although this is a purely correlative observation, it is interesting to note that these alterations occurred exclusively in the entorhinal cortex and not in the hippocampus. In addition oscillatory behaviour in neuronal circuits might be related to cognitive performance and pathological mental states (Whittington et al., 2000), as suggested by the action of several clinically used drugs. The idea of involvement of KAR in cognitive processes is furthermore supported by genetic studies which have identified mutations in GluK2 as a potential cause for mental retardation (Motazacker et al., 2007).

Analyzing the cellular and subcellular distribution and properties of these receptors and investigating their functional role in network behaviour such as oscillations will therefore most probably provide insights into underlying physiological mechanisms of cortical and cognitive function and their pathophysiological alterations.

5.13 Pathophysiological hyperexcitability

Though kainate and kainate receptors have been implicated in hyperexcitability, there are many other players contributing to similar pathologies but through mutually exclusive pathways. Briefly, we will introduce a novel mechanism by which glutamatergic synaptic transmission is modulated by a member (Plasticity related gene-1; PRG-1) of a class of lipid phosphate phosphatases. PRG-1 is a neuronal, synaptic molecule expressed by glutamatergic neurons and ultrastructural analysis of PRG-1 expression shows preferential expression of PRG-1 at the postsynaptic density (figure 5-14A-C). Deletion of prg-1 in mice leads to hyperexcitability (figure 5-14D), epileptic seizures and augmentation of EPSCs (figure 5-14E), but not IPSCs. *In utero* electroporation of PRG-1 into deficient animals revealed that PRG-1 modulates excitation at the synaptic junction. Mutation of the extracellular domain of PRG-1 crucial for its interaction with lysophosphatidic acid (LPA) abolished the ability to

prevent hyperexcitability. As LPA application in vitro induced hyperexcitability in wild-type but not in LPA_2 receptor-deficient animals and uptake of phospholipids is reduced in PRG-1-deficient neurons, we assessed PRG-1/LPA_2 receptor-deficient animals, and found that the pathophysiology observed in the PRG-1-deficient mice was fully reverted. Thus, PRG-1 is an important player in the modulatory control of hippocampal excitability dependent on presynaptic LPA_2 receptor signaling.

PRG-1 expression on dendrites is limited to glutamatergic neurons and reaches maximum levels in the third week of life (data not shown), a time when synaptogenesis peaks and neuronal connections are shaped. In parallel, expression of LPA_2–receptors is high (Contos and Chun, 2000; Contos et al., 2000) at this critical period of seizure susceptibility/increased hyperexcitability (Ben-Ari et al., 2007), in which an imbalance between excitatory and inhibitory inputs in the almost developed neurons is believed to occur (Ben-Ari, 2006).

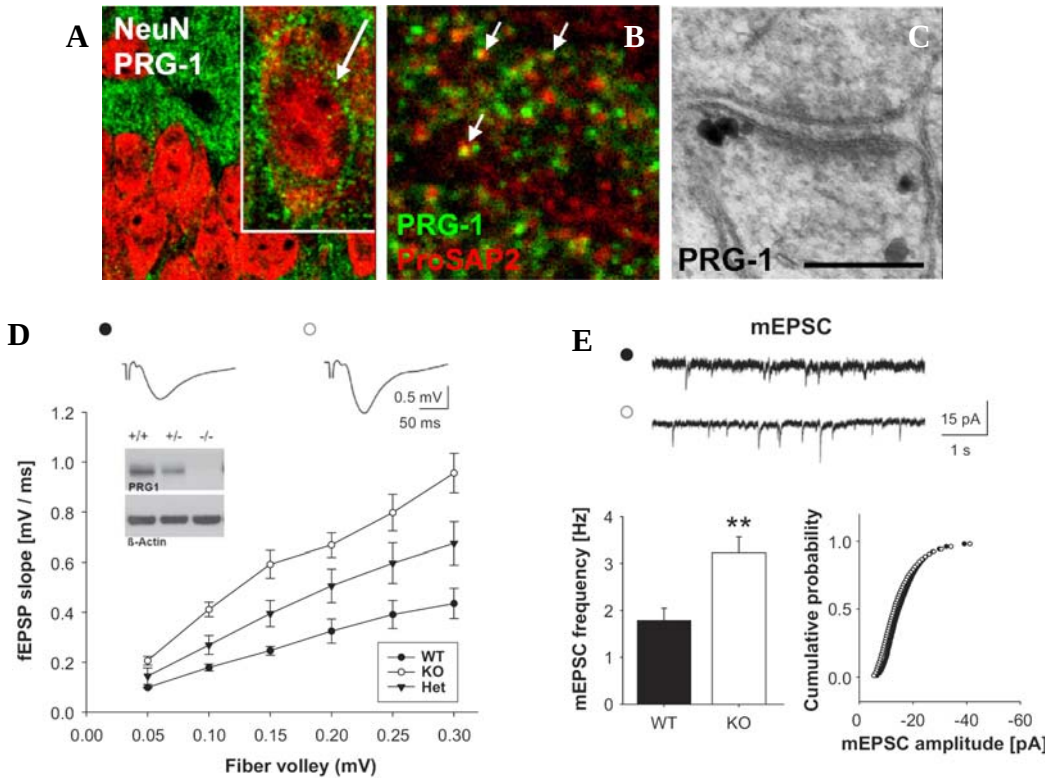

Figure 5-14: PRG-1 is a neuronal, synaptic molecule expressed by glutamatergic neurons. **(A)** PRG-1 expression in the hippocampal CA1 pyramidal cells shows high expression in dendrites, with membrane-bound expression shown in higher magnification (inset, arrows). **(B)** PRG-1, mainly expressed on dendrites, colocalized with ProSAP2. **(C)** Ultrastructural analysis of PRG-1 expression shows preferential expression of PRG-1 at the postsynaptic density (the scale bar represents 200 nm). Hyperexcitability in CA1 pyramidal cells in PRG-1 KO mice **(D)** Extracellular fEPSPs were evoked by Schaffer collateral stimulation. fEPSP slope is plotted for WT, PRG-1+/- and PRG-1-/-. Increased network excitability is seen for the PRG-1-/- mice (white) compared with

WT mice (black). The input-output curves indicate a gene-dose-dependent effect of PRG-1 that is also reflected in the adjacent western blot of brain homogenates. **(E)** A significantly higher mEPSC frequency was observed in PRG-1 KO CA1 pyramidal cells compared to WT cells (left panel), however the amplitude of these events did not significantly vary between the two groups (right panel).

The lack of apparent morphological changes in PRG-1 KO animals, and specifically the presence of GABAergic neurons as in WT animals, indicated that changes in network properties were due to a pathological increase of excitatory synaptic transmission on otherwise unaffected neurons. Field potential recordings of hippocampal slices confirmed this, showing increased excitability in PRG-1 KO mice (figure 5-14D) while intrinsic properties of the CA1 neurons and the overall morphology were not altered.

Rescue of normal excitatory events in single PRG-1−/− cells by PRG-1 *in utero* electroporation demonstrates PRG-1's effect on neuronal excitability at individual glutamatergic synapses (figure 5-15A-B right panel). In turn, deletion of prg-1 in single cells of conditional PRG-1 KO mice using Cre-recombinase *in utero* electroporation was sufficient to elicit the synaptic dysfunction (figure 5-15A-B left panel). Thus, our data reveal that hyperexcitability in PRG-1 KO animals can only be explained by the lack of the modulatory activity of PRG-1 at the synapse. As this single-cell KO approach never resulted in epileptic discharge in the animals and the recorded PRG-1 KO neurons were connected by normal presynaptic afferents deriving from PRG-1-expressing cells, these findings confirm that PRG-1 influences excitatory transmission from the postsynaptic side. Additionally, AMPA receptors at glutamatergic synapses and their physiological function appeared to be normal. Therefore, increased excitation at glutamatergic synapse, so far studied in CA1 and CA3 (data not shown) in vitro, and related hyperexcitability and seizures in vivo, both caused by lack of postsynaptic PRG-1, could not be explained by alteration in synaptic innervation or changes to postsynaptic receptors.

Thus, we addressed a direct role of PRG-1 in terms of its relation to lipid phosphate phosphatases. LPPs have been proposed as negative regulators of receptor-directed signaling cascades induced by bioactive lipid phosphates such as LPA or S1P (Brindley, 2004; Sigal et al., 2005). However, little is known about the physiological role of these molecules in the living organism, particularly the brain. A function for germ cell migration of one class of LPP homologs in vivo has been inferred from deletion and ectopic expression experiments in Drosophila (Renault et al., 2004; Starz-Gaiano et al., 2001). Homology of the membrane-spanning N-terminal part of PRG-1 to the LPP family clearly indicates their evolutionary

relationship and implies that the binding partner or ligand of PRG-1 is a bioactive lipid such as LPA (Todd et al., 2002). PRG-1 and LPPs share amino acids shown to be crucial for the interaction of those molecules with lipid phosphates. In particular, mutation of a highly conserved histidine within the extracellular domain is known to abolish this interaction (Starz-Gaiano et al., 2001; Zhang et al., 2000). Precisely this exchange from histidine to lysine, when performed in PRG-1 at position 253, resulted in a protein no longer able to rescue the KO phenotype after *in utero* electroporation (figure 5-16A). These data support the hypothesis that PRG-1 can interfere with glutamatergic signal transduction by interacting with lipid phosphates in the synaptic cleft from the postsynaptic side.

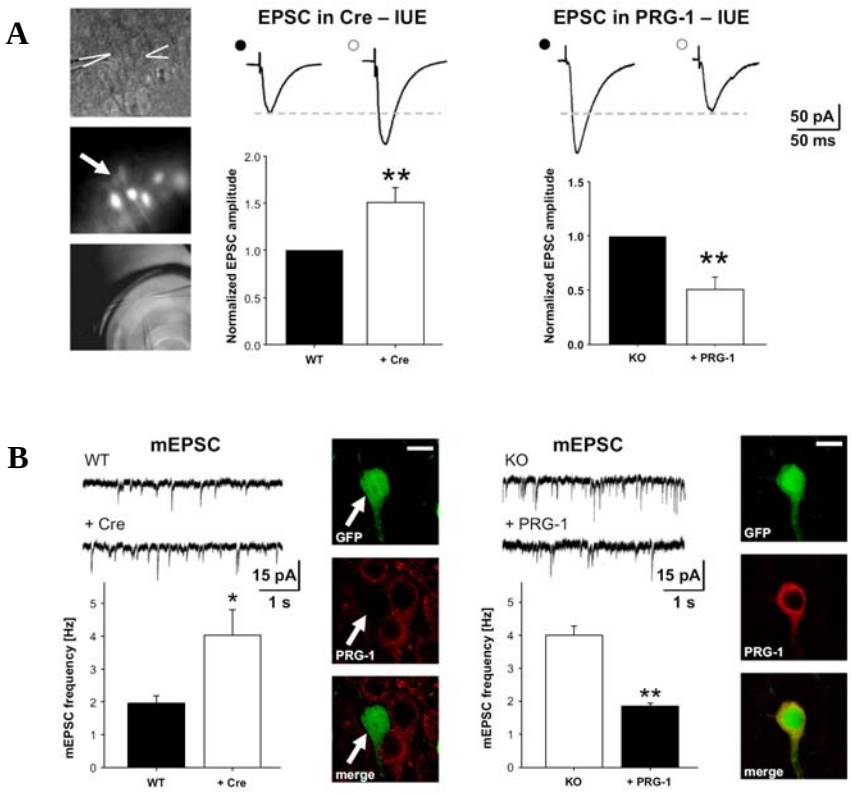

Figure 5-15: PRG-1 Action in Single CA1 Neurons in Acute Slices. Using *in utero* electroporation prg-1 was deleted (GFP+) in conditional or re-expressed (GFP+) in constitutive PRG-1 KO mice in a subset of cells. **(A)** Left: In simultaneous recordings (upper image) from GFP+ (KO) and GFP- (WT, arrow) CA1 pyramidal neurons (middle image) EPSC amplitude (experimental setting: lower image) was significantly increased in KO cells compared to WT cells. Right: In simultaneous recordings from GFP+ (PRG-1+) and GFP- (KO) CA1 pyramidal cells EPSC amplitude was significantly decreased in PRG-1-expressing cells compared to KO cells. **(B)** Left: mEPSCs were recorded from GFP+ (KO) and GFP- (WT) cells. Significantly higher mEPSC frequency was observed in the PRG-1-/- cells compared to WT neurons. Arrow points to GFP+ cell, in which PRG-1 (red) has been deleted. Right: mEPSC frequency was significantly reduced in the GFP+ (PRG-1-expressing KO) cells

compared to the GFP- (KO) cells. GFP signal in neurons indicates PRG-1 expression, confirmed by PRG-1 (red) immunolabeling. Data are represented as mean ± SEM *p < 0.05, **p < 0.01. The scale bar represents 15 µm.

The LPA_2 receptor's presynaptic location at the excitatory junction and the fact that LPA does not increase excitability in LPA_2 receptor-deficient mice suggests this bioactive phospholipid is directly involved in controlling glutamatergic transmission. Consequently, the absence of both overexcitation at the synapse (figure 5-16B and epileptic activity (figure 5-16C) in PRG-1/LPA_2 receptor-deficient mice indicate PRG-1 modulates LPA-mediated control of excitatory discharge via the LPA_2 receptor.

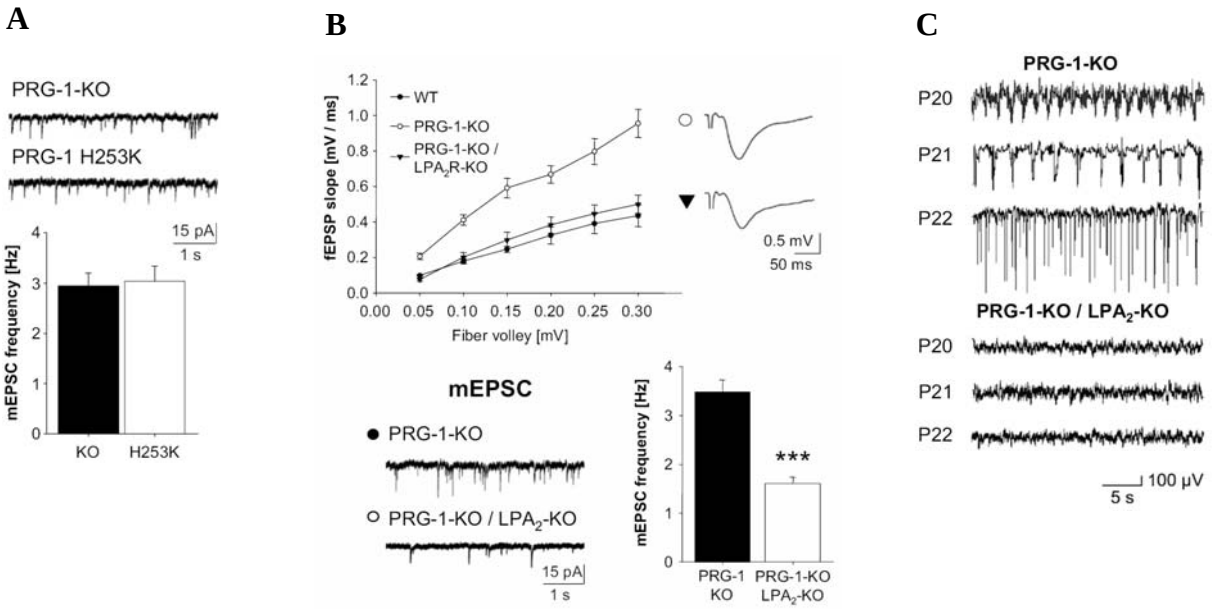

Figure 5-16: Interaction of PRG-1 with LPA2 thereby influencing phospholipid signaling. **(A)** Mutated PRG-1 (H253K) lacking the ability to interact with phospholipids was expressed in a subset of cells (GFP+) in PRG-1 KO animals using *in utero* electroporation mEPSC frequency at P21 was not reduced to WT levels in PRG-1 (H253K)-expressing neurons after electroporation of the WT prg-1 construct. **(B)** Normal network excitability is seen in PRG-1 KO/LPA2-R KO-/- animals when compared to the PRG-1 KO mice. In contrast to PRG-1 KO mice, double KO animals showed fEPSP slopes similar to WT animals. mEPSC frequency in CA1 pyramidal neurons in hippocampus from double KO mice also returned to WT levels and did not show the increase seen in PRG-1-/- animals. **(C)** In vivo recordings of double KO animals did not display the hypersynchrony around P21 as seen in PRG-1-/- mice of same age.

Changes in lipid phosphate species have been linked to forms of human epilepsy (Hermansson et al., 2005). Receptors for lipid phosphates have been described (Fukushima and Chun, 2001) as acting via G proteins and are putative transducers of a signal mediated by bioactive lipids at the synapse. Furthermore, it has been reported that lipid phosphates and

their receptors can interfere with excitability (MacLennan et al., 2001) and exocytosis via G protein-coupled receptor-mediated signaling pathways (Pan et al., 2007). This indicates that modulation of neuronal transmission might involve bioactive lipids such as LPA acting via presynaptic LPA_2 receptors, a mechanism that is in turn controlled by PRG-1 from the postsynaptic side specifically at the glutamatergic junction.

Neuronal synchrony and physiological maintenance of neuronal excitability require the interplay of many key molecules. Here we present the critical contribution of two such molecules involved in modulating neuronal excitability. GluK2 containing KARs play a vital role in synchronizing the mEC microcircuitry to generate gamma oscillations. Lack of these receptors abolishes such synchrony which is necessary for binding sensory information from different cortical areas. Disease models are reported where information flow is impaired due to desynchrony of cortical oscillations. Secondly, at the synaptic level, genetic deletion of PRG-1 tilts the fine synaptic homoestasis at glutamatergic synapses resulting in hyperexcitability. Thus the fine balance between physiological synchrony and pathological hyperexcitability is under tight control of many molecules; each of which modulates the information flow in neuronal microcircuit in a specific and targeted way.

SUMMARY

Neuronal microcircuits are the fundamental units of brain functions. Such microcircuits are at the interface between the elementary building blocks, namely excitatory and inhibitory neurons and functional neuronal networks. The structure of neuronal microcircuits matures over development and stabilizes in the adult. Developmental or environmental insults often result in misconnected circuits. By studying normal or misconnected neuronal microcircuits one can better understand the underlying functions in physiological or pathological (neurodegenerative diseases) conditions.

In my doctoral thesis, I aimed to understand the functional microcircuitry of the entorhinal cortex, in particular the medial entorhinal cortex (mEC), in normal functions and disease. Past research has focused mainly on the anatomical circuitry of the entorhinal cortex. However, recent *in vivo* work has revealed the functional relevance of the entorhinal cortex as an independent computational unit serving a key role in spatial navigation and not simply an information hub between the cortex and hippocampus. The chronological gap between structural and functional studies has led to many open questions. In addition the mEC has been implicated heavily in Alzheimer's disease, temporal lobe epilepsy (TLE), Schizophrenia and many other neuropsychiatric disorders. In chapters 1 and 2, I introduce the concept of a neuronal microcircuit and emphasize the need to understand it both at the structural and functional levels. Further, I introduce the mEC's role in spatial navigation and pathophysiology and the importance of looking at the underlying microcircuitry which might further our understanding in these directions.

In chapter 3, I discuss the available techniques for studying neuronal microcircuitry, introduce our fast-scanning photostimulation software and in depth compare its performance to the other standard techniques and software available. By mapping the intralaminar synaptic connectivity of Layer 2 stellate cells (L2S) of the mEC as a model cell, the applicability, resolution and repeatability of the software was validated. Further, the detection algorithm for distinguishing photo-induced events from background events was tested and proven to be capable of faithfully differentiating between the two kinds of photo-induced events – the direct responses and the synaptic inputs.

In chapter 4, the main findings of the functional microcircuitry of the two projection neurons in the L2 mEC – Layer 2 stellate cell (L2S) and the Layer 2 pyramidal cell (L2P) – are presented. Results reveal the existence of excitatory microcircuits with a cell-type–specific separation of intralaminar recurrent connections and ascending interlaminar feedback connections as well as modular organization. L2Ss display more intralaminar recurrent connectivity; in comparison, L2Ps receive a larger fraction of the ascending interlaminar feedback connectivity from deep layers of the mEC, constituting the hippocampal feedback loop. Ascending interlaminar feedback connections to L2 are spatially organized in modules with distinct properties for the two cell types.

Neuronal synchrony is an inherent property of neuronal microcircuits. Brain rhythms of different temporal frequencies, especially gamma oscillations, have been attributed important roles in binding information from several brain areas. In chapter 5, a model for studying the role of mEC microcircuitry in neuronal synchrony and excitability is assessed, the molecular mechanisms behind such synchrony and pathological consequences of hyperexcitability. From the results, we conclude that GluK2 containing kainate receptors are crucial players in the kainate-induced gamma oscillations in the superficial layers of the mEC. Layer 3 pyramidal cells (L3Ps) contain KARs that are limited to the somatodendritic region. The specific expression and distribution of GluK2 containing KARs on L3Ps might render them sensitive to seizure related insults as is often seen in animal models of TLE (eg: kainate model, pilocarpine model etc.). Since epilepsy can result from hyperexcitable neuronal networks, there are more than one way and region where and how this might occur. As an outlook, from another study that I was involved in, we propose the role of a novel mediator of synaptic transmission, PRG-1 (plasticity related gene-1) in modulating excitability in neuronal networks. PRG-1 is found exclusively at glutamatergic synapses on the postsynaptic side and modulates synaptic transmission. Genetic deletion of PRG-1 results in severe hyperexcitability (chapter 5) in the hippocampus leading to pathological seizures.

Taken together these findings reveal the importance of studying the functional microcircuitry of a cortical region in normal and pathological conditions. The cell-type specific and modular organization of inputs upon the L2S and L2P further the knowledge as to how information is transferred within the local microcircuitry of the entorhinal cortex. The deep layer inputs have been implicated to be of pivotal importance for the L2 cells to perform its role in spatial navigation. Here, we provide the first direct functional evidence for the existence of such input to the L2 cells. Secondly, the characterization of the KARs on L3Ps is a step forward to understand the KAR-mediated synaptic transmission and its contribution towards neuronal synchrony and excitability in the mEC. Further, the identification of a novel mediator of excitability at the synapse, PRG-1, show a critical way in which neuronal networks are finely tuned. The balance between excitation and inhibition is needed to maintain the integrity of neuronal microcircuits.

In conclusion, my doctoral thesis makes a contribution towards understanding the functional microcircuitry in the medial entorhinal cortex and answers questions explaining the role of microcircuit-forming synapses in physiological and pathophysiological conditions.

APPENDICES:

MATERIALS AND METHODS

A. Mapping neuronal microcircuitry

Commercially available hardware components

This section introduces the basic components of the setup, which are schematically illustrated in figure 3-05A. As proposed by Katz and Dalva (1994), a laser beam is focused and positioned within the specimen by using the objective of a standard upright microscope. Light was delivered to an Olympus BX-51 WI microscope (Olympus, Hamburg, Germany) with a 200 µm fiber optic light guide coupled into the epifluorescence port of the microscope with an OSI-BX adapter (Rapp Optoelektronik, Wedel, Germany) and focused on the specimen by the objective lens.

The final spot size within the tissue is determined by the magnification factor and the numerical aperture of the objective lens. We used a 0.9NA 60× objective, which yielded an optical spot size of about 7.5 µm. By using a fiber diameter of 20 µm it is possible to reach spot sizes as small as about 1–2.5 µm. As a light source, we use a modified DPSS laser System (Rapp Optoelectronics, Wedel, Germany). The power of the pulsed UV laser (355 nm wavelength, frequency-tripled Nd:YVO 4, 100 kHz pulse repetition rate; DPSS Lasers, Santa Clara, CA, USA) was adjusted by modulating the number of laser pulses in discrete stimulus intensity levels. The duration of the 2 ms light stimulus was controlled by a fast galvanometric driven shutter system triggered via a digital TTL-impulse generated by a computer-internal PCI-I/O card (Multifunction-Data-Aquisition NI-PCI-6221, Shielded Connector Block NIBNC-2110, National Instruments, Austin, TX, USA).

The microscope optics and, hence, the laser spot is positioned by amotorized XYZ-shifting table (Shifting Table 380, Luigs & Neumann, Ratingen, Germany), so that the specimen and the recording electrode remain in a fixed position. Each axis of the shifting table is equipped with a high-precision step motor that realizes a step size of 0.1 µm. The mutual communication between the XYZ-stage and the computer is realized by using a serial port and an external interface (Shifting Table Control Unit, Luigs & Neumann, Ratingen, Germany) between the computer and the motors.

For the optical control of the experiment a VX55 IR-camera (Till Photonics, Munich, Germany) is mounted on a standard C-mount port. The camera generates an analog video signal in the CCIR/PAL format, which is read out by a computer-internal frame-grabber card (DT-3120, Data Translation, Bietigheim Bissingen, Germany) and displayed in real-time using the Direct-Memory-Access mode of the computer-internal video card. The

communication software (on the operating system Windows) was hosted on a standard personal computer with a 1.2 GHz Pentium processor and 1 GB of RAM.

Slice preparation

Animal husbandry and experimental intervention were performed according to the german animal welfare act and the European Council Directive 86/609/EEC regarding the protection of animals used for experimental and other scientific purposes. All animal maintenance were performed in accordance with the guidelines of local authorities, Berlin [T 0100/03]). Wistar rats (2–3 weeks) were used for this study. The animals were anaesthetized with isoflurane, decapitated and brains were rapidly removed and placed in ice-cold (4°C) oxygenated artificial cerebrospinal fluid (ACSF) containing (in mM): NaCl (87), NaHCO3 (26), Sucrose (75), Glucose (25), KCl (2.4), NaH2PO4 (1.25), MgCl2 (7), and CaCl2 (0.5), pH 7.4. Horizontal, combined entorhinal-hippocampal brain slices (300µm; 400µm for oscillation experiments) were cut by Leica VT 1200 Vibratome (Leica Microsystems, Wetzlar, Germany). Slices were then incubated at 34-35°C for 30 minutes and thereafter transferred to ACSF containing (in mM): NaCl (119), NaHCO3 (26), Glucose (10), KCl (2.5), NaH2PO4 (1.25), MgCl2 (1.3), and CaCl2 (2.5), at room temperature. All ACSF solutions were equilibrated with carbogen (95% O2 and 5% CO2).

Electrophysiological recordings

Prior to recording, slices were transferred to a submerged recording chamber (Luigs and Neumann, Ratingen, Germany) and perfused with oxygenated ACSF at room temperature, with a perfusion rate of 2.5 – 3.0 ml/min. Recording electrodes of 3-6 MΩ resistance were pulled from borosilicate glass capillaries (Harvard Apparatus, Kent, UK; 1.5mm OD) using a micropipette electrode puller (DMG Universal Puller). Biocytin (0.2%) was included (for a subset of recorded cells) in the patch pipette to assess the morphology and correct location of the recorded neurons following the experiments. For calibration experiments, patch electrodes were filled with (in mM): 135 K-gluconate, 20 KCl, 2 MgATP, 10 Hepes, 0.2 EGTA, 5 phosphocreatine, pH 7.3. For mapping experiments, the intracellular solution consisted of (inmM):150K-gluconate, 0.5 MgCl2, 1.1EGTA, 10 phosphocreatine, pH 7.2. Whole-cell voltage and current-clamp recordings were performed with an Axopatch 700B Amplifier (Axon Instruments, Foster City, CA, USA). Initial access resistances were below 25 MΩ after breakthrough and not allowed to vary more than 30% during the course of the experiment in the voltage clamp mode. No access resistance compensation was used. Data were digitized

(National Instruments BNC-2090, Austin, TX, USA) at 5 kHz, lowpass filtered at 2 kHz and recorded stimulation point-specific with custom-made software.

Morphological reconstruction

Slices with 0.2% biocytin-filled cells were fixed in 0.1 mM phosphate buffer (pH 7.4) containing 4% paraformaldehyde, for 24–48 h. The filled neurones were visualized by incubating sections in avidin–biotin conjugated horseradish peroxidase (ABC, Vector Laboratories, Ltd., UK) and reacting them with diaminobenzidine and hydrogen peroxide. Sections were then dehydrated and embedded on glass slides. Subsequently, the cells were reconstructed with the aid of a Neurolucida reconstruction system (MicroBrightField, Inc., Williston, VT, USA).

Photostimulation – glutamate uncaging

20 ml of 200 μM MNI-caged-l-glutamate (Tocris, Bristol, UK) were recirculated at 3–5 ml/min. The maximum time period of recirculation was 3 h. The duration of the laser flash was 2 ms, the laser power under the objective corresponding to the stimulus intensity levels used was calibrated using a photo diode array based photodetector (PDA-K-60, Rapp Optoelectronics, Wedel, Germany) and monitored to exclude changes of stimulation light intensity over time. The readout of the detector was a voltage signal related to a single pulse and the number of pulses at a defined stimulation intensity level ranging from 0 to 10. For controlling against fluctuations in the laser intensity used in the experiments, it was not necessary to transform the voltage signal into an energy density measure.

Using a fluorescent coverslip with a black grid pattern, the focal plain for imaging the grid with the DIC-optics was aligned with the focal point of maximal laser intensity. In addition, the laser beam was defined as the center of the image. To ensure optimal spatial resolution of the laser beam and compensate for misalignment of the optical pathway, this procedure was repeated at the beginning of each experimental day. The optical system was adapted to achieve an effective light spot diameter of 15 μm in the focal plane. The effective spot size was ascertained by the direct activation of dendritic parts of a neuron.

The relatively large effective spot size was necessary to permit for scanning of large brain regions. If a higher resolution is required, smaller diameter light guides can be used. The focal plane of the stimulation was focused at 50 μm below the slice surface. Depending on the slice preparation, the slice surface may not be completely flat (Koetter et al., 2005). Variations in the Z-plane of the slice surface were analyzed using the integrated readout of the Z-

coordinates from the control software. Usually, the slice surface covered the whole layer II of the entorhinal cortex, in our preparation nonstationarities in the surface of the slice only occurred between different layers in horizontal entorhinal cortex slices. The patch pipette was positioned orthogonal to and directed away from the slice surface to minimize mechanical obstruction of the objective lens during mapping.

Generally, stimulation points were defined in a hexagonal grid with a raster size of 30 µm. The benefit of using a hexagonal grid instead of a rectangle pattern is that each point is surrounded by six equidistant neighboring points, which results in the highest density of scanning points for a given distance (Marsal, 1976). The inter-stimulus time between two consecutive points was longer than 2 s, a parameter that can be easily reduced to 1 s if larger areas have to be scanned. In order to prevent accumulation of uncaged glutamate, the stimulation order is automatically redefined to preserve a minimum distance of 60 µm between consecutive stimulation points.

Data analysis

The excitatory and inhibitory postsynaptic currents (EPSCs and IPSCs, respectively) are detected by an iterative algorithm. The detection algorithm is based on four criteria including the absolute peak amplitude (larger than 10 pA), the maximum absolute slope of the rising part of the PSC (faster than 2.8 pA/ms), the time-interval between the initiation of the PSC and its peak (shorter than 13 ms) and the total amount of electric charge that is transported out of the cell (negative for EPSCs and positive for IPSCs). To check the last criterion the integral between the trajectory of the PSCs and the baseline of the signal was calculated. The baseline is assessed iteratively by subtracting the detected PSC. The mean of the remaining signal defines the baseline for the next iteration step. The iterative algorithm stops if no more changes of the detected PSCs occur. In order to improve the performance of detection, the recorded signal is initially zero-phase digital filtered with a fifth-order lowpass Butterworth filter at a cutoff frequency of 500 Hz (see for unfiltered detection, e.g., Kudoh and Taguchi, 2002). Additionally, small fluctuations in the trajectory are substituted by an interpolating cubic hermite spline between starting and end point of the fluctuation resulting in a smoother version of the original trajectory. The slopes at starting and end point are chosen such that the interpolation preserves the shape of the original data and thus also the local extrema. The detection criteria were designed and adjusted to reliably detect visually identified putative PSCs. By construction and contrary to a template-based algorithms (e.g., Clements and Bekkers, 1997), the algorithm also detects indirect signals that are superimposed on direct

signals. However, the reliable detection of abnormal shaped PSCs or mixed signals composed of simultaneously arriving PSCs of different polarity remains critical for both the automatic and manual detection.

B. Cell-type specific and modular organization of microcircuitry

Slice preparation and electrophysiological recordings

Please refer to Appendix A.

.

Photostrimulation - glutamate uncaging

The setup and experimental procedures for photolysis of caged glutamate have been described previously (Bendels*, Beed* et al., 2008). In brief, 20 ml of 200 µM MNI-caged-l-glutamate (Tocris, Bristol, UK) were recirculated at 3–5 ml/min. The maximum time period of recirculation was 3 h. The duration of the laser flash was 2ms, the laser power under the objective corresponding to the stimulus intensity levels used was calibrated and constantly monitored using a photo diode array based photodetector (PDA-K-60, Rapp Optoelectronics, Wedel, Germany). The optical system was adapted to achieve an effective light spot diameter of 15 µm in the focal plane. Generally, stimulation points were defined in a hexagonal grid with a raster size of 30 µm. For all experiments, the focal depth of the uncaging spot was set at 50 µm below the slice surface. To correct for differences in focal depth of the uncaging spot due to variabilities in slice surface height, the focal depth was adjusted for different subregions. These subregions were scanned in a randomized order.

Histological procedures

Please refer to Appendix A.

Analysis and statistics

For detection of synaptic events, we used the automatic detection method described by Bendels*, Beed* et al. 2008. Parameters used for automatic detection were based on visual inspection of the raw data. The time window used for the detection of direct synaptic inputs was based on experiments blocking indirect synaptic inputs with TTX. The PSC rate of all experiments was plotted over time and the duration of a photostimulation-induced significant increase in the PSC rate defined the time interval for the detection of indirect synaptic events. See Bendels et al., 2009 for a description of the algorithm used for the separation of specific events constituting hotspots from background noise. Statistical tests were performed using student's t-test. All data are written as mean ± SEM.

C. Neuronal synchrony and excitability

Slice preparation

Animal husbandry laws and animal welfare acts were followed as explained in Appendix A. In addition to Wistar rats, C57/BL6 mice (2–3 weeks) were also used for this study. The GluK1 and GluK2 mice used in this study were raised on a C57/BL6 background and littermate wildtype mice were used as control in such experiments. The slice preparation procedure in explained elsewhere (Appendix A). In addition to incubation of slices at room temperature, those used for oscillation experiments were stored in an interface-type recording chamber.

Electrophysiological recordings

Standard electrophysiological recordings procedures were followed as explained in Appendix A. The internal solution for all recordings included (in mM): K-gluconate (135), Hepes (10.0), EGTA (0.5), KCl (20), MgATP (2.0) and Phosphocreatine (5.0), with the exception of IV characterization, which included Cs-gluconate (140), Hepes (10.0), EGTA (1.0), CaCl2 (0.5), and Glucose (10.0).The osmolarities for the internal solutions were 300-305 mOsm, and the pH was adjusted to 7.2-7.3 with KOH or CsOH.

L3Ps were initially recorded in the current-clamp mode to identify them according to their characteristic electroresponsive properties. Identified neurons were then held at -60 mV in voltage-clamp mode, and only recordings from neurons whose series resistances < 30MΩ were used for data analysis. The whole-cell holding current experiments were done in the absence of any receptor-blockers unless mentioned otherwise on the figures.

Excitatory postsynaptic currents (EPSCs) were evoked by stimulating the L1 mEC. Synaptic KARs: Evoked EPSCs were recorded until the amplitudes of the responses were stable for a minimum of ten minutes before control and experimental drug application responses were obtained for analysis. EPSCKA were pharmacologically isolated by adding 50 μM D(-)-2-amino-5-phosphonopentanoic acid (APV), 2 μM Gabazine (SR 95531), 20 μM SCH 50911, (Tocris, Ellisville, MO, USA), and 20 μM 1-(4-aminophenyl)-4-methyl-7,8-methylenedioxy-5H-2,3-benzodiazepine hydrochloride (GYKI 53655) to inhibit NMDA, GABA-A, GABA-B, and AMPA receptors respectively. GYKI resistant EPSCs were blocked by adding 25 μM 2,3-dioxo-6-nitro-1,2,3,4-tetrahydrobenzo(f)quinoxaline-7-sulfonamide (NBQX). A minimum of ten responses were recorded under each condition and averaged for analysis. Evoked EPSC

amplitudes were calculated as the difference between the averaged peak response and the average of the baseline region (20 ms preceding the stimulus).

For studying gamma oscillations, slices were stored and recorded from in the interface-type recording chamber. Extracellular recording electrode was placed in the superficial layers of mEC and baseline activity was recorded. Gamma oscillations were induced by bath applying 300 nM Kainic acid for upto 40 minutes.

Photostimulation - glutamate uncaging

With the uncaging procedure explained in Appendix A, glutamate was uncaged over the cell soma in the presence of all other channel blockers as mentioned above. In combined experiments where both the somatic and synaptic currents were recorded, first L1 mEC was stimulated with a stimulation electrode thus evoking a synaptic response and after 200-300 ms a laser pulse was flashed to uncage MNI-glutamate evoking somatic current.

Histological procedures

A subset of electrophysiologically characterized L3Ps were loaded with 0.2% biocytin and reconstructed for visualization as described in Appendix A.

Analysis and statistics

All values in all graphs are presented as mean ± SEM. Analyses were performed using IGOR Pro (WaveMetrics Inc., OR, USA), SigmaPlot (SYSTAT, Hounslow, UK) and MATLAB v7.0 (The Mathworks Inc., MA, USA). Statistical comparisons between groups were performed with Student's t-test. Results were considered significant at $p < 0.05$ or $p < 0.01$ (*).

Drugs

Kainic acid, (Kainate, KA); 1-(4-aminophenyl)-4-methyl-7,8-methylenedioxy-5H-2,3-benzodiazepine hydrochloride (GYKI 53655, henceforth in the manuscript GYKI would refer to GYKI 53655 unless mentioned otherwise); D(-)-2-amino-5-phosphonopentanoic acid (APV); 6-Imino-3-(4-methoxyphenyl)-1(6H)-pyridazinebutanoic acid hydrobromide (Gabazine); (2S)-(+)-5,5-Dimethyl-2-morpholineacetic acid (SCH 50911); 2,3-dioxo-6-nitro-1,2,3,4-tetrahydrobenzo(f)quinoxaline-7-sulfonamide (NBQX) and 6-Chloro-3,4-dihydro-3-(5-norbornen-2-yl)-2H-1,2,4-benzothiazidiazine-7-sulfonamide-1,1-dioxide (Cyclothiazide, CTZ) were all purchased from Tocris Bioscience (Ellisville, MO, USA).

REFERENCES

Aaron G, Yuste R (2006) Reverse optical probing (ROPING) of neocortical circuits. *Synapse* 60:437–440.

Agmon A, Connors BW (1991) Thalamocortical responses of mouse somatosensory (barrel) cortex in vitro. *Neuroscience* 41:365–379.

Alle H, Geiger JR (2006) Combined analog and action potential coding in hippocampal mossy fibers. *Science* 311:1290–1293.

Alonso A, Klink R (1993) Differential electroresponsiveness of stellate and pyramidal-like cells of medial entorhinal cortex layer II. *J Neurophysiol* 70:128-143.

Amaral DG, Witter MP (1989) The three-dimensional organization of the hippocampal formation: a review of anatomical data. *Neuroscience* 31:571–591.

Arenkiel BR, Peca J, Davison IG, Feliciano C, Deisseroth K, Augustine GJ, Ehlers MD, Feng G (2007) In vivo light-induced activation of neural circuitry in transgenic mice expressing channelrhodopsin-2. *Neuron* 54:205–218.

Arenkiel BR, Ehlers MD (2009) Molecular genetics and imaging technologies for circuit-based neuroanatomy. *Nature* (Insight Review) 461:900-907.

Bahn S, Volk B, Wisden W (1994) Kainate Receptor Gene-Expression in the Developing Rat-Brain. *Journal of Neuroscience* 14: 5525-5547.

Bartesaghi R, Gessi T, Sperti L (1988) Electrophysiological analysis of the dorsal hippocampal commissure projections to the entorhinal area. *Neuroscience* 26:55–67.

Bartesaghi R, Gessi T, Sperti L (1989) Electrophysiological analysis of the hippocampal projections to the entorhinal area. *Neuroscience* 30:51–62.

Bartesaghi R, Di Maio V, Gessi T (2005) Topographic activation of the medial entorhinal cortex by presubicular commissural projections. *The Journal of Comparative Neurology* 487:283–299.

Bear J, Fountain NB, Lothman EW (1996) Responses of the superficial entorhinal cortex in vitro in slices from naive and chronically epileptic rats. *J. Neurophysiol.* 76:2928-40.

Ben-Ari Y, Cossart R (2000) Kainate, a double agent that generates seizures: two decades of progress. *Trends Neurosci.* 23: 580-587.

Ben-Ari Y (2006) Basic developmental rules and their implications for epilepsy in the immature brain. *Epileptic Disord.* 8:91–102.

Ben-Ari Y, Gaiarsa JL, Tyzio R, Khazipov R (2007) GABA: a pioneer transmitter that excites immature neurons and generates primitive oscillations. *Physiol. Rev.* 87:1215–1284.

Ben-Ari Y (2008) Neuro-archaeology: pre-symptomatic architecture and signature of neurological disorders. *Trends Neurosci.* 23:580-587.

Bendels MH, Beed P, Leibold C, Schmitz D, Johenning FW (2008) A novel control software that improves the experimental workflow of scanning photostimulation experiments. *J Neurosci Methods* 175:44-57.

Borlotto ZA, Nistico R, More JC, Jane DE, Collingridge GR (2005) Kainate receptors and mossy fiber LTP. *Neurotoxicology* 25: 769-777.

Bostock E, Muller RU, Kubie JL (1991). Experience-dependent modifications of hippocampal place cell firing. *Hippocampus* 1:193-205.

Briggs F, Callaway EM (2005) Laminar patterns of local excitatory input to layer 5 neurons in macaque primary visual cortex. *Cereb Cortex* 15:479–488.

Brindley DN (2004) Lipid phosphate phosphatases and related proteins: signaling functions in development, cell division, and cancer. *J. Cell. Biochem.* 92:900–912.

Brivanlou IH, Dantzker JL, Stevens CF, Callaway EM (2004) Topographic specificity of functional connections from hippocampal CA3 to CA1. *Proc Natl Acad Sci USA* 101:2560–2565.

Brun VH, Otnass MK, Molden S, Steffenach HA, Witter MP, Moser MB, Moser EI (2002) Place cells and place recognition maintained by direct entorhinal-hippocampal circuitry. *Science* 296:2243-2246.

Brusa R, Zimmermann F, Koh DS, Feldmeyer D, Gass P, et al. (1995) Early-Onset Epilepsy and Postnatal Lethality Associated with An Editing-Deficient Glur-B Allele in Mice. *Science* 270: 1677-1680.

Bureau I, von Saint Paul F, Svoboda K (2006) Interdigitated paralemniscal and lemniscal pathways in the mouse barrel cortex. *PLoS Biol* 4:e382.

Bureau I, Shepherd GM, Svoboda K (2008) Circuit and plasticity defects in the developing somatosensory cortex of FMR1 knock-out mice. *J Neurosci* 28:5178–5188.

Cajal SRY (1911) Histologie du Système Nerveux de l'Homme et des Vertébrés, Maloine, Paris, France.

Callaway EM, Katz LC (1993) Photostimulation using caged glutamate reveals functional circuitry in living brain slices. *Proc Natl Acad Sci USA* 90:7661-7665.

Callaway EM, Yuste R (2002) Stimulating neurons with light. *Curr Opin Neurobiol* 12:587–592.

Canto CB, Wouterlood FG, Witter MP (2008) What does the anatomical organization of the entorhinal cortex tell us? *Neural Plast* 2008:381243.

Castillo PE, Malenka RC, Nicoll RA (1997) Kainate receptors mediate a slow postsynaptic current in hippocampal CA3 neurons. *Nature* 388:182-186.

Chittajallu R, Braithwaite SP, Clarke VRJ, Henley JM (1999) Kainate receptors: subunits, synaptic localization and function. *Trends in Pharmacological Sciences* 20: 26-35.

Clements JD, Bekkers JM (1997) Detection of spontaneous synaptic events with an optimally scaled template. *Biophys J* 73:220–229.

Collingridge GL, Olsen RW, Peters J, Spedding M (2009) A nomenclature for ligand-gated ion channels. *Neuropharmacology* 56:2–5.

Contos JJ, Chun J (2000) Genomic characterization of the lysophosphatidic acid receptor gene, lp(A2)/Edg4, and identification of a frameshift mutation in a previously characterized cDNA. *Genomics* 64:155–169.

Contos JJ, Ishii I, Chun J (2000) Lysophosphatidic acid receptors. *Mol. Pharmacol.* 58:1188–1196.

Crepel V, et al. (2007) A parturition-associated nonsynaptic coherent activity pattern in the developing hippocampus. *Neuron* 54:105–120.

Cunningham MO, Davies CH, Buhl EH, Kopell N, Whittington MA (2003) Gamma oscillations induced by kainate receptor activation in the entorhinal cortex in vitro. *Journal of Neuroscience* 23: 9761-9769.

Cunningham MO, Hunt J, Middleton S, Lebeau FEN, Gillies MG, et al. (2006) Region-specific reduction in entorhinal gamma oscillations and parvalbumin-immunoreactive neurons in animal models of psychiatric illness. *Journal of Neuroscience* 26: 2767-2776.
Dalva MB, Katz LC (1994) Rearrangements of synaptic connections in visual cortex revealed by laser photostimulation. *Science* 265:255-258.

Dantzker JL, Callaway EM (2000) Laminar sources of synaptic input to cortical inhibitory interneurons and pyramidal neurons. *Nat Neurosci* 3:701–707.

DeFelipe J (1993) Neocortical neuronal diversity: chemical heterogeneity revealed by colocalization studies of classic neurotransmitters, neuropeptides, calcium-binding proteins, and cell surface molecules. *Cereb. Cortex* 3:273–289

Dekaban AS (1978) Changes in brain weights during the span of human life: relation of brain weights to body heights and body weights. *Ann Neurol* 4:345–356.

Dhillon A, Jones RS (2000) Laminar differences in recurrent excitatory transmission in the rat entorhinal cortex in vitro. *Neuroscience* 99:413-422.

Dickson CT, Mena AR, Alonso A (1997) Electroresponsiveness of medial entorhinal cortex layer III neurons in vitro. *Neuroscience* 81:937-950.

Dickson CT, Magistretti J, Shalinsky M, Hamam B, Alonso A (2000) Oscillatory activity in entorhinal neurons and circuits - Mechanisms and function. *Parahippocampal Region* 911: 127-150.

Dodt HU, Frick A, Kampe K, ZieglgansbergerW (1998) NMDA and AMPA receptors on neocortical neurons are differentially distributed. *Eur J Neurosci* 10:3351–3357.

Dolorfo CL, Amaral DG (1998) Entorhinal cortex of the rat: organization of intrinsic connections. *The Journal of Comparative Neurology* 398:49–82.

Eder M, Becker K, Rammes G, Schierloh A, Azad SC et al. (2003) Distribution and properties of functional postsynaptic kainate receptors on neocortical layer V pyramidal neurons. *Journal of Neuroscience* 23:6660-6670.

Fairen A, et al. (1984) Nonpyramidal neurons: general account. In Cerebral Cortex (Vol. 1): Cellular Components of the Cerebral Cortex (Peters A and Jones EG, eds), Plenum Press

Feldmeyer D, Egger V, Lubke J, Sakmann B (1999) Reliable synaptic connections between pairs of excitatory layer 4 neurones within a single 'barrel' of developing rat somatosensory cortex. *J. Physiol.* 521:169–190.

Fell J, Klaver P, Lehnertz K, Grunwald T, Schaller C, Elger CE, Fernandez G (2001) Human memory formation is accompanied by rhinal-hippocampal coupling and decoupling. *Nat Neuroscience* 4:1259–1264.

Fernandez G, Effern A, Grunwald T, Pezer N, Lehnertz K, Dumpelmann M, Van Roost D, Elger CE (1999) Real-time tracking of memory formation in the human rhinal cortex and hippocampus. *Science* 285:1582–1585.

Fisahn A (2005) Kainate receptors and rhythmic activity in neuronal networks: hippocampal gamma oscillations as a tool. *Journal of Physiology-London* 562:65-72.

Frerking M, Ohligre-Frerking P (2002) AMPA receptors and kainate receptors encode different features of afferent activity. *Journal of Neuroscience* 22:7434-7443.

Frick A, Zieglgansberger W, Dodt HU (2001) Glutamate receptors form hot spots on apical dendrites of neocortical pyramidal neurons. *J Neurophysiol* 86:1412–1421.

Fukushima N, Chun J (2001) The LPA receptors. *Prostaglandins Other Lipid Mediat.* 64:21–32.

Germroth P, Schwerdtfeger WK, Buhl EH (1989) Morphology of identified entorhinal neurons projecting to the hippocampus. A light microscopical study combining retrograde tracing and intracellular injection. *Neuroscience* 30:683–691.

Giocomo LM, Zilli EA, Fransen E, Hasselmo ME (2007) Temporal frequency of subthreshold oscillations scales with entorhinal grid cell field spacing. *Science* 315:1719-1722.

Gloveli T, Schmitz D, Empson RM, Dugladze T, Heinemann U (1997a) Morphological and electrophysiological characterization of layer III cells of the medial entorhinal cortex of the rat. *Neuroscience* 77:629-648.

Gloveli T, Schmitz D, Empson RM, Heinemann U (1997b) Frequency-dependent information flow from the entorhinal cortex to the hippocampus. *J. Neurophysiol* 78: 3444-3449.

Godwin DW, Che D, O'Malley DM, Zhou Q (1997) Photostimulation with caged neurotransmitters using fiber optic lightguides. *J Neurosci Methods* 73:91–106.

Grigorenko EV, Bell WL, Glazier S, Pons T, Deadwyler S (1998) Editing status at the Q/R site of the GluR2 and GluR6 glutamate receptor subunits in the surgically excised hippocampus of patients with refractory epilepsy. *Neuroreport* 9: 2219-2224.

Grillner S, Markram H, De Schutter E, Silberberg, G, LeBeau FE (2005) Microcircuits in action--from CPGs to neocortex. *Trends Neurosci* 28:525-533.

Gupta A, Wang Y, Markram H (2000) Organizing principles for a diversity of GABAergic interneurons and synapses in the neocortex. *Science* 287:273–278.

Hafting T, Fyhn M, Molden S, Moser MB, Moser EI (2005) Microstructure of a spatial map in the entorhinal cortex. *Nature* 436:801-806.

Hamam BN, Kennedy TE, Alonso AA, Amaral DG (2000) Morphological and electrophysiological characteristics of layer V neurons of the rat medial entorhinal cortex. *The Journal of Comparative Neurology* 418:457–472.

Hamam BN, Amaral DG, Alonso AA (2002) Morphological and electrophysiological characteristics of layer V neurons of the rat lateral entorhinal cortex. *The Journal of Comparative Neurology* 451:45–61.

Han X, Boyden ES (2007) Multiple-color optical activation, silencing, and desynchronization of neural activity, with single-spike temporal resolution. *PLoS One* 21, 2:e299.

Hermansson M, Käkelä R, Berghall M, Lehesjoki AE, Somerharju P, Lahtinen U (2005) Mass spectrometric analysis reveals changes in phospholipid, neutral sphingolipid and sulfatide molecular species in progressive epilepsy with mental retardation, EPMR, brain, a case study. *J. Neurochem.* 95**:**609–617.

Higuchi M, Stefan M, Single FN, Hartner J, Rozov A, et al. (2000) Point mutation in an AMPA receptor gene rescues lethality in mice deficient in the RNA-editing enzyme ADAR2. *Nature* 406:78-81.

Hollmann, M, Heinemann, S (1994) Cloned glutamate receptors. *Annual Review Neuroscience* 17:31–108.

Huettner JE (2003) Kainate receptors and synaptic transmission. *Progress in Neurobiology* 70: 387-407.

Huxter JR, Zinyuk LE, Roloff EVL, Clarke VRJ, Dolman NP, et al. (2007) Inhibition of kainate receptors reduces the frequency of hippocampal theta oscillations. *Journal of Neuroscience* 27:2212-2223.

Iijima T, Witter MP, Ichikawa M, Tominaga T, Kajiwara R, Matsumoto G (1996) Entorhinal-hippocampal interactions revealed by real-time imaging. *Science* 272:1176-1179.

Jane D, Lodge D, Collingridge GL (2009) Kainate receptors: Pharmacology, function and therapeutic potential. *Neuropharmacology* 56:90–113.

Jarrard LE, Meldrum BS (1993) Selective Excitotoxic Pathology in the Rat Hippocampus. *Neuropathology and Applied Neurobiology* 19:381-389.

Jin X, Prince DA, Huguenard JR (2006) Enhanced excitatory synaptic connectivity in layer V pyramidal neurons of chronically injured epileptogenic neocortex in rats. *J Neurosci* 26:4891–4900.

Johnson DM, Illig KR, Behan M, Haberly LB (2000) New features of connectivity in piriform cortex visualized by intracellular injection of pyramidal cells suggest that "primary" olfactory cortex functions like "association" cortex in other sensory systems. *J Neurosci* 20:6974-6982.

Jones RSG (1994) Synaptic and intrinsic properties of neurons of origin of the perforant path in layer II of the rat entorhinal cortex in vitro. *Hippocampus* 4:335–353.

Kandel ER, Schwartz JH, Sanes JR (2000) Sensory experience and the fine-tuning of synaptic connections. In:

Kandel ER, Schwartz JH, Jessell TM (eds). *Principles of Neural Science*, 4th edn. Appleton & Lange (Stamford, Conn):1115–1130.

Kandler K, Katz LC, Kauer JA (1998) Focal photolysis of caged glutamate produces long term depression of hippocampal glutamate receptors. *Nat Neurosci* 1:119–123.

Katz LC, Dalva MB (1994) Scanning laser photostimulation: a new approach for analyzing brain circuits. *J Neurosci Methods* 54:205–18.

Kawaguchi Y, Kubota Y (1997) GABAergic cell subtypes and their synaptic connections in rat frontal cortex. *Cereb. Cortex* 7:476–486

Klink R, Alonso A (1997) Morphological characteristics of layer II projection neurons in the rat medial entorhinal cortex. *Hippocampus* 7:571-583.

Kloosterman F, Van Haeften T, Witter MP, Lopes Da Silva FH (2003) Electrophysiological characterization of interlaminar entorhinal connections: an essential link for re-entrance in the hippocampal-entorhinal system. *Eur J Neurosci* 18:3037-3052.

Knickmeyer RC, Gouttard S, Kang C, Evans D, Wilber K, et al. (2008) A structural MRI study of human brain development from birth to 2 years. *J Neurosci* 28:12176–12182.

Koetter R, Schubert D, Dyhrfjeld-Johnsen J, Luhmann HJ, Staiger JF (2005) Optical release of caged glutamate for stimulation of neurons in the in vitro slice preparation. *J Biomed Opt* 10:11003.

Koehler C (1986) Intrinsic connections of the retrohippocampal region in the rat brain. II. The medial entorhinal area. *J Comp Neurol* 246:149-169.

Koehler C (1988) Intrinsic connections of the retrohippocampal region in the rat brain. III. The lateral entorhinal area. *J Comp Neurol* 271:208–228.

Kortenbruck G, Berger E, Speckmann EJ, Musshoff U (2001) RNA editing at the Q/R site for the glutamate receptor subunits GluR2, GluR5, and GluR6 in hippocampus and temporal cortex from epileptic patients. *Neurobiology of Disease* 8: 459-468.

Kudoh SN, Taguchi T (2002) A simple exploratory algorithm for the accurate and fast detection of spontaneous synaptic events. *Biosens Bioelectron* 17:773–82.

Kumar SS, Buckmaster PS (2006) Hyperexcitability, interneurons, and loss of GABAergic synapses in entorhinal cortex in a model of temporal lobe epilepsy. *J Neurosci* 26: 4613–4623.

Kumar SS, Jin X, Buckmaster PS, Huguenard JR (2007) Recurrent circuits in layer II of medial entorhinal cortex in a model of temporal lobe epilepsy. *J Neurosci* 27:1239-1246.

Lam Y-W, Nelson CS, Sherman SM (2006) Mapping of the functional interconnections between thalamic reticular neurons using photostimulation. *J Neurophysiol* 96:2593–2600.

Lerma J (2006) Kainate receptor physiology. *Curr.Opin.Pharmacol.* 6: 89-97.

Lester HA, Nerbonne JM (1982) Physiological and pharmacological manipulations with light flashes. *Annu Rev Biophys Bioeng* 11:151–75.

Lodge D (2009) The history of the pharmacology and cloning of ionotropic glutamate receptors and the development of idiosyncratic nomenclature. *Neuropharmacology* 56:6–21.

Losonczy A, Magee JC (2006) Integrative properties of radial oblique dendrites in hippocampal CA1 pyramidal neurons. *Neuron* 50:291–307.

Liu QS, Xu QW, Arcuino G, Kang J, Nedergaard M (2004) Astrocyte-mediated activation of neuronal kainate receptors. *Proc Natl Acad Sci USA* 101:3172-3177.

Lomeli H, Wisden W, Kohler M, Keinanen K, Sommer B, et al. (1992) High-Affinity Kainate and Domoate Receptors in Rat-Brain. *FEBS Letters* 307:139-143.

MacGregor DG, Graham DI, Stone TW (1997) The attenuation of kainate-induced neurotoxicity by chlormethiazole and its enhancement by dizocilpine, muscimol, and adenosine receptor agonists. *Experimental Neurology* 148:110-123.

MacLennan AJ, Carney PR, Zhu WJ, Chaves AH, Garcia J, Grimes JR, Anderson KJ, Roper SN, Lee N (2001) An essential role for the H218/AGR16/Edg-5/LP(B2) sphingosine 1-phosphate receptor in neuronal excitability. *Eur. J. Neurosci.* 14:203–209.

Marsal D (1976) Die numerische Lösung partieller Differentialgleichungen in Wissenschaft und Technik. Mannheim, Germany: Bibliographisches Institut.

Matsuzaki M, Honkura N, Ellis-Davies GC, Kasai H (2004) Structural basis of long-term potentiation in single dendritic spines. Nature 429:761–766.

McNaughton BL, Barnes CA, Gerrard JL, Gothard K, Jung MW, et al. (1996) Deciphering the hippocampal polyglot: the hippocampus as a path integration system. *J. Exp. Biol.* 199:173-185.

McNaughton BL, Battaglia FP, Jensen O, Moser EI, Moser MB (2006) Path integration and the neural basis of the 'cognitive map'. *Nat Rev Neurosci* 7:663-678.

Motazacker MM, Rost BR, Hucho T, Garshasbi M, Kahrizi K, et al. (2007) A defect in the ionotropic glutamate receptor 6 gene (GRIK2) is associated with autosomal recessive mental retardation. *American Journal of Human Genetics* 81:792-798.

Mountcastle VB (1997). The columnar organization of the neocortex. *Brain* 120:701-722.

Mountcastle VB (1998) Perceptual Neuroscience: The Cerebral Cortex, Harvard Uni. Press

Mulle C, Sailer A, Perez-Otano I, Dickinson-Anson H, Castillo PE, et al. (1998) Altered synaptic physiology and reduced susceptibility to kainate-induced seizures in GluR6-deficient mice. *Nature* 392:601-605.

Mulle C, Sailer A, Swanson GT, Brana C, O'Gorman S, et al. (2000) Subunit composition of kainate receptors in hippocampal interneurons. *Neuron* 28:475-484.

Musshoff U, Kortenbruck G, Vollmar W, Berger E, Speckmann EJ (2002) Postoperative investigations in epilepsy surgery: Molecularbiological analyses. *Klinische Neurophysiologie* 32:178-187.

Nikolenko V, Poskanzer KE, Yuste R (2007) Two-photon photostimulation and imaging of neural circuits. *Nat Methods* 4:943–50.

Okamoto K, Nagai T, Miyawaki A, Hayashi Y (2004) Rapid and persistent modulation of actin dynamics regulates postsynaptic reorganization underlying bidirectional plasticity, *Nat. Neurosci.* 7:1104–1112.

O'Keefe J, Dostrovsky J (1971) The hippocampus as a spatial map. Preliminary evidence from unit activity in the freely-moving rat. *Brain Res.* 34:171-175

O'Keefe J (1976). Place units in the hippocampus of the freely moving rat. *Exp. Neurol.* 51:78-109.

O'Keefe J, Nadel L (1978) The Hippocampus as a Cognitive Map. Oxford: Clarendon Press.

Pan CY, Wu AZ, Chen YT (2007) Lysophospholipids regulate excitability and exocytosis in cultured bovine chromaffin cells. *J. Neurochem.* 102**:**944–956.

Paschen W, Schmitt J, Uto A (1996) RNA editing of glutamate receptor subunits GluR2, GluR5, and GluR6 in transient cerebral ischemia in the rat. *Journal of Cerebral Blood Flow and Metabolism* 16:548-556.

Peters A, Yilmaz E (1993) Neuronal organization in area 17 of cat visual cortex. *Cereb. Cortex* 3:49–68

Peterlin ZA, Kozloski J, Mao BQ, Tsiola A, Yuste R (2000) Optical probing of neuronal circuits with calcium indicators. *Proc. Natl. Acad. Sci. USA* 97:3619–3624.

Petreanu L, Huber D, Sobczyk A, Svoboda K (2007) Channelrhodopsin-2- assisted circuit mapping of long-range callosal projections. *Nat. Neurosci.* 10:663–668.

Pinheiro P, Mulle C (2006) Kainate receptors. *Cell Tissue Res.* 326:457-482.

Pouille F, Scanziani M (2001) Enforcement of temporal fidelity in pyramidal cells by somatic feed-forward inhibition. *Science* 293:1159–1163.

Renault AD, Sigal AJ, Morris AJ, Lehmann R (2004) Soma-germ line competition for lipid phosphate uptake regulates germ cell migration and survival, *Science* 305:1963–1966.

Saggau, P (2006) New methods and uses for fast optical scanning. *Current Opinion in Neurobiology* 16:543–550.

Sargolini F, Fyhn M, Hafting T, McNaughton BL, Witter MP, Moser MB, Moser EI (2006) Conjunctive representation of position, direction, and velocity in entorhinal cortex. *Science* 312:758-762.

Sailer A, Swanson GT, Perez-Otano I, O'Leary L, Malkmus SA et al. (1999) Generation and analysis of GluR5 (Q636R) kainate receptor mutant mice. *Journal of Neuroscience* 19:8757-8764.

Scanziani M, Häusser M (2009) Electrophysiology in the age of light. *Nature* (Insight Review) 461:930-939.

Scharfman HE, Goodman JH, Du F, Schwarcz R (1998) Chronic changes in synaptic responses of entorhinal and hippocampal neurons after amino-oxyacetic acid (AOAA)-induced entorhinal cortical neuron loss. *J. Neurophysiol.* 80:3031-3046.

Schmolke C, Kunzle H (1997) On the presence of dendrite bundles in the cerebral cortex of the Madagascan lesser hedgehog tenrec and the red-eared pond turtle. *Anat. Embryol. (Berl.)* 196:195–213

Schubert D, Staiger JF, Cho N, Kötter R, Zilles K, Luhmann HJ (2001) Layer-specific intracolumnar and transcolumnar functional connectivity of layer V pyramidal cells in rat barrel cortex. *Journal of Neuroscience* 21:3580–3592.

Schubert, D, Koetter, R, Zilles, K, Luhmann, HJ, Staiger JF (2003) Cell type-specific circuits of cortical layer IV spiny neurons. *Journal of Neuroscience* 23:2961-2970.

Schubert D, Koetter R, Luhmann HJ, Staiger JF (2006) Morphology, electrophysiology and functional input connectivity of pyramidal neurons characterizes a genuine layer Va in the primary somatosensory cortex. *Cereb Cortex* 16:223–36.

Schubert D, Koetter R, Staiger JF (2007) Mapping functional connectivity in barrel-related columns reveals layer- and cell type-specific microcircuits. *Brain Struct Funct.* 212:107–119.

Seeburg PH, Higuchi M, Sprengel R (1998) RNA editing of brain glutamate receptor channels: mechanism and physiology. *Brain Research Reviews* 26:217-229.

Seeburg PH, Hartner J (2003) Regulation of ion channel/neurotransmitter receptor function by RNA editing. *Current Opinion in Neurobiology* 13:279-283.

Shepherd GM, Pologruto TA, Svoboda K (2003) Circuit analysis of experience-dependent plasticity in the developing rat barrel cortex. *Neuron* 38:277-289.

Shoham S, O'Connor DH, Sarkisov DV, Wang SS-H (2005) Rapid neurotransmitter uncaging in spatially defined patterns. *Nat Methods* 2:837–43.

Sigal YJ, McDermott MI, Morris AJ (2005) Integral membrane lipid phosphatases / phosphotransferases: common structure and diverse functions. *Biochem. J.* 387:281–293.

Silberberg G, Gupta A, Markram H (2002) Stereotypy in neocortical microcircuits. *Trends Neurosci* 25:227-230.

Silberberg G, Grillner S, LeBeau FE, Maex R, Markram H (2005) Synaptic pathways in neural microcircuits. *Trends Neurosci* 28:541-551.

Sprengel R, Brusa R, Feldmeyer D, Burnashev N, Hvalby O, et al. (1998) RNA editing in the brain. Naunyn-Schmiedebergs Archives of Pharmacology 358: R370.

Starz-Gaiano M, Cho NK, Forbes A, Lehmann R (2001) Spatially restricted activity of a Drosophila lipid phosphatase guides migrating germ cells. *Development* 128:983–991.

Steriade M (2001) The Intact and Sliced Brain (Cambridge, MA, USA: MIT Press).

Steward O, Scoville SA (1976) Cells of origin of entorhinal cortical afferents to the hippocampus and fascia dentata of the rat. *J Comp Neurol* 169:347–370.

Taube JS, Muller RU, Ranck JB Jr (1990) Head-direction cells recorded from the postsubiculum in freely moving rats. I. Description and quantitative analysis. *J. Neurosci.* 10:420-435.

Thomson A, Lamy C (2007) Functional maps of neocortical local circuitry. *Frontiers in Neuroscience* 1:19-42

Todd AE, Orengo CA, Thornton JM (2002) Sequence and structural differences between enzyme and nonenzyme homologs. *Structure* 10:1435–1451.

Toledo-Rodriguez M, et al. (2002) Neocortex: basic neuron types. In The Handbook of Brain Theory and Neural Networks (2nd edn) (Arbib, M.A., ed.), MIT Press.

Toledo-Rodriguez M, et al. (2005) Cellular signaling properties in microcircuits. *Trends Neurosci* 28:534-540.

Tolle TR, Berthele A, Zieglgansberger W, Seeburg PH, Wisden W (1993) The Differential Expression of 16 NMDA and Non-NMDA Receptor Subunits in the Rat Spinal-Cord and in Periaqueductal Gray. *Journal of Neuroscience* 13:5009-5028.

Tolner EA, Kloosterman F, Kalitzin SN, da Silva FHL, Gorter TA (2005a) Physiological changes in chronic epileptic rats are prominent in superficial layers of the medial entorhinal area. *Epilepsia* 46:72-81.

Tolner EA, Kloosterman F, van Vliet EA, Witter MP, Lopes da Silva FH, Gorter JA (2005b) Presubiculum stimulation in vivo evokes distinct oscillations in superficial and deep entorhinal cortex layers in chronic epileptic rats. *The Journal of Neuroscience* 25:8755–8765.

Tolner EA, Frahm C, Metzger R, Gorter JA, Witte OW, et al. (2007) Synaptic responses in superficial layers of medical entorhinal cortex from rats with kainate-induced epilepsy. *Neurobiology of Disease* 26:419-438.

van Haeffen T, Baks-te-Bulte L, Goede PH, Wouterlood FG, Witter MP (2003) Morphological and numerical analysis of synaptic interactions between neurons in deep and superficial layers of the entorhinal cortex of the rat. *Hippocampus* 13:943–952.

Van Hoesen (1982) The parahippocampal gyrus. New observations regarding its coritcal connections in the monkey. *Trends Neurosci* 5:345–350.

Van Hoesen GW, Hyman BT, Damasio AR (1986) Cell-specific pathology in neural systems of the temporal lobe in Alzheimer's disease. *Prog Brain Res* 70:321–335.

Van Hoesen GW, Hyman BT, Damasio AR (1991) Entorhinal cortex pathology in Alzheimer's disease. *Hippocampus* 1:1–8.

Vignes M, Collingridge GL (1997) The synaptic activation of kainate receptors. *Nature* 388:179-182.

Vincent P, Mulle C (2009) Kainate receptors in epilepsy and excitotoxicity. Neuroscience 158:309-323

Vissel B, Royle GA, Christie BR, Schiffer HH, Ghetti A, et al. (2001) The role of RNA editing of kainate receptors in synaptic plasticity and seizures. *Neuron* 29:217-227.

Wang H, Peca J, Matsuzaki M, Matsuzaki, K., Noguchi J, et al. (2007) High-speed mapping of synaptic connectivity using photostimulation in Channelrhodopsin-2 transgenic mice. *Proc. Natl. Acad. Sci. USA* 104:8143–8148.

Watkins JC, Evans RH, (1981) Excitatory amino acid transmitters. *Annual Review of Pharmacology and Toxicology* 21:165–204.

Watkins JC, Jane DE (2006) The glutamate story. *British Journal of Pharmacology* 147:S100–S108.

Werner P, Voigt M, Keinanen K, Wisden W, Seeburg PH (1991) Cloning of A Putative High-Affinity Kainate Receptor Expressed Predominantly in Hippocampal CA3 Cells. *Nature* 351:742-744.

West PJ, Wilcox KS (2005) Comparison of kainate receptor-mediated EPSCS in superficial layer neurons of the rat medial entorhinal cortex. *Epilepsia* 46:128-129.

West PJ, Dalpe-Charron A, Wilcox KS (2007) Differential contribution of kainate receptors to excitatory postsynaptic currents in superficial layer neurons of the rat medial entorhinal cortex. *Neuroscience* 146:1000-1012.

White EL (1989) Cortical Circuits. *Synaptic Organization of the Cerebral Cortex*, Birkhäuser, Basel.

Whittington MA, Faulkner HJ, Doheny HC, Traub RD (2000) Neuronal fast oscillations as a target site for psychoactive drugs. *Pharmacology & Therapeutics* 86:171-190.

Wisden W, Seeburg PH (1993) A Complex Mosaic of High-Affinity Kainate Receptors in Rat-Brain. *Journal of Neuroscience* 13:3582-3598.

Witter MP, Groenewegen HJ, Lopes da Silva FH, and Lohman, AH (1989) Functional organization of the extrinsic and intrinsic circuitry of the parahippocampal region. *Prog. Neurobiol.* 33:161-253.

Witter MP, Amaral DG (2004) Hippocampal formation. In The rat nervous system, G. Paxinos, ed. (San Diego: Academic Press) 637-703.

Witter MP, Moser EI (2006) Spatial representation and the architecture of the entorhinal cortex. *Trends Neurosci* 29:671-678.

Yasuda, R (2006) Imaging spatiotemporal dynamics of neuronal signaling using fluorescence resonance energy transfer and fluorescence lifetime imaging microscopy. *Curr. Opini. Neurobiol.* 16:551–561.

Yasuda R, Harvey C, Zhong H, Sobczyk A, Svoboda, K (2006) Super-sensitive Ras activation in dendrites and spines revealed by 2-photon fluorescence lifetime imaging, *Nat. Neurosci.* 9:283–289.

Yoshimura Y, Callaway EM (2005) Fine-scale specificity of cortical networks depends on inhibitory cell type and connectivity. *Nat. Neurosci.* 8:1552–1559.

Yoshimura Y, Dantzker J L, Callaway EM (2005) Excitatory cortical neurons form fine-scale functional networks. *Nature* 433:868–873.

Yuste R (2005) Fluorescence microscopy today. *Nat. Methods.* 2:902–904.

Zhang QX, Pilquil CS, Dewald J, Berthiaume LG, Brindley DN (2000) Identification of structurally important domains of lipid phosphate phosphatase-1: implications for its sites of action. *Biochem. J.* 345:181–184.

Zhang F, Wang LP, Boyden ES, Deisseroth, K (2006) Channelrhodopsin-2 and optical control of excitable cells. *Nat. Methods*. 3:785–792.

Zhang, F, Wang LP, Brauner M, Liewald JF, Kay K, et al. (2007) Multimodal fast optical interrogation of neural circuitry. *Nature* 446:633–639

STATEMENT OF CONTRIBUTION

Some parts of my doctoral thesis have been conducted in a collaborative approach. In the following, please find a statement of the relative contributions to the data presented.

Chapter 3:

I have performed all the calibration and mapping experiments in this chapter and the Biocytin reconstructions. Dr. Michael Bendels have designed the photostimulation software and along with Dr. Christian Leibold have contributed towards developing the detection algorithm.

Chapter 4:

I have conducted the mapping experiments of L2Ss and L2Ps in this chapter, and analyzed the data using the detection algorithm described in the previous chapter.

Chapter 5:

I have performed all the *in vitro* electrophysiological experiments in this chapter. Dr. Sebastian Schuchmann has performed the *in vivo* EEG (figure 5-15) Dr. Thorsten Trimbuch generated the PRG-1 mouse in the lab of Prof. Robert Nitsch and along with Dr. Johannes Vogt was involved in the immunocytochemistry of PRG-1 (figures 5-13 and 5-14)

In addition, and referring to all the chapters above, I have developed new analytical tools, conceived experiments and contributed to writing the respected manuscripts.

Berlin, 11th January, 2010.

DEUTSCHE ZUSAMMENFASSUNG

Neuronale Mikroschaltkreise bilden die elementaren Einheiten von Hirnfunktionen. Solche Mikroschaltkreise verbinden die elementaren Bausteine, d.h. exzitatorische und inhibitorische Neurone zu funktionalen neuronalen Netzwerken. Die Struktur neuronaler Mikroschaltkreise reift während der Entwicklung und stabilisiert sich im adulten Organismus. Entwicklungs- oder umgebungsbedingte Beeinträchtigungen haben oft fehlerhaft verknüpfte Kreisläufe zur Folge. Die Betrachtung normaler und falsch verknüpfter Mikroschaltkreise ermöglicht das bessere Verständnis der zugrunde liegenden Funktionen unter physiologischen oder pathologischen (neuropsychiatrischen Krankheiten) Bedingungen.

Das Ziel meiner Doktorarbeit ist das Verständnis des funktionalen Mikroschaltkreises des entorhinalen Cortex, ins Besondere des medialen entorhinalen Cortex (mEC), in seiner gesunden Funktion und auch im Zusammenhang mit Krankheiten.

Frühere Studien konzentrierten sich hauptsächlich auf die anatomische Verschaltung des entorhinalen Cortex. Jüngste in vivo Forschungen offenbarten jedoch die funktionale Relevanz des entorhinalen Cortex als unabhängige Recheneinheit, die bei der räumlichen Orientierung eine Schlüsselrolle einnimmt und keineswegs nur als Informationsdrehkreuz zwischen Cortex und Hippocampus dient. Die zeitliche Diskrepanz zwischen strukturellen und funktionalen Studien warf viele offene Fragen auf. Desweiteren wurde der mEC in Zusammenhang mit Alzheimer, Temporallappenepilepsie (TLE), Schizophrenie und vielen anderen neuroentwicklungs- und psychiatrischen Erkrankungen gebracht. In den Kapiteln 1 und 2 leite ich das Konzept des neuronalen Mikroschaltkreises ein und gehe auf die Notwendigkeit des Verständnisses auf struktureller und funktionaler Ebene ein. Außerdem erläutere ich die Rolle des mEC bei der räumlichen Orientierung und in der Pathophysiologie, sowie die Wichtigkeit die zugrunde liegenden Mikroschaltkreise zu betrachten, welche unser Verständnis in obigen Zusammenhängen erweitern dürften.

In Kapitel 3 diskutiere ich die zur Untersuchung neuronaler Mikroschaltkreise verfügbaren Techniken, stelle unsere schnell abtastende Photostimulationssoftware vor und vergleiche deren Leistungsvermögen mit dem anderer Standardtechniken und Softwares. Die Anwendbarkeit, Auflösung und Reproduzierbarkeit der Software wurde an Hand der Kartierung der intralaminaren synaptischen Verknüpfungen der Schicht 2 Sternzellen (L2S) des mEC als Modellzelle bestätigt. Desweiteren überprüfte ich den Detektionsalgorithmus zur Unterscheidung photo-induzierter Ereignisse von Hintergrundereignissen und bewies außerdem dessen Verlässlichkeit zwischen den beiden Arten photo-induzierter Ereignisse, direkte Antworten und synaptische Eingänge, zu differenzieren.

In Kapitel 4 lege ich die Kernergebnisse bezüglich der funktionalen Mikroschaltkreise der beiden Projektionsneuronen der Schicht 2 des mEC, L2S und Schicht 2 Pyramidenzellen (L2P), dar. Meine Ergebnisse offenbaren das Vorhandensein erregender Mikroschaltkreise mit einer zelltypspezifischen Trennung zwischen intralaminaren rekurrenten Verbindungen und aufsteigenden interlaminaren Rückkopplungsverbindungen sowie eine modulare Organisation. L2S zeigen hauptsächlich intralaminare rekurrente Verknüpfungen wohingegen L2P mehrheitlich Eingang von aufsteigenden interlaminaren Rückkopplungsverbindungen aus den tiefen Schichten des mEC erhalten. Letztere bilden den hippocampalen Rückführkreis. Aufsteigende interlaminare Rückkopplungsverbindungen nach Schicht 2 sind in räumlichen Modulen organisiert welche für die beiden Zelltypen verschiedene Eigenschaften aufweisen.

Neuronale Synchronität ist eine inherente Eigenschaft neuronaler Mikroschaltkreise. Hirnrythmen verschiedener zeitlicher Frequenzen, ins Besondere Gamma Oszillationen, werden wichtige Rollen beim Zusammenführen von Informationen aus verschiedenen Hirnregionen zugeschrieben. In Kapitel 5 beschäftige ich mich mit einem Modell zur Untersuchung der Rolle von mEC Mikroschaltkreisen im Zusammenhang mit neuronaler Synchronität und Erregbarkeit, den zugrunde liegenden molekularen Mechanismen dieser Synchronität und den pathologischen Folgen von Übererregbarkeit. Aus den Ergebnissen dieser Studien schlussfolgere ich, dass GluK2 enthaltende Kainatrezeptoren eine Schlüsselrolle bei durch Kainat induzierten Gammaoszillationen in den oberflächlichen Schichten des mEC einnehmen. KARs der Schicht 3 Pyramidenzellen (L3Ps) sind auf die somatodendritischen Bereiche beschränkt. Die spezielle Expression und Verteilung von GluK2 enthaltenden KARs auf L3Ps könnte sie empfänglich für mit epileptischen Anfällen in Beziehung stehende krankhafte Veränderungen machen, wie sie oft bei Tiermodellen für TLE (z.B. Kainatmodell, Pilokarpinmodell, etc.) beobachtet werden. Da sich Epilepsie aus

übererregbaren neuronalen Netzwerken entwickeln kann, gibt es mehr als einen Weg wie und wo dies erfolgen kann. Als Ausblick diskutiere ich die Rolle eines neuartigen Vermittlers synaptischer Übertragung, PRG-1 (plasticity related gene-1) bei der Modulation von Erregbarkeit in neuronalen Netzwerken. Dieser wurde in einer anderen Studie, an der ich beteiligt war, untersucht. PRG-1 findet sich ausschließlich an glutamatergen Synapsen auf der postsynaptischen Seite und moduliert die synaptische Übertragung. Genetische Deletion von PRG-1 führt zu schwerer Übererregbarkeit (Kapitel 5) des Hippocampus welche in der Entstehung pathologischer Anfälle mündet.

Zusammenfassend zeigen diese Erkenntnisse die Wichtigkeit funktionale Mikroschaltkreise eines cortikalen Bereichs unter normalen wie auch unter pathologischen Bedingungen zu untersuchen auf. Die zelltypspezifische und modulare Organisation von Inputs auf L2S und L2P erweitern unser Wissen darüber wie Information innerhalb eines lokalen Mikroschaltkreises des entorhinalen Cortex übermittelt wird. Den Eingängen der tiefen Schichten wird eine herausragende Rolle für L2 Zellen bei deren Funktion bei der räumlichen Orientierung zugeschrieben. Diese Arbeit zeigt die ersten funktionalen Beweise der Existenz solcher Eingänge auf L2 Zellen. Desweiteren ist die Charakterisierung der KARs auf L3Ps ein weiterer Schritt zum Verständnis KAR-vermittelter synaptischer Übertragung und deren Beitrag zu neuronaler Synchronität und Erregbarkeit im mEC. Die Identifikation eines neuartigen Mediators der Erregbarkeit von Synapsen, PRG-1, zeigt eine entscheidende Möglichkeit wie neuronale Netzwerke genau reguliert werden können. Das Gleichgewicht zwischen Erregung und Inhibition ist notwendig um die Integrität neuronaler Mikroschaltkreise zu bewahren.

In ihrer Gesamtheit leistet meine Doktorarbeit einen Beitrag zum Verständnis der funktionalen Mikroschaltkreise im medialen entorhinalen Cortex und beantwortet Fragen zu dessen Rolle unter physiologischen und pathophysiologischen Bedingungen.

RESUME

For reasons of data protection,

the resume is not included in the online version

PUBLICATIONS

No.	Title	Status
1.	Bendels M*, **Beed P***, Leibold C, Schmitz D*, and Johenning F* (2008) A novel control software that improves the experimental workflow of scanning photostimulation experiments. ***J. of Neuroscience Methods*** 175:44-57.	Published
2.	Trimbuch T*, **Beed P***, Vogt J*, Schuchmann S, Maier N, et al. (2009) PRG-1 is a novel player at the synapse, modulating excitatory transmission via lipid phosphate-mediated signaling. ***Cell*** 138:1222-1235.	Published
3.	**Beed P**, Salmen B*, Schmitz D* (2009) Role of GluK2 in excitability and synchrony within the entorhinal cortex. ***PLoS One*** 4:e5576 .	Published
4.	Johenning F, **Beed P**, Trimbuch T, Bendels M, Winterer J, Schmitz D (2009) Dendritic compartment and neuronal output mode determine pathway specific LTP in the piriform cortex. ***J. of Neuroscience*** 29:13649-13661. .	Published
5.	Bendels M, **Beed P**, Johenning F, Schmitz D, Leibold C (2009) Detection of input sites in scanning photo stimulation data based on spatial correlations. ***J. of Neuroscience Methods*** (in revision)	In revision
6.	Salmen B, Breustedt J, **Beed P**, Winterer J, Oezdogan T, Schmitz D (2009) GluK1 inhibits calcium dependent and independent transmitter release at associational / commissural synapses in area CA3 of the hippocampus ***Hippocampus*** (in revision)	In revision
7.	**Beed P***, Bendels M*, Wiegand HF, Leibold C, Johenning F*, Schmitz D* (2009) Microcircuitry in the medial entorhinal cortex reveals a cell-type–specific and modular organization ***Neuron*** (in revision)	In revision

* equal contribution

CONFERENCE PROCEEDINGS

No.	Title
1.	**Beed P**, Salmen B, Schmitz D (2007) Synaptic and extrasynaptic kainate receptors in neurons of the entorhinal cortex. ***PENS European Synapse Summer School, Bordeaux, France.***
2.	Bendels M, Johenning F, **Beed P**, Leibold C, Schmitz D (2007) High-spatial-resolution photo stimulation for mapping the synaptic connectivity of large brain regions. ***37th Annual Meeting of the Society for Neuroscience. San Diego, USA.***
3.	(a) **Beed P**, Salmen B, Schmitz D (2008) Kainate induced currents on neurons of the entorhinal cortex. (b) Salmen B, **Beed P**, Oezdogan T, Winterer J, Breustedt J, Schmitz D (2008) Mechanism of Kainate receptor induced suppression of glutamatergic synaptic transmission at the hippocampal AC Synapse ***6th Annual meeting of the Federation of European Neuroscience, Geneva, Switzerland.***
4.	**Beed P**, Bendels M, Leibold C, Johenning F, Schmitz D (2009) Different input patterns to stellate versus pyramidal cells in the entorhinal cortex. ***Proceedings of the 32nd Göttingen Neurobiology Conference. Göttingen, Germany.***
5.	(a) **Beed P**, Bendels M, Wiegand HF, Leibold C, Johenning F, Schmitz D (2009) Microcircuitry in the medial entorhinal cortex reveals a cell-type–specific and modular organization (b) Johenning F, **Beed P**, Trimbuch T, Bendels M, Winterer J, Schmitz D (2009) Dendritic excitability determines pathway-specific LTP induction in the piriform cortex ***39th Annual Meeting of the Society for Neuroscience. Chicago, USA.***

ACKNOWLEDGEMENTS

I would like to extend my sincere thanks and gratitude to Prof. Dr. Dietmar Schmitz, Director, NeuroCure, Berlin for giving me the opportunity to work on my doctoral thesis in his laboratory and also for the invaluable help and guidance during my work. His extensive knowledge of literature and keen insights made work light and enjoyable.

I would like to thank Dr. Benedikt Salmen for introducing me to the lab and the basic electrophysiological techniques. I am happy to have received a smooth start in the lab on both the scientific and at the social level.

I owe a special thanks to Dr. Friedrich Johenning for patiently introducing me to calcium imaging experiments. Moreover, I am lucky to have shared most of my working time in the lab with him as we were tucked away in our imaging oasis amidst intense scientific and nonscientific discussions. Lastly I thank him for critically reading my thesis.

In addition, I also owe my thanks to

- Anke Schönherr and Susanne Walden for providing excellent technical help throughout my stay - be it solutions, reagents or intras, they were always there
- Michael Bendels and Christian Leibold for their collaboration on the development of the software and analysis of the neuronal mapping data
- Thorsten Trimbuch and the rest of the team on the PRG-1 project
- Claudia Böhm for her help in translating the concluding remarks of this thesis into German and simultaneously for reading parts of the thesis
- Sarah Shoichet for critically reading the manuscripts
- Everyone else in the Schmitz lab for providing a friendly and warm atmosphere during my doctoral thesis
- My family for always being there